CENTRO DE INVESTIGACIONES EN ÓPTICA, A.C.

FABRICATION OF FLUORESCENT NANOSTRUCTURED ORGANIC MATERIALS AND THEIR APPLICATION AS CONTRAST AGENT IN CONFOCAL AND TWO-PHOTON MICROSCOPY

DOCTORA EN CIENCIAS (ÓPTICA)

Supervised by: Dr. Gabriel Ramos Ortiz
Co-supervised by: Dr. Juan Luis Pichardo Molina

Presented by: M. en C. Laura Aparicio Ixta

February 2016

León, Guanajuato, México

Fabrication of fluorescent nanostructured organic materials and their application as contrast agents in confocal and two-photon microscopy

Thesis submitted in partial fulfillment of the
requirements for the degree of

DOCTORA EN CIENCIAS (ÓPTICA)

Presented by:

M. en C. Laura Aparicio Ixta

Supervised by

Dr. Gabriel Ramos Ortiz

Co-supervised by

Dr. Juan Luis Pichardo Molina

Centro de Investigaciones en Óptica, A. C.

León, Guanajuato, México 2016

Acknowledgements

I would like to thank all the people who contributed in some way to the work described in this thesis. First and foremost I offer my sincerest gratitude to my supervisor, Dr. Gabriel Ramos, who gave me the freedom to explore on my own and at the same time the guidance to recover when my steps faltered. His guidance helped me in all the time of research and writing of this thesis.

My co-advisor, Dr. Juan Luis Pichardo, has been always there to listen and give advice. I am deeply grateful to him for the long discussions that helped me sort out some technical details of my work.

Additionally, I would like to thank my evaluation committee members Dr. Marco Antonio Meneses, and Dr. Sergio Calixto for their interest in my work. Also I would like to thank committee members Dr. Ramón Carriles, Dr. Claudio Frausto, Dr. Marco Antonio Meneses and Dra. Rosa Santillan for their time, and helpful comments to improve the dissertation writing.

Similar, my profound gratitude goes to Mario Ruiz for his patience in his English class, which paid off allowing write this dissertation in English.

I am grateful to Dr. Mario Rodríguez for his encouragement and practical advice. I am also thankful to him for reading my reports; commenting on my views and helping me understand and enrich my ideas.

Every result described in this thesis was accomplished with the help and support of fellow labmates and collaborators, without his efforts my job would have undoubtedly been more difficult.

Appreciation also goes out to all collaborators who provide me the fluorescent materials studied in this dissertation. Cristina C. Jiménez and Dr. Norberto Farfán (Facultad de Química, Depto. de Química Orgánica, Universidad Nacional Autónoma de México) for providing me the borinates. Prof. Zujin Zhao and his team (College of Material Chemistry and Chemical Engineering Hangzhou Normal University) for providing me the BODIPYS. Jesús Rodríguez Romero and Dra. Rosa Santillan (Departamento de Química, Centro de Investigación y de Estudios Avanzados del IPN) for facilitating me BT2.

Also I would like to thank Dr. Mikhail G. Zolotukhin and Dr. Serguei Fomine (Instituto de Investigaciones en Materiales, Universidad Nacional Autónoma de México) for providing me the monomer M1 and polymer P1 and the calculations of molecular orbitals involved in the electronic transitions of these materials studied in this dissertation.

My sincere thanks also to Dr. Daniel Martinez Fong (Programa de Doctorado en Nanociencias y Nanotecnología, CINVESTAV), who gave me access to his laboratory and research facilities. I would like to express my sincere gratitude to Victor for his friendship and support with staining cells and MTT assays. Without they precious support it would have not been possible to conduct this research.

I am thankful to Dra. Myrna Sabanero López and Liss Flores (Departamento de Biología, Div. Ciencias Naturales y Exactas, Universidad de Guanajuato) for their assistance in cell staining in the second part of this dissertation.

The studies on nanoparticles fabricated by laser ablation discussed in this dissertation would not have been possible without the help of Enrique Alba (División de Ciencias e Ingeniería, Campus León, Universidad de Guanajuato). I appreciate his collaboration.

I am also indebted to Dra. Ivana Moggio for the measurements of the fluorescent lifetime of BT2.

I recognize that this research would have not been possible without the financial assistance of CONACYT through my scholarship and projects; I express my gratitude to this institution.

Finally, but not least, I would like to acknowledge my friends and family who supported me during my stay here.

None of this would have been possible without the love, support, encouragement and patience of my family to whom this dissertation is dedicated. His unconditional support has been essential during all these years.

Particularly, I would like to express my heart-felt gratitude to Karely, Yeni, Blanca, Susy, Villa, Joel, Octavio, Lupita, Brenda and all those that I inadvertently omit, I greatly value their friendship and I deeply appreciate their belief in me.

Yeni besides being a great friend and an example of perseverance helped me to implement the electrophoresis technique, sharing her excellent advice, reagents, and protocol. Without her expertise my project might not have ever come to conclusion. I cannot adequately express how thankful I am.

I wish to sincerely thank Karla who is a great friend and the best basketball player that I knew in grad school. I am lucky to have met Karla here, and I thank her for her friendship during these years, and support through the ups and downs of my academic career. I cannot imagine being the person I am today without such a great friend through the years as her.

Thanks for everything that helped me get to this day.

Fabrication of fluorescent nanostructured organic materials and their application as contrast agent in confocal and two-photon microscopy

Contents

Abstract

Chapter 1. Introduction

1.1 Two-Photon Microscopy…….. 1

1.2 Photoluminescent nanoparticles used as contrast agents ...…….……..... 4

1.2.1 Quantum dots …….…….… 5

1.2.2 Gold nanoparticles …….…. 5

1.2.3 Organic fluorescent nanoparticles …….….. 6

1.3 Future Trends of nanostructures…….…….…. 7

1.4 Goals ……..…. 7

1.5 Outline ..……..…. 8

Chapter 2. Two-Photon Absorption and fluorescence in organic materials

2.1 Introduction…….……..…….. 9

2.2 Fluorescence induced by one photon absorption …….…. 9

2.3 Fluorescence induced by two-photon absorption…….. 10

2.4 Fluorescence quantum yield …….…. 12

2.5 Techniques for measuring two-photon absorption cross section (Z-scan and TPEF)……...…….. 14

2.6 Structure-property relationships for fluorescent organic materials ……... 17

2.7 Recent efforts in Two-Photon Organic Materials Development ……... 19

Chapter 3. Organic nanostructured materials with TPA properties

3.1 Fluorescent nanostructures ……..……..…… 25

3.2 Fabrication methods of organic fluorescent nanostructures ……...……... 27

3.2.1 Laser ablation to produce organic nanoparticles……..…….....… 29

3.2.2 Reprecipitation method to produce organic nanoparticles ……... 30

3.2.3 Microemulsion O/W to produce organic nanoparticles ……..... 32

3.3 Functionalization of fluorescent silica nanoparticles …… 34

3.4 Bioconjugation……..……..……..……..... 35

Chapter 4. Fluorescent organic materials, photophysical characterization

4.1 Borinates ……..... 38

4.1.1 Linear Optical Properties…… 38

4.1.2 Two-photon absorption.…..……...……... …… 40

4.2 BODIPYS……...……..……..… 42

4.2.1 Linear Optical Properties…….....….. 43

4.2.2 Two-photon absorption…….……...…..... 45

4.3 Fluorene derivatives…...……..…….…… 46

4.3.1 M1 and P1…….…… 47

4.3.1.1Transmission electron microscopy of M1(P1)-NPs……..……..... 48

4.3.1.2 Linear Optical Properties…….…..……...… 49

4.3.1.3 Two-photon absorption…… 54

4.3.1.4 Photostability……..... 58

4.3.2 BT2……..….. 59

4.3.2.1 Linear Optical Properties……..…...……... 60

4.3.2.2 Two-photon absorption in different solvents ……. 63

4.3.2.3 Fabrication of nanoparticles…… 65

4.3.2.4 Comparative study of BT2-Nanoparticles fabricated by three different methods…….……..... 70

4.3.2.4.1 Size of the nanoparticles…….……..… 71

4.3.2.4.2 Linear Optical Properties…….…...…… 72

4.3.2.4.3 Two-photon absorption ……. 74

4.3.2.4.4 Photostability ...……...…….…… 75

4.3.3 Functionalization and bioconjugation…….. 76

Chapter 5. Application of fabricated nanostructuras as contrast agents in confocal and Two-Photon Microscopy

5.1 Cell staining……..... 81

5.2 Cell viability……... 82

5.3 Fluorescence Microscopy ……..…… 83

5.3.1 Fluorescence images of HeLa cells treated with M1(P1)-NPs……..... 83

5.3.2 Fluorescence images of HeLa cells treated with BT2-NPs……. 86

Conclusions .…….…….….. 89

Perspectives ...…….……...……..…… 91

Research products…...…….……..….. 92

References …….……..… 94

Appendix A. Reagents and equipment used to fabrication and characterization of fluorescent materials……..... 106

Appendix B. Synthesis of organic nanoparticles by reprecipitation method..... 108

Appendix C. Synthesis of silica nanoparticles doped with organic fluorescent fluorophores……..…..…..… 108

.

Appendix D. Fabrication of organic nanoparticles by laser ablation……..……..... 109

Appendix E. Surface modification of amino-functionalized SNPs with folic acid/Transferrin ……....…….. 110

Appendix F. Agarose gel electrophoresis...……..……..…..... 111

Appendix G. Cell cytotoxicity assay……..... 112

List of Tables

Table 1.1 TPA activity for commercial fluorophores in water.…….. 3

Table 2.1 TPA properties of organic materials shown in Figures 2.8 and 2.9. The properties are presented for materials in molecular solution and in the form of nanoparticles.……..... 22

Table 3.1. Characteristics of organic nanoparticles produced by laser ablation (LA), reprecipitation (RP) and microemulsion (ME) methods……..... 28

Table 4.1. Photophysical properties of borinates *5a-5h*…….. 41

Table 4.2. Optical properties of BODIPYS..…… 46

Table 4.3 Wavelengths of maximum absorbance and fluorescence, quantum yield and maxima TPA cross sections…….……. 57

Table 4.4 Results of thermogravimetric analysis of **M1-SNPs**……... 57

Table 4.5 Results of thermogravimetric analysis of **P1-SNPs**…… 58

Table 4.6 One-photon absorption data for BT2 compound obtained in different solvents……..… 61

Table 4.7 Emission data for derivatives studied in different solvents……. 62

Table 4.8 Summary of σ_{TPA} values of BT2 compound at 750 nm……... 64

Table 4.9 Results of thermogravimetric analysis of **BT2-SNPs**……..…… 67

Table 4.10 Photophysical Properties of fluorescent organic nanoparticles and BT2 in THF solution……...……. 76

List of Figures

Fig. 1 Comparison between confocal and two-photon microscope with respect to image formation. When focusing on the actual focal plane under one-photon excitation, a contribution from adjacent planes that are physically excluded in the two-photon process is obtained…… 2

Fig.2.1 Schematic energy level diagram showing the excitation process of a molecule from the ground state, S_0, to an excited state, S_1…….. 10

Fig. 2.2 Schematic energy level diagram showing the excitation process of a molecule from the ground state, S_0, to an excited state, E_1. The photons can have the same energy (degenerate case), or different energies (non-degenerate case)…….……..... 11

Fig. 2.3 Fluorescence induced by one and two-photon absorption in an organic material.…… 12

Fig. 2.4 The experimental setup for measuring the quantum efficiency. …… 13

Fig. 2.5 Z-scan technique. The pulse energy of a train of pulses is kept constant, but changes in intensity are achieved by moving the sample along the propagation direction Z. The transmittance is measured at each Z position of the sample.…….…..…... 15

Fig. 2.6 Typical TPEF experimental setup to measure the σ_{TPA} in organic materials. The photoluminiscense promoted by the absorption of two photons is detected from a solution of the sample under test and compared with that from a standard tested under the same experimental conditions……..… 16

Fig. 2.7 Molecular architectures for optimization of TPA responses in organic compounds: a) linear, b) dipolar c), quadrupolar d) and octupolar……..……. 19

Fig. 2.8 Linear structures of efficient organic two-photon dyes……... 20

Fig. 2.9 Two-dimensional structures of efficient organic two-photon dyes……. 21

Fig. 3.1 Classification of fluorescent nanostructures based on their different chemical structural compositions…….. 26

Fig. 3.2 Architectures of organic fluorescent nanostructures and their fabrication methods. NPs-PEG could have different functions in the block sections or simply to self-assemble into uniform structures and silica shell in FSNP acted as protecting agents of matrix…… 27

Fig. 3.3 Fabrication method of organic nanoparticles utilizing laser ablation of amorphous target (a) or microcrystals in water (b), where the bulk solids are converted directly into nanoparticles which are caught by water and stabilized as nanocolloids……...…… 30

Fig. 3.4 Reprecipitation method…… 31

Fig. 3.5 Synthesis of silica nanoparticles doped with hydrophobic organic dyes…. 33

Fig. 3.6 Formation of the silica layer functionalized with amino groups……. 34

Fig. 3.7 Common functional groups on nanoparticles that provide the ability to couple to biomolecules…….. 35

Fig. 3.8 Representative bioconjugation scheme for attachment of biomolecules onto the surface of silica nanoparticles……. 36

Fig. 4.1 Molecular structure of compounds 5a-5h…… 39

Fig. 4.2 Lineal absorption (a) and emission spectra (b) for borinates ***5a-5h*** in THF solution…….. 39

Fig. 4.3 TPA cross section spectra of borinates ***5a-5h*** in THF solution……... 41

Fig. 4.4 TPE-decorated BODIPY luminogens……..… 42

Fig. 4.5 a) Absorption and b) fluorescence spectra of TPE-decorated BODIPY luminogens in dilute THF solutions…….. 44

Fig. 4.6 a) TPA and b) TPEF dispersion curves of TPE-decorated BODIPY luminogens dissolved in THF…….…….…. 45

Fig. 4.7 OPEF and TPEF spectra of 3TPE-BODIPY in THF solution……. 45

Fig. 4.8 a) Chemical structures of the fluorene monomer BT2, M1 and its cross-conjugated polymer P1. b) THF solutions of the same compounds excited by UV light…… 47

Fig. 4.9 TEM micrographs of P1-NPs obtained from suspension processed with two different concentration of CTAB: a) 0.08 mM and b) 0.8 mM. TEM micrographs of P1-NPs obtained with two different concentrations of aerosol-OT: c) 5 mM and d) 10 mM. Insets: nanoparticles size distribution from the analysis of various TEM micrographs……..…….…….. 49

Fig. 4.10 Linear absorption spectra from a) THF solution of M1, aqueous suspensions of M1-NPs and aqueous suspensions M1-SNPs; b) THF solution of P1, aqueous suspensions of P1-NPs and aqueous suspensions P1-SNPs. In the case of M1(P1)-NPs the suspensions are stabilized with CTAB. The dash-dotted line represents the M1(P1)-SNPs absorption spectrum before scattering subtraction and the dotted line the scattering baseline. Insets: molecular orbitals showing the ICT character in $S_0 \rightarrow S_1$ transitions calculated for models of M1 and P1…… 50

Fig. 4.11 The most important excitations contributing to the transitions in M1….. 51

Fig. 4.12 The most important excitations contributing to the transitions of an oligomer structure used as model for P1…….…….. 52

Fig. 4.13 Normalized photoluminescence (PL) spectra for a) monomer M1 and b) polymer P1 in solutions and aqueous suspensions. Excitation: UV lamp……..... 53

Fig. 4.14 Log-log plot for the dependence of TPEF on pump intensity taking **M1**-SNPS and **P1**-SNPs as an example……... 54

Fig. 4.15 Normalized TPEF spectra for a) monomer M1 and b) polymer P1 in solutions and aqueous suspensions. Excitation: femtosecond pulses at 750 nm….. 55

Fig. 4.16 Two-photon absorption spectra of a) M1 and b) P1 in solutions and aqueous suspensions of nanoparticles and loaded silica nanoparticles. Insets: Log-log plot for the dependence of TPEF on pump intensity for M1-SNPS and P1-SNPs……..…… 55

Fig. 4.17 Differential thermal analysis and thermogravimetric analysis of a) M1-SNPs and b) P1-SNPs to determine the percent of fluorophore encapsulated in the silica…….. 58

Fig. 4.18 Photostability of M1 and P1 in THF solutions and aqueous suspensions of nanoparticles. The samples were exposed to illumination from a Xenon lamp and the absorption at the peak of the π-π^* transition was measured as a function of exposition time……..…… 59

Fig. 4.19 UV-Vis normalized absorption spectra of BT2 in different solvents…… 60

Fig. 4.20 Emission spectra of BT2 in different solvents……..... 62

Fig. 4.21 a) Excitation spectrum from BT2 in toluene solution. The PL is detected at 510 nm b) PL spectra of BT2 in mixtures of THF-methanol. The concentration of BT2 in these mixtures was kept constant (6×10^{-5} M). Inset photography of the PL exhibited by the mixtures.……...…… 63

Fig. 4.22 a) TPA spectra of BT2 dissolved in hexane, toluene, THF, acetone, methanol, acetonitrile. b) Non-monotonic behavior of the maximum σ_{TPA} of BT2 as a function of dielectric constant for each solvent……. 65

Fig. 4.23 UV-Vis normalized absorbance spectra of BT2 in FSNPs fabricated with 0.2g, 0.4g and 0.6g of AOT…….……. 66

Fig. 4.24 TEM micrographs and size distribution graphs of BT2-FSNPs obtained by different amount of AOT surfactant used in the fabrication process a) 0.2g, b) 0.4g and c) 0.6g.…….…… 66

Fig. 4.25 Absorption spectra of BT2 in THF solution and BT2-SNPs in THF-water mixtures.…….……. 67

Fig. 4.26 a) Comparison of absorption spectra of BT2 in THF solution, BT2-NPs, BT2-SNPs and BT2 films. Comparing the absorption spectra of the BT2 in solution, BT2 film and BT2 nanoparticles, a shoulder was clearly observed in BT2 nanoparticles and BT2 film. Presumably, this widening is due to the formation of charge-transfer complexes between BT2 molecules ……..…….. 68

Fig. 4.27 Effect of the increase of BT2 concentration in hexane solution. When the concentration of BT2 increases a) a decrease of the band corresponding to $\pi \rightarrow \pi^*$ transition is observed and b) a widening of the band corresponding to ICT transition also is observed……...…….. 69

Fig. 4.28 b) Absorption and b) photoluminescence spectra of BT2 in THF solution, BT2-SNPs and BT2-PEG-NPs……... 70

Fig. 4.29 TEM micrographs of **BT2**-NPs obtained by different fabrication methods a) reprecipitation, b) laser ablation and c) microemulsion……. 71

Fig. 4.30 UV-Vis normalized absorption spectra of **BT2-THF, NPs-LA**, **NPs-RP** and **NPs-ME** obtained at the concentration of 1 μM…….. 72

Fig. 4.31 Normalized photoluminescence (PL) spectra for BT2 in solution and aqueous suspensions of nanoparticles……... 73

Fig. 4.32 Fluorescence decay curves of **BT2-THF**, **NPs-LA** and **NPs-RP**……. 74

Fig. 4.33 Two-photon absorption spectra of **BT2** in solutions and aqueous suspensions of nanoparticles……. 75

Fig. 4.34 Photostability of **BT2** in molecular solution (THF) and aqueous suspensions nanoparticles. Samples were exposed to illumination from a Xenon lamp and the photoluminescence was measured as a function of exposition time.……. 76

Fig. 4.35. Functionalization of BT2-SNPs with carbonyl groups ……..…..…. 77

Fig. 4.36 a) BT2-SNPs functionalized with carboxyl groups. Succinic anhydride reacts with primary amine groups in a ring-opening process, forming an amide bond and a terminal carboxylate. b) BT2-SNPs functionalized with amide group (acetylated BT2-SNPs) to inhibit the internalization into cells…….……..…….. 78

Fig. 4.37 Agarose gel electrophoresis showing comparative methodologies to functionalize BT2-SNPs-NH_2 with CHO group. (Lane 1) fluorescent molecule BT2, (Lane 2) BT2-SNPs with amino groups used as control or reference, (Lane 3-5) BT2-SNPs functionalized with 12, 36 and 60 μL of GA, respectively using hepes buffer, (Lane 6-8) BT2-SNPs functionalized with 12, 36 and 60 μL of GA, respectively using Sodium phosphate buffer…….…….. 79

Fig. 4.38. Agarose gel electrophoresis showing BT2-SNPs-NH_2 modified with 36 µl of GA in Hepes (lane 1), Sodium phosphate (lane 2), Sodium acetate (lane 3) buffer and BT2-SNPs-FA (route 1)……. 79

Fig. 5.1. Viability of a) A546 cells and b) HeLA cells cultured after the addition of aqueous suspensions at different dilutions of M1(PI)-NPs (stabilized with surfactants such as CTAB and Triton X-100) and M1(P1)-SNPs. The concentrations of suspensions before dilution were 7.5×10^{-5} M (M1-NPs), 4.1×10^{-7} M (P1-NPs), 5.2×10^{-5} M (M1-SNPs) and 3.1×10^{-7} M (P1-SNPs)……..…… 83

Fig. 5.2 One-photon (first and third row) and two-photon (second and fourth row) fluorescence images of HeLa cells treated with Hoechst 33258 and P1-NPs (A, B, C, D, F) and P1-SNPs (G, H, I, J, L). Left column: images taken with green filter to identify cytoplasm stained by nanoparticles under test. Middle column: the images taken with blue filter. Right column: superposition of images from the left and middle column. The wavelengths for one- and two-photon excitation is indicated to the left of the columns..……..…….. 85

Figure 5.3 One-photon (first row) and two-photon (second row) fluorescence images of HeLa cells treated with a) **NPs-RP,** b) **NPs-LA**, and c) **NPs-ME**. The wavelengths for one- and two-photon excitation are indicated to the left of the columns. The micrographs corresponding to the first row were obtained by setting the confocal microscope with the same parameters of image acquisition. Similar procedure was followed for the two-photon imaging…….…….. 87

Fig. 5.4 Two-photon images of HeLa cells treated with a) **NPs-RP**, b) **NPs-LA**, and c) **NPs-ME**. In each case, the laser output level for image acquisition was optimized keeping constant the remaining parameters in the microscope…....….. 88

Fig. A1. Reprecipitation method to fabricate organic nanoparticles…… 108

Fig. A2. Laser ablation method to fabricate organic nanoparticles…….……. 109

Fig. A3. Schematic illustration of three routes for the bioconjugation of FSNPs… 111

Fig. A4 Cell cytotoxicity assay. Cells were seeded in 96-well plates and exposed with an aqueous suspensions of **M1(P1)**-NPs, **M1**(**P1)**-SNPs. Purple color shows that there are live cells……... 112

Abbreviations

ACN: 3-(9-(2-(2-methoxyethoxy)ethyl)-2,7-bis{3-[2-(polyethyleneglycol-550-monomethylether-1-yl)]-4-(benzo[d]thiazol-2-yl)styryl}-9*H*-fluoren-9-yl)propanoic acid in acetonitrile.

ACQ: Aggregation-caused quenching

AIE: Aggregation-induced emission

AEE: Aggregation enhanced emission

Aerosol OT, AOT: 1-sodium bis(2-ethylhexyl)sulfosuccinate

BTNPs: Bare Two-Photon Absorption Nanoparticles without encapsulation by DSPE-PEG

BT2: 4,7-bis((9,9-dioctyl-2-fluorenyl)ethynyl)-2,1,3-benzothiadiazole

BT2-SNPs: Silica nanoparticles doped with BT2

CTAB: Hexadecyltrimethyl-ammonium bromide

CPNPs: Conjugated Polymer Nanoparticles

FA: Folic acid

FSNPs: Fluorescent silica nanoparticles

FTNPs: DSPE-PEG encapsulated Two-Photon Absorption Nanoparticles

FTNP0: FTNPs that were formulated with polymers having the feed ratio of 0% for DSPE-PEG5000-Folate in the matrix.

GA: Glutaraldehyde

LA: Laser ablation method

ME: Microemulsion method

M1: Fluorene monomer 4,7-bis[2-(9,9-dimethyl) fluorenyl]benzo[1,2,5]thiadiazole

M1-SNPs: Silica nanoparticles doped with the monomer M1

NPs: Nanoparticles

NPs-LA: BT2 nanoparticles fabricated by laser ablation method

NPs-ME: BT2 nanoparticles fabricated by microemulsion method

NPs-RP: BT2 nanoparticles fabricated by reprecipitation method

O-NPs: Organic nanoparticles

OPEF: Fluorescence excited by one photon

P1: Cross-conjugated polymer of M1

P1-SNPs: Silica nanoparticles doped with the polymer P1

RP: Reprecipitation method

TF: Transferrin

TPA: Two-photon absorption

TPE: Tetraphenylethene

TPEF: Two-photon excited fluorescence

TPM: Two-photon laser scanning microscopy

Abstract

During the past years, technological advances have provided new uses of fluorescent materials to impact in fields such as opto-electronics, information technology and, more recently, nanotechnology. One of these technologies is fluorescence microscopy which is one of the most versatile imaging techniques in biomedical research. Particularly, two-photon laser scanning microscopy (TPM) has attracted increasing attention due to several advantages over traditional techniques such as higher resolution, higher depth penetration in tissue, reduction of photobleaching and weak autofluorescence. These advantages allow to study in detail not only cellular or tissue structure, but also get information about cellular dynamics (biochemical and biophysical processes), generate medical imaging for diagnostic purposes, and monitor the site-specific delivery of a drug into a bio-specimen. To implement TPM, the biological sample under study is stained with fluorescent markers (contrast agents).

Nevertheless, it should be pointed out that the commercially available organic fluorescent materials (fluorophores) currently used in two-photon imaging exhibit very small two-photon absorption (TPA) with cross-sections commonly in the range of 1–100 GM (1 GM = 10^{-50} cm^{-4} s^{-1}). This means an area of opportunity to develop new contrast agents to provide higher sensitivity in TPM.

Intensive investigations during the last two decades have produced several reports on organic materials possessing much higher TPA properties than those commercially available; however, the toxicity of the organic solvents in which they are soluble, the decreased fluorescence properties exhibited in aqueous media and the difficult processability of these materials to fabricate nanostructures to improve their solubility in water are some factors that limit their applications in the two-photon imaging technique.

In this dissertation, novel organic compounds synthesized to achieve optimized fluorescent and TPA properties are studied and their processing into aqueous suspension of nanostructures is developed. Accordingly, this work focuses in two aspects, one related with basic research and other with practical application of the material under study. For the former, the (molecular) structure / (optical) property relationship is obtained through spectroscopy techniques, while for the latter the bioimaging of cellular lines of biomedical interest is pursued.

In total, three families of compounds are studied.

1. **Borinates**
   Eight fluorescent **borinates** were considered in this study with different molecular structures and comprising different donor (D) and acceptor (A) electronic groups.

As a main result, it was found that in **borinates** the structure D-π-C=N^+-π-A architecture introduced increments in the TPA cross-sections (σ_{TPA}) in at least a factor of five compared to the D-π-C=N^+-π-D architecture. Maximum value of σ_{TPA} in this family was of 174 GM at 760 nm.

2. Three different **BODIPYS** with tetraphenylethene (TPE) units introduced to the molecular periphery were studied. In this family of compounds, it was found that TPA and two-photon excited fluorescence (TPEF) properties are significantly improved as more TPE units are attached at the BODIPY core. Such TPE units are of importance as they provide aggregation induced fluorescence (AIE) property to the whole molecule. The luminogens with 3TPE units (**3TPE-BODIPY**) show the strongest TPA and TPEF in the wavelength range of 750–830 nm, with maximum cross-section values of 264 GM.

3. Three fluorene derivates (two monomers and one polymer called **M1**, **BT2** and **P1**, respectively) were studied. The fluorene monomer **M1** and its cross conjugated polymer **P1** were chosen to get insight into the enhancement of TPFE properties from the monomer to the polymer. The largest σ_{TPA} achieved in this work (~10^4 GM) corresponds to this polymer. Likewise, **BT2** being a structure of low molecular weight but high π-conjugation allowed to obtain σ_{TPA} values as high as ~ 1000 GM.

The materials with higher two-photon absorption were those based on fluorene moieties. Therefore, they were chosen to obtain different nanostructures fabricated by methods such as reprecipitation, microemulsion and laser ablation, whose main properties and applications resulted to be:

Aqueous suspensions of **M1** and **P1** nanoparticles prepared through the reprecipitation method exhibited maximum of 84 and 9860 GM at 740 nm, respectively, and a fluorescence quantum yield of ~1. Such two-photon activity was practically equal to that for molecular solutions of **M1** and **P1**. These materials were then successfully encapsulated into silica nanoparticles (through microemulsion method of fabrication) to provide biocompatibility. A human lung cancer cell line (**A549**) and a human cervical cancer cell line (**HeLa cells**) were incubated with our fluorescent silica nanoparticles to carry out two-photon imaging. By means of these studies we demonstrate that optimized nonlinear optical polymers loaded in silica nanoparticles can be used as efficient probes with low cytotoxicity and good photostability for two-photon fluorescence microscopy. To the best of our knowledge, this is the first time that polymer-doped silica nanoparticles have been fully characterized for their TPA and TPEF properties.

In regards to the **BT2,** compound with a D-A-D architecture with fluorene moieties as donor groups and fluorenone or benzothiadiazole derivatives as acceptor groups, led to σ_{TPA}

of 236 and 1000 GM, respectively in THF. Fluorescence quantum efficiency of these compounds was affected by the medium, with fluorescence quenching in protic solvents such as methanol due to specific solvent interactions (i.e., hydrogen-bonding). Nevertheless, in a more polar medium such as water, synthesized nanoaggregates by reprecipitation method exhibited good two-photon activity, i.e., ~500 GM and fluorescence quantum efficiency of 0.83. Furthermore, these nanoaggregates exhibited more resistance against photodegradation processes than any of the organic solutions tested.

Finally, a comparative study of the morphological and optical properties of **BT2** nanoparticles fabricated by reprecipitation (**NPs-RP**), laser ablation **(NPs-LA)** and microemulsion (**NPs-ME**) methods was realized. The way in which the chromophore **BT2** was packed in each type of nanoparticles influenced the absorption and photoluminescence properties. The studied nanoparticles were employed as exogenous agents for the visualization of human cervical cancer cell line (HeLa) using confocal and two-photon microscopy. Under similar experimental conditions, we found that the micrographs of the highest contrast were obtained with **NPs-LA**. This result showed that laser ablation is a suitable technique for the fabrication of organic fluorescent nanoparticles used as contrast agents for *in vitro* fluorescent microscopy. It is very important to mention that before this study fluorescent organic nanoparticles had not been used in the context of biophotonic applications, i.e., imaging of biological samples.

CHAPTER 1

Introduction

A general introduction to the subject of this dissertation, the motivations and aims of this work are presented in this chapter.

1.1 Two-Photon Microscopy

During the past years, technological advances have provided new uses of fluorescence, reaping the benefits of significant advances in electronics, information technology and, more recently, nanotechnology. One of these technologies is fluorescent microscopy which is one of the most versatile imaging techniques in biomedical research. The development of targeted contrast agents such as fluorescent probes (also known as fluorescent markers or contrast agents) has made it possible to selectively view morphological details of cells, specific biological events and processes in both living and nonviable systems with improved detection limits.

To date, fluorescence-based microscopy, i.e., confocal microscopy is widely used for bioimaging due to its high sensitivity, high selectivity, convenience and non-destructive character. Although confocal microscopy provides a high resolution optical sectioning capability, it has some inherent problems. As the confocal aperture reduces the fluorescence signal due to the exclusion of adjacent planes or out-of-focus, one needs a higher excitation power of UV, blue or green light, which increases the possibility of photobleaching[1] on the utilized contrast agent whereas the high energy of the photons of such UV or visible light can induce damage on the biological sample under study. Two-Photon Microscopy (TPM), first demonstrated by Denk *et al*,[2] is based on the two-photon absorption (TPA) properties of fluorophores. The fluorescence produced by this process also provides a direct visual tool for observing biological processes and clinical imaging, offering a number of unique advantages over confocal microscopy, such as:

(1) reduced specimen photodamage,
(2) enhanced penetration depth in scattering samples due to the use of excitation light in a near-infrared (NIR) spectral range,
(3) three-dimensional localization of the excitation volume (reduction of photobleaching by selective excitation of the focal volume by limitation of fluorescence excitation to within a femtoliter size focal volume),

(4) reduced fluorescence background due to the relatively low two-photon cross-section of most biomolecules responsible for autofluorescence in biological systems.[3]

In Figure 1 a schematic diagram of confocal and two-photon microscopy is shown. In confocal imaging, scattering reduces excitation of the specimen and diverts confocal fluorescent rays (green arrows) from the pinhole, cutting signal strength. In contrast, for two-photon imaging with near-IR rays, scattering of excitation rays is reduced, and fluorescence emission from the focal plane (green arrows) is efficiently collected on a wide area photomultiplier tube. Light path in a one-photon microscope showing fluorescence constricted at the focal plane but occupying all planes above and below the focus and showing the same total amount of fluorescence in each plane. Light path in a two-photon microscope showing that fluorescence excitation is localized (and limited) to the focal plane.

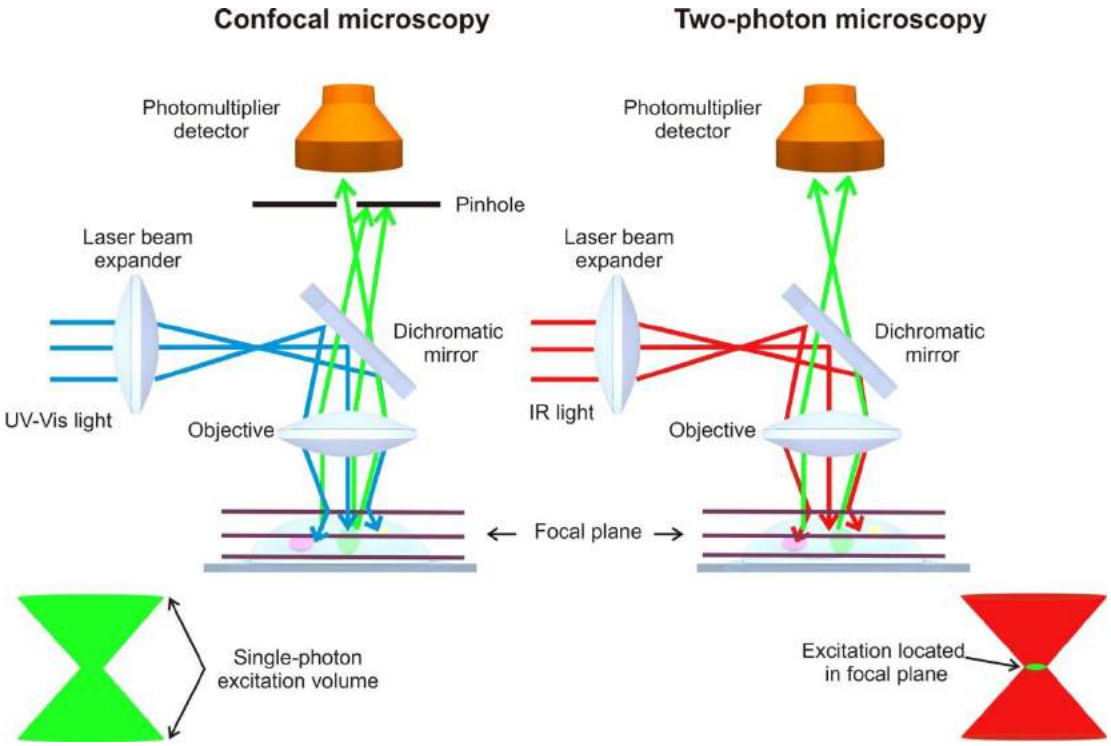

Fig. 1 Comparison between confocal and two-photon microscope with respect to image formation. When focusing on the actual focal plane under one-photon excitation, a contribution from adjacent planes that are physically excluded in the two-photon process is obtained.

Currently, one of the principal interests in the field of fluorescent microscopy is the development of novel fluorophores to be used as contrast agents or bio-markers with (a) high quantum yield of fluorescence (Φ_F) and high absorbance, (b) high TPA cross section,

quantified in GM in the NIR 700–900 nm window; (c) resistance to photobleaching, which is a critical problem; (d) sufficient in vitro and in vivo stability; (e) adequate dispersibility in the biological environment; (f) resistance to metabolic disintegration and non-toxicity and (g) the feasibility of conjugation with biomolecules for targeting specific cellular sites.[4]

The first TPA dyes studied in 1972,[5] were the Rhodamine derivatives which have σ_{TPA} values of 65 (Rhodamine 6G) and 140 GM (Rhodamine B) at 798-802 nm in methanol solution, and later a series of typical one-photon fluorophores (Alexa, fluorescein, Rhodamines and BODIPYs) [6,7] were also investigated for their TPA properties in water or a solvent compatible with biological medium. Table 1.1 summarizes the optical properties of commercially avialable dyes.[7,8]

Several biological systems often possess fluorophores, proteins such as tryptophan, tyrosine, phycoerythrin, neurotransmitter serotonin and coenzyme nicotinamide adenine dinucleotide phosphate [NAD(P)H], such that they represent a source of background signal that has to be surpassed in various orders of magnitudes by synthetic markers or labels when the latter are used in TPM in order to have a good signal to noise ratio.

Table 1.1 TPA activity for commercial fluorophores in water.

Dyes	**Excitation wavelength (nm)**	$\Phi_F\sigma_{TPA}$ **(GM)**
Alexa350	700	35
Alexa488	750	100
Alexa568	780	180
Alexa594	780	100
Bodipy	930	18
Ca-Crimson	870	100
Ca-Green	950	60
Cascade blue	740	2.5
Coumarin307[a]	800	15
DAPI	700	100
Di-4-ANEPPS[b]	950	5
Di-8-ANEPPS[b]	950	10
Dil[a]	700	95
dsRed	1000	110

[a]Methanol, [b]Ethanol

Table 1.1 Continued

Dyes	Wavelength (nm)	$\Phi_F\sigma_{TPA}$ (GM)
eGFP	930	180
Fluorescein	780	38
Fluo-3	800	13
Riboflavina	700	1
Retinol	700	0.1
Folic acid	700	0.01
Lucifer yellow	850	1.4
mCerulean	850	78
mCFP	850	190
NADH in PBS	700	0.09

[a]Methanol, [b]Ethanol

Recent search for molecules with high two-photon absorption cross-sections has led to the design and synthesis of molecules with two-photon cross-sections of >1000 GM.[9] Thus, the optimization of the nonlinear properties of the dyes has two main motivations: a) the reduction of the excitation laser intensity (less photodamage) and b) the development and study of processing methods to take advantage of the optical properties of these molecular systems but in the form of organic nanoparticles (O-NPs), to overcome many of the limitations of conventional contrast agents.[10] For instance, organic materials possessing high TPA properties are commonly soluble in toxic solvents,[11,12] which greatly limits their applications in the two-photon imaging technique. To circumvent this limitation, nanoscience has recently provided methods to bring organic molecules into biological media such as water. Some of these methods are described in Chapter 3 of this thesis.

1.2 Photoluminescent nanoparticles used as contrast agents

Recently, various photoluminescent nanoparticles (NPs) systems have been proposed to replace organic fluorophores in many bioimaging applications. In this chapter, only the most representative nanoparticles will be mentioned as well as their application to create *in vitro* images of cells through confocal and multiphoton microscopy.

1.2.1 Quantum dots

Quantum dots (QDs) are luminescent semiconductor nanocrystals with sizes ranging from 2 to 15 nm. Most QDs are composed of atoms from groups II-VI (e.g., CdSe) or III-V (e.g., InP) of the periodic table. Recently, QDs have been proposed as an alternative to conventional organic fluorophores for bioimaging because of their unique advantages. These properties of interest include size-tunable optical properties (high quantum efficiency, high molar extinction coefficients, high resistance to photobleaching, distinctive emission lifetimes, and broad excitation and narrow emission spectra). The excitation and emission spectra of the QDs are very favorable for biological detection. For instance, their broad excitation spectra and narrow emission spectra help to reduce spectral overlap, which improves the possibility of distinguishing multiple fluorophores simultaneously.

The dots are claimed to be 20 times as bright, 100 times as stable against photobleaching, and one-third as wide in spectral width, when compared to conventional fluorophores.[13] While QDs have emerged as promising probes for bioimaging, there are a number of issues that warrant attention before their full potential can be realized. The potential toxicity of QDs is a growing concern over the years. It is considered to depend on multiple QD properties, including QD core size, stability in biological media, and surface chemistry that determine the extent of cellular internalization. Unpassivated QDs could promote the generation of reactive oxygen species (ROS) causing cell death. Aggregation of QDs, as well as release of toxic ions from QDs, contributes to their cytotoxicity. Thus, few criteria should be met for QDs to be used for in vitro cellular studies without affecting the functionality of living cells. First, core-shell structure QDs must be used to prevent the leakage of cadmium ions. Second, the QDs should be additionally wrapped by biocompatible layer. Lastly, colloidal stability of QDs in biological fluids must be maintained.[1] Bioconjugation of QDs can be achieved using several approaches, e.g., they can be conjugated to the linker [14] (e.g., avidin, protein A or protein G, or a secondary antibody) by covalent binding.[15,16]

1.2.2 Gold nanoparticles

Another type of contrast agent recently proposed for two-photon luminescence imaging is nanosized gold particles, such as nanorods, nanoshells, or nanoplates. Part of the energy absorbed by gold nanoparticles is emitted in the form of scattered light, which is the basis of much gold nanoparticle–based optical imaging. The rest of the energy decays in a nonradiative form. Biocompatibility of gold is well known, although absence of toxicity is still being questioned for gold nanoparticles. Several groups have examined the cellular uptake and cellular toxicity of AuNPs and there are conflicting results about the

cytotoxicity of these nanoparticles. In several reviews the cytotoxicity, although low, has been found to be dependent of the NP size and shape, the surface modifiers, and the type of cell. In general, AuNPs can be nontoxic under certain experimental conditions, although the toxicity and side effects need to be thoroughly examined for each study.[17] Characteristic values for the two-photon action cross-section for these gold nanoprobes are determined to be in the order of a few thousand GM.[18,19] However, their emission quantum efficiency is not high. It is necessary to modify the gold nanoparticle surface to improve its dispersion and also to allow for bio-conjugation for imaging applications.

1.2.3 Organic fluorescent nanoparticles

Among all the fluorescent nanoparticles (NPs) used in bioimaging, organic nanoparticles (**O-NPs**) are the most widely studied due to their rich chemical structures, easy chemical modification and high fluorescence quantum yield. Generally, these O-NPs include carbon-based fluorescent nanostructures, fluorescent macromolecules, fluorescent polymeric nanoparticles, fluorescent supermacromolecular nanoassemblies and aggregation-induced emission fluorophores.[20]

Dyes and polymers have been used to fabricate nanoparticles and often their photophysical and physicochemical properties do not differ significantly when are processed into O-NPs.[21] However, the photoluminescent properties of some materials change when they are aggregated, that is the case of luminogens, heteroatom-containing luminogens, organometallic luminogens, polymeric luminogens, siloles and silole containing linear and hyperbranched polymers.[22-24]

Intended as contrast agents, it is important that O-NPs preserve (or enhance) the optical properties of the molecules of which they are made. Thus, the way in which organic molecules assemble to form O-NPs is important in order to preserve their optical properties. Likewise, the methods of synthesis of such O-NPs and how they can be covered, encapsulated, functionalized or bioconjugated are of paramount importance for their application as contrast agents. In this regard, let us mention as an example the rapid photobleaching exhibited by most organic fluorescent dyes. Numerous photochemical reactions occur in the cellular environment that can lead to photodegradation of the dye. Alternatives as the encapsulation of the dye in a silica matrix have emerged presently to maximize both in vitro and in vivo stability. This minimizes oxygen access, increases chemical stability and allows surface modification of the shell to enhance the hydrophilic character and cell uptake.[4] Silica NPs are robust, mechanically stable and transparent, and they can protect and stabilize the embedded fluorophores. When the fluorophores are encapsulated into the silica matrix they are brighter than single organic dyes, since they can

incorporate more than one molecule into the particle. Commonly, silica nanocomposites show good monodispersity and biocompatibility. The first biological applications of these particles was the targeting of cancer cells.[17] Different kinds of fluorescent dyes such as a metalorganic luminophore, tris(2,2'-bipyridyl)dichlororuthenium(II) hexahydrate (Rubpy), and different derivatives of the organic dye rhodamine have been incorporated into the silica matrix and the particle's silica surfaces covalently bound to an antibody and biomolecules for cell targeting purposes.[25-28]

1.3 Future Trends of nanostructures

Each of the nanomaterials described above (gold NPs, QDs, O-NPs and fluorescent silica NPs) has its respective advantages and disadvantages depending on the intended application. All together, these materials will play a significant role in the development of imaging tools to provide better insights into biological processes, including early diagnosis of human diseases. It is anticipated that advances in nanosciences combined with the attractive features of many nanoparticle systems will render these particles increasingly attractive for bioanalytical applications in the future. An important trend is the development of multifunctional or theranostic nanoparticles, nanoparticles that are capable of accomplishing multiple objectives such as imaging, diagnostic and therapy.

1.4. Goals

The main aim of this dissertation is the study of the photophysical properties of novel organic fluorescent materials in solution and different nanostructures and their use as contrast agents in confocal and two-photon microscopy. As it was mentioned above, the way in which organic molecules assemble to form O-NPs determines their optical properties. This characteristic has received little attention in the literature. For that reason in this wok a comparative study of the morphological, photophysical and optical properties of organic-fluorescent nanoparticles fabricated by reprecipitation, laser ablation and microemulsion methods (fluorescent silica nanoparticles) is performed. Bioimaging of cellular lines using these O-NPs is also presented.

The specific objectives of this dissertation are:

- Assess the potential of novel fluorophores as contrast agents for fluorescent microscopy. Specifically, fluorescent borinates, bodypies, fluorene-chromophores and a polymer are studied.

- Measure the quantum yield of fluorescence of candidate materials with TPA properties.
- Find optimal conditions to fabricate nanoparticles by reprecipitation, microemulsion and laser ablation.
- Characterize the fluorophores in solution and nanoparticles by absorption spectroscopy, and two-photon excited fluorescence.
- Obtain morphological characteristics of the fluorescent nanoparticles.
- Evaluate the photostability of fluorophores in solution and aqueous suspensions of nanoparticles.
- Investigate through confocal and two-photon microscopy the ability of organic nanoparticles to penetrate into a human lung cancer cell line (A549) and a human cervical cancer cell line (HeLa cells).
- Evaluate the viability of cells after their staining with the organic nanoparticles.
- Bioconjugate fluorescent silica nanoparticles with folic acid and transferrin.

1.5. Outline

The thesis consists of five chapters. Chapter 2 describes the two-photon absorption process in organic materials as well as fluorescence produced by one and two-photon absorption. Fluorescence quantum yield and the main techniques for measuring two-photon absorption cross section are also presented. Structure-property relationship for fluorescent organic materials is another important section of this chapter. Next, in Chapter 3, a description of fabrication methods of organic fluorescent nanostructures used in this dissertation (reprecipitation, laser ablation and microemulsion) are presented. The materials and methodology for the fabrication of organic fluorescent nanostructures are shown in Appendixes. Additionally, a brief introduction about functionalization of silica nanostructures fabricated by microemulsion method as well as bioconjugation for coupling with molecules of biological interest is shown. The results and discussions of photophysical characterization of fluorescent materials in solution and processing of these materials in different nanostructures are provided in chapter 4. Application of the fluorescent nanostructures fabricated as contrast agent in confocal and two-photon microscopy is provided in chapter 5. Finally, the conclusions and work perspectives are shown.

CHAPTER 2

Two-Photon Absorption and fluorescence in organic materials

2.1 Introduction

Applications built around two-photon absorption (TPA) property as two-photon laser scanning microscopy,[2] optical power limiting,[29] 3-D microfabrication,[30] data storage[31] and photodynamic therapy[32] still require of new materials with optimized properties. For this purpose it is required to work in several areas, including molecular and synthetic chemical designs, understanding of structure–property relations to obtain molecules with large TPA cross sections, and increased fluorescence quantum yields in the visible and near-infrared (NIR).[33]

For new TPA molecules, an accurate characterization of their optical properties is fundamental in order to assess their potential for applications. This chapter presents basic definitions of the optical properties of interest in this dissertation, the characterization techniques, and design strategies and structure–property relations of molecular structures with the goal of enhancing TPA for fluorescence microscopy application.

2.2 Fluorescence induced by one photon absorption

The radiation emission process due to the deactivation of a molecule is generally referred as luminescence while the term photoluminescence refers to the particular case in which the excitation takes place by absorption of photons. Photoluminescence can be divided into two categories: fluorescence and phosphorescence.

Fluorescence is the emission of photons by atoms or molecules whose electrons are transiently stimulated to a higher excitation state by radiant energy from an outside source. During fluorescence, the absorption and re-emission events occur nearly simultaneously, the interval being only 10^{-9}–10^{-12} seconds; therefore, fluorescence stops after there is no more exciting incident light.

When a fluorescent molecule absorbs a photon of the appropriate wavelength, an electron is excited to a higher energy state and almost immediately collapses back to its initial ground state. In the process of energy collapse, the molecule can release the absorbed energy as a fluorescent photon. Since some energy is lost in the process, the emitted fluorescent photon exhibits a lower frequency of vibration and a longer wavelength than the excitatory photon

that was absorbed. The situation is depicted graphically in what is known as a *Jablonski diagram* (Figure 2.1), which shows a series of increasing energy states as a stack of horizontal lines. Each energy level is in turn composed of a number of subenergy levels. There are two categories of excited states, characterized by different spin states of the excited electron — the singlet excited state and the triplet excited state. Most commonly, an excited electron occupies an excitation level within the singlet excited state (straight upward pointing arrows), and when it collapses to the ground state, energy can be given up as fluorescence emission (straight downward pointing arrows). Alternatively, energy can be given up as heat (internal conversion), in which case no photon is emitted (wavy downward pointing arrows). When excited above the ground state, there is a probability that an electron can also enter the triplet excited state through a process called intersystem crossing (diagonal wavy arrow). [34]

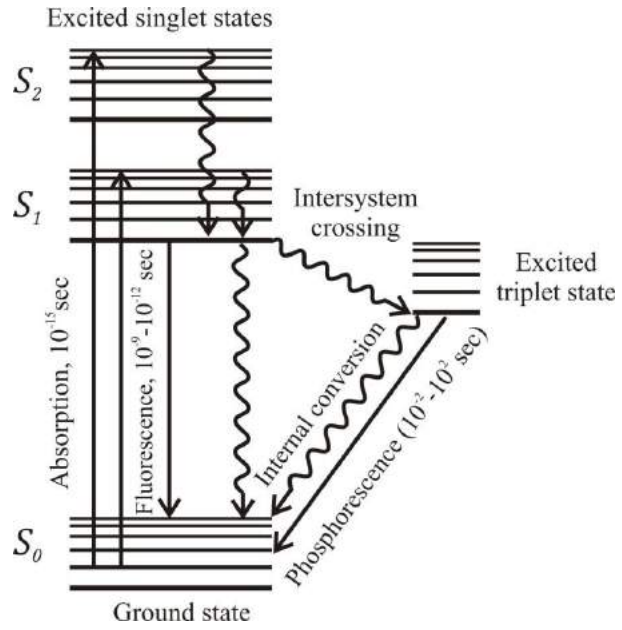

Fig.2.1 Schematic energy level diagram showing the excitation process of a molecule from the ground state, S_0, to an excited state, S_1.

2.3 Fluorescence induced by two photon absorption

Fluorescence imaging can be further enhanced by utilizing nonlinear excitation processes such as Two-Photon Absorption, where the excitation photon energy is less than the energy gap of the fluorophore. The molecular TPA property is defined as the electronic excitation that is induced by a simultaneous absorption of a pair of photons with the same or different

energy (Figure 2.2). This phenomenon was first predicted in 1931 by M. Göppert-Mayer [6] who calculated the transition probability for the absorption of two quanta of energy. In this process a photon first interacts with the molecule and promotes a transition from ground state to a temporary virtual state of energy above the ground state. This is not a real state of the molecule and it exists only for a short time interval (~10^{-15}–10^{-16}s for photon energies in the visible and near-IR ranges).[35] If during this interval of time other photon interacts with the molecule, the excited state can be achieved. The adjective "simultaneous" for TPA is used to indicate that the two photons interact with the molecule within the interval of time mentioned above and that no real states act as an intermediate state in this process.

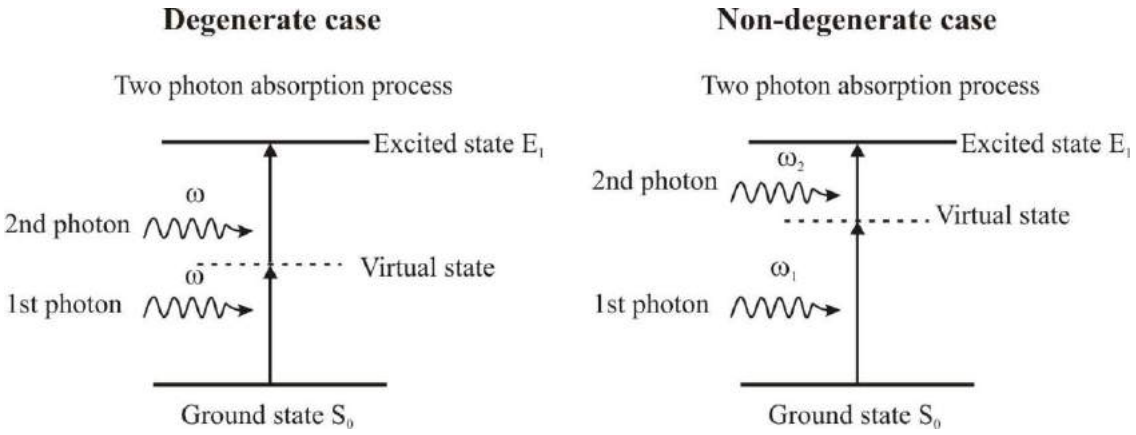

Fig. 2.2 Schematic energy level diagram showing the excitation process of a molecule from the ground state, S_0, to an excited state, E_1. The photons can have the same energy (degenerate case), or different energies (non-degenerate case).

Lasers emitting short pulses (nano, pico o femtosecond pulse widths) can excite fluorophores by two-photon absorption. If the laser intensity is high, a fluorophore can simultaneously absorb two photons to reach the first singlet state (Figure 2.2). This process depends strongly on the light intensity and occurs only at the focal point of the laser beam. This can be seen in the photograph, Figure 2.3, where emission is occurring only from a single spot within the sample. Fluorophores outside the focal volume are not excited.

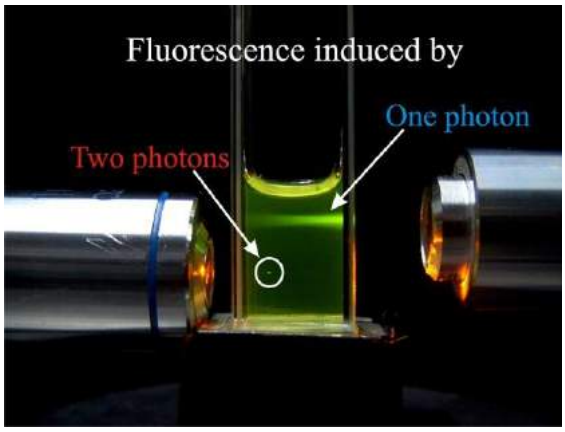

Fig. 2.3 Fluorescence induced by one and two-photon absorption in an organic material.

The TPA is a third-order non-linear optical process which is increased in proportion with the square of the light intensity. The magnitude of TPA can be quantified by introducing the parameter called *TPA cross section*. This parameter is usually expressed in Goppert-Mayer units: 1 GM = 10^{-50} (cm^4 s/photon).

2.4 Fluorescence quantum yield

The fluorescence quantum yield (Φ_F) is a very important characteristic of a fluorophore. This is defined as the ratio of the number of photons emitted to the number absorbed. Substances with the largest quantum yields, approaching unity, display the brightest emissions.

In this method it is necessary to use a reference sample whose quantum yield of fluorescence is known. By comparing the photoluminescence of the sample of interest with the photoluminescence of the reference sample it is possible to obtain the Φ_F for the sample.

The experimental setup for measuring the quantum yield of fluorescence is shown in Figure 2.4. It consists of a diode laser at 375 nm, diaphragm (D1) and two lenses (L1 and L2) which are used for collimating the laser beam incident on the sample placed in the center of an integrating sphere (model INS250 International Light Technologies) of 25.4 cm internal diameter; subsequently, a PMT (Hamamatsu R7400U series) is placed at 90° of the excitation beam and lock-in amplifier model SR830 from Stanford Research Systems to detect the fluorescence signal. The cell is placed outside and inside the sphere at positions 1 and 2 respectively, in order to detect only the fluorescence and not consider the excitation light transmitted by the sample and the background noise. Therefore, the differences

between the signal obtained in position 2 and the value obtained in the position 1 for each sample including the reference sample (*Fs* and *Fst* for the sample and reference, respectively) are used to calculate the quantum yield of fluorescence according equation 1.

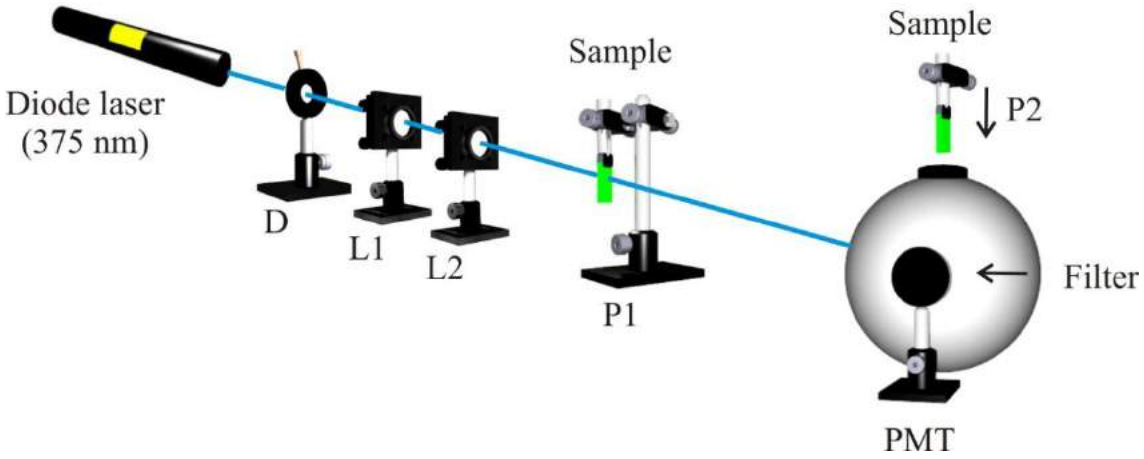

Fig. 2.4 The experimental setup for measuring the quantum efficiency.

$$\Phi_S = \Phi_{st} \frac{A_{st}}{A_S} \frac{F_S}{F_{st}} \left(\frac{n_S}{n_{st}}\right)^2 \qquad (1)$$

Where A_{st} is the absorption of the reference standard, A_s is the absorption of the sample, both at the excitation wavelength, Φ_{st} is the quantum yield, n_s and n_{st} are the refractive index of the sample and the standard refractive index, respectively.[36]

In general, rigid structures are essential for high fluorescence quantum yields and substituents such as NO_2 and heavy atoms will lead to low fluorescence quantum yields via intersystem crossing to a triplet state.[37]

The intensity of fluorescence can be decreased by a wide variety of processes. Such decrements in intensity are called quenching. Quenching can occur by different mechanisms; these include excited-state reactions, molecular rearrangements, energy transfer, ground-state complex formation, and collisional quenching. Collisional quenching occurs when the excited-state fluorophore is deactivated upon contact with some other molecule in solution, which is called the quencher. A wide variety of small molecules or ions can act as quenchers of fluorescence, for instance, iodide (I^-), bromide, oxygen, halogens, amines, and acrylamide. However, there are others factors that can affect the

emission spectral properties of fluorophores such as solvent polarity and viscosity, internal charge transfer, probe–probe interactions, probe conformational changes and the local environment (rigidity of the local environment), among others.[38]

Fluorescence emitted by almost all fluorescent dyes fades during observation. This phenomenon is called photobleaching and involves a photochemical modification of the dye resulting in the irreversible loss of its ability to fluoresce. Photobleaching affects the image formation process. Indeed, fluorescent dyes in the excited state may undergo chemical or biochemical reactions that lead to their rapid degradation and destruction and consequent loss of image quality during measurement. In a certain sense, fluorophores are consumed by being observed.

This shows that in confocal microscopy and TPM the photostability problem can have a severe impact on the image formation process. Even in TPM, despite the tight confinement of the excitation volume and the use of infrared light, the high peak power of the laser pulses may cause photodamage of the fluorescent probes being used. In general, the loss of fluorescence that comes along with photobleaching has the undesirable effect of reducing the signal-to-noise ratio and the quality of the collected images and data.

Several theories have been proposed to explain photobleaching. The main causes seem to involve photodynamic interactions between excited fluorophores and molecular oxygen (O2) in its triplet ground state and dissolved in the sample media.[39]

2.5 Techniques for measuring two-photon absorption cross section (Z-scan and TPEF)

Several techniques have been used to measure the two-photon excitation cross sections of various materials for more than two decades. The two main techniques for measuring σ_{TPA} are the Z-scan [40] and two-photon excited fluorescence (TPEF),[41] although others methods exist such as thermal lensing[42] and photoacoustic measurements.[43]

Z-scan is a direct method to determine the non-linear absorption of materials; this technique consists in monitoring changes in the transmittance of the sample when the incident intensity of a train of laser pulses changes (this can be achieved by varying the position (position z) of the sample in the vicinity of the focal plane of a lens, hence the term “Z-scan”). See Figure 2.5. The Z-scan curve obtained is symmetrical with respect to the focus

(z = 0), where it is possible to obtain a minimum in the transmittance (multiphoton absorption).[40] The normalized transmittance is given by:

$$T(z) = 1 - \frac{1}{2^{3/2}}\sigma_{TPA}\,\frac{CN_A}{\hbar\omega}\,\frac{I_0 L_{eff}}{1+(\frac{z}{z_0})^2} \qquad (2)$$

where C is the concentration of the material in solution (usually organics are characterized in solution), N_A is Avogadro's number, ω is the optical frequency of the laser, z_0 the Rayleigh range of the beam, I_o the peak intensity at z =0 and L_{eff} the effective thickness of sample. With this technique σ_{TPA} is determined straightforwardly when short laser pulses (femtosecond or picosecond) are employed by just fitting experimental data to the expression given above. The use of nanosecond pulses can lead to an overestimation for the σ_{TPA} since other effects different than simultaneous TPA can also be present.

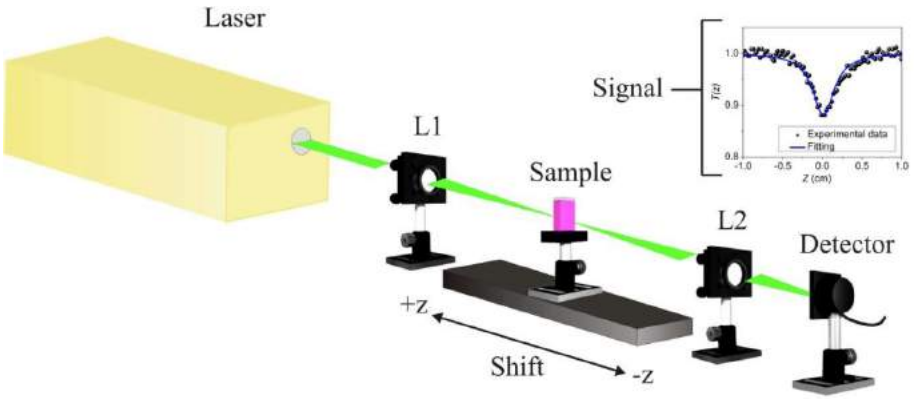

Fig. 2.5 Z-scan technique. The pulse energy of a train of pulses is kept constant, but changes in intensity are achieved by moving the sample along the propagation direction Z. The transmittance is measures at each Z position of the sample.

The TPEF (Two-Photon Excited Fluorescence) technique is another procedure for determining σ_{TPA} and consists in measuring the fluorescence signal generated from a sample after it is excited by TPA. From the two-photon fluorescence signal a TPE (two-photon fluorescence excitation) cross section σ_{TPE} can be determined. The σ_{TPE} is linearly proportional to σ_{TPA} with the constant of proportionality being the fluorescence quantum efficiency (Φ_F) of the sample

$$\sigma_{TPE} = \Phi_F\,\sigma_{TPA}. \qquad (3)$$

Several variants of this experiment have been developed since it was first reported by Xu and Webb.[41] However, if a standard calibration sample of known σ_{TPE} and spectra is

available, then the simplest approach is to compare the two-photon excited fluorescence excitation spectra of the sample with this reference sample tested under identical conditions. Then, with this method it is possible to cancel automatically a large number of variables. For instance, it is not necessary to know parameters related to the excitation (pulse energy, pulse duration, and temporal intensity distribution).[44] The equation to calculate the TPA cross section is given by:

$$\sigma_{TPA}(\lambda) = \sigma_{TPA(ref)}(\lambda)\frac{\Phi_{ref}(\lambda)C_{ref}}{\Phi(\lambda)C}\frac{\langle F(t)\rangle_{ref}}{\langle F(t)\rangle}\frac{n_{ref}}{n} \qquad (4)$$

where C denotes the concentration of solution, $\langle F(t)\rangle$ is the time averaged fluorescence emission, n is the refractive index of the sample, and λ is the excitation wavelength. The subindex ref denotes the parameters for the dye used as references or standard. Representative experimental setup of TPEF technique is shown in Figure 2.6, the laser beam of a Ti:sapphire laser (100 fs per pulse, repetition rate of 80 MHz, tunability 740–820 nm) is focused into a quartz cell of 1 cm path length (containing the samples) by using a 5 cm focal-length lens. The TPEF emission was collected using a lens in an epi-illumination configuration (in a perpendicular direction with respect to the excitation beam) and focused into the input slit of a spectrometer.

The principal drawback of the TPEF method is that, obviously, it cannot be used for non-fluorescing or weakly fluorescing materials. TPEF is also difficult to implement in compounds that exhibit wavelength-dependent emission (in either band shape or efficiency) or dual emission, as well as in solid-state samples. In those cases the use of Z-scan is more convenient.

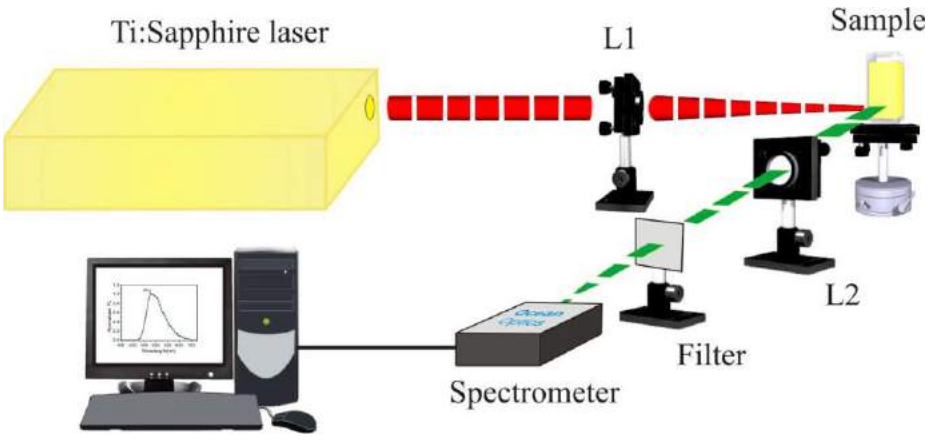

Fig. 2.6 Typical TPEF experimental setup to measure the σ_{TPA} in organic materials. The photoluminiscense promoted by the absorption of two photons is detected from a solution of the sample under test and compared with that from a standard tested under the same experimental conditions.

The TPA action cross-section is the most commonly used parameter for characterizing bioimaging TPA fluorophores. However, the action cross-section does not consider the impact of photostability. Low photostability will significantly limit the applications of a fluoroscent probe in fluorescence imaging. For this reason, X. Wang and coworkers developed a figure of merit to evaluate a TPA fluorescent probe based on the action cross-section and photodecomposition quantum yield. [45]

The figure of merit (*FM*) is defined as:

$$F_M = \sigma_{TPA}\frac{\Phi_F}{\Phi_d} \tag{5}$$

where σ_{TPA} is TPA cross-section, Φ_F is fluorescence quantum yield, and Φ_d is photodecomposition quantum yield. The incorporation of the photodecompostion quantum yield in the F_M provides a more comphensive picture of a fluorophore for bioimaging and provides a value by which all fluorescent probes for two-photon fluorescence microscopy can be compared.[37]

The values of photodecomposition quantum yields, Φ_d, can be calculated according to equation 6:

$$\Phi_d = \frac{(A_1 - A_0)N_A}{10^3 \times \varepsilon \times I \times \left(1 - 10^{\frac{A_1+A_0}{2}}\right)(t_1 - t_0)} \tag{6}$$

where Φ_d is the photobleaching decomposition quantum yield, A_1 is the absorbance maximum at t_1, A_0 is absorbance max at t_0, N_A is Avogadro's number, ε is molar absorbance in $M^{-1}\cdot cm^{-1}$, $t_1 - t_0$ is time exposed (s), and I is the intensity of laser in photon$\cdot cm^{-2}\cdot s^{-1}$.

A wide range of organic molecules with large TPA activity have been studied experimentally employing Z-scan and TPEF techniques. In the following section we present some representative samples.

2.6 Structure-Property Relationships for fluorescent organic materials

Organic molecules, with the capability of tailoring their linear and nonlinear optical properties by molecular structure modification, can be utilized in fluorescence sensing and

biological imaging. Many organic molecules and polymers having electronic π-conjugated systems in their structure have shown large nonlinear optical properties. So far, the largest values of σ_{TPA} reported in the literature are in the range of $10^2 – 10^4$ GM. The number of examples within this range of nonlinearities has increased notably during the last three decades, and scientists have designed different families of molecules to achieve these values. A large number of scientific articles that report new TPA organic fluorescent materials are oriented toward imaging *in vivo* or *in vitro* of bio specimens, as well as the diagnosis of diseases. For these applications it is necessary to have organic molecules with high quantum yield of fluorescence and large TPA cross section values, in addition low cell-toxicity and compatibility with aqueous media. In particular, the architecture of organic molecules that have been studied and investigated for their two-photon absorption and fluorescent properties could be classified in two principal groups: a) linear and b) two-dimensional architectures. For both structures there are some requirements for maximizing the TPA cross-section response: a long conjugated π-backbone system with a planar conformation; the presence of electron donor (D) and electron acceptor (A) groups able to promote an intense displacement of charge during the transition from the donor-centered HOMO (highest occupied molecular orbital) to the acceptor-center LUMO (lowest unoccupied molecular orbital).[12] The energy difference between the HOMO and LUMO is the optical gap corresponding to the excitation transition promoted by TPA. Depending on the symmetry of the organic molecule, this gap can be the same or different from that promoted by one photon transition (linear absorption). For instance, in centrosymmetric molecules the maximum TPA appears usually at higher energies than the peak of one-photon absorption transition. This is because one-photon and two-photon transitions are regulated by different dipole selection rules.

In the case of chromophores with linear architecture such as polymers and small molecules, effective molecular architectures have been used to enhance the two-photon absorption. Arrangement such as donor-bridge-acceptor (D-π-A) dipolar structures (Figure 2.7a), donor-bridge-donor (D-π-D), acceptor-bridge-acceptor (A-π-A), donor-acceptor-donor (D-π-A-π-D) and acceptor-donor-acceptor (A-π-D-π-A), the latter four corresponding to quadrupolar structures (Figures 2.7b and 2.7c), have been designed and synthesized.[44,46,47] The appropriate donor-acceptor substitution in organic π-systems can enhance the TPA activity through an increase in the transition dipole moment or the dipole moment difference between the ground state and excited state. Experiments indicate that quadrupolar architectures in some cases are more efficient that dipolar ones. For quadrupolar systems the best results have been obtained for architectures containing donor groups in the periphery and acceptor in the core. For molecules that possess two dimensional structures the best results correspond to architectures containing a core with accepting properties and donor groups in a multi‐branched configuration (Figure 2.7d). These type of structures have octupolar response A-$(\pi\text{-D})_3$. Typical D groups are amino moieties as diphenylamino (NPh_2), dimethylamino (NMe_2) or diethylamino (NEt_2) which

are the most employed, while some of the fragments used as A are anthracene, fluorine, benzothiadiazole, triazine, porphyrin or BODIPYS derivatives. For the π-bridge between D and A is common to utilize aromatic (phenyl or fluorene) or heteroaromatic rings (thiophene) to favors the planar structure. However, some reports indicate that carbon triple bond is an excellent π−bridge.

Organics systems as fluorene based molecules and polymers, porphyrin, BODIPYS, dendrimers, etc. have large TPA activity with linear and two-dimensional designs.

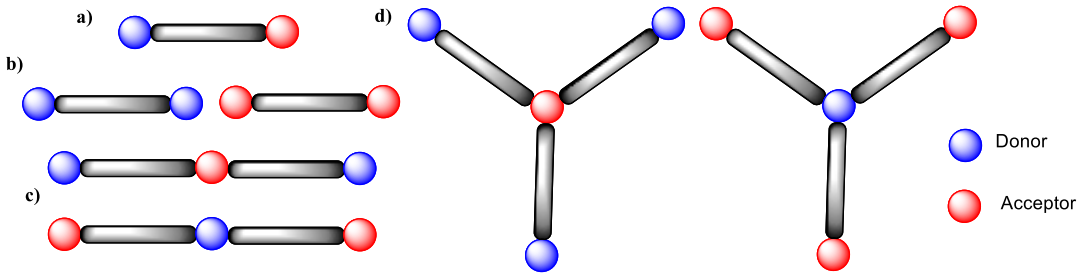

Fig. 2.7 Molecular architectures for optimization of TPA responses in organic compounds: a) linear, b) dipolar c), quadrupolar and d) octupolar.

2.7 Recent Efforts in Two-Photon Materials Development

Upon excitation, molecules with TPA properties experiment substantial intramolecular charge transfer (ICT) over the π-backbone, producing a high σ_{TPA}. Enhancement of the σ_{TPA} is achieved with a correct design of the molecular structure able to modify properly the ICT. The environment is a factor that can affect the ICT process and in turn the nonlinear optical response. For instance, the linear TPA dye **5** (see Figure 2.8 for a collection of TPA dyes with linear molecular structure) having dipolar architecture showed intense solvatochromic effect such that in cyclohexane (non-polar solvent) solution exhibits a large σ_{TPA} value of 6670 GM which is reduced in DMF (high polar solvent) to 1450 GM. In low polar solvents, such as toluene, linear quadrupolar structure **9** showed σ_{TPA} of 7080 GM while a two−dimensional molecule **13** (see Figure 2.9 for a collection of TPA dyes with two-dimensional molecular structure) has acceptable σ_{TPA} of 5300 GM. Other two−dimensional structures show much higher optical nonlinearities than linear structures. An example of the latter is the dendrimer with quadrupolar architecture (**19**) which in solution exhibits interesting value of 56000 GM.

It must be observed that in general the studied molecules are hydrophobic and soluble only in highly toxic solvents. To emphasize this fact, Table 2.1 summarizes the main optical properties of the molecules shown in Figure 2.8 and Figure 2.9 and the cases in which the

molecules can be processed into nanoparticles (NPs) susceptible to be suspended in biocompatible media, i.e., aqueous solutions.

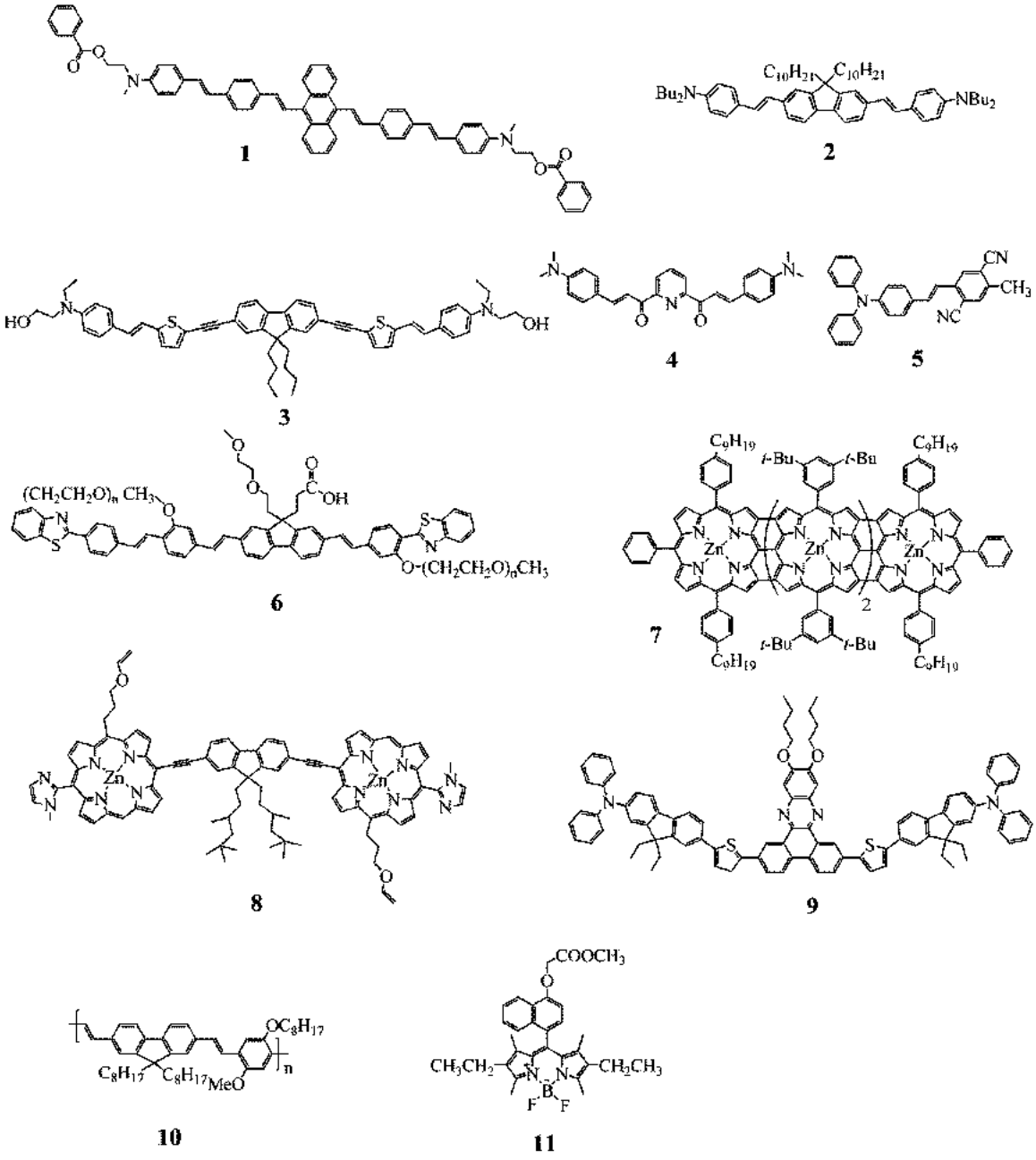

Fig. 2.8 Linear structures of efficient organic TPA molecules.

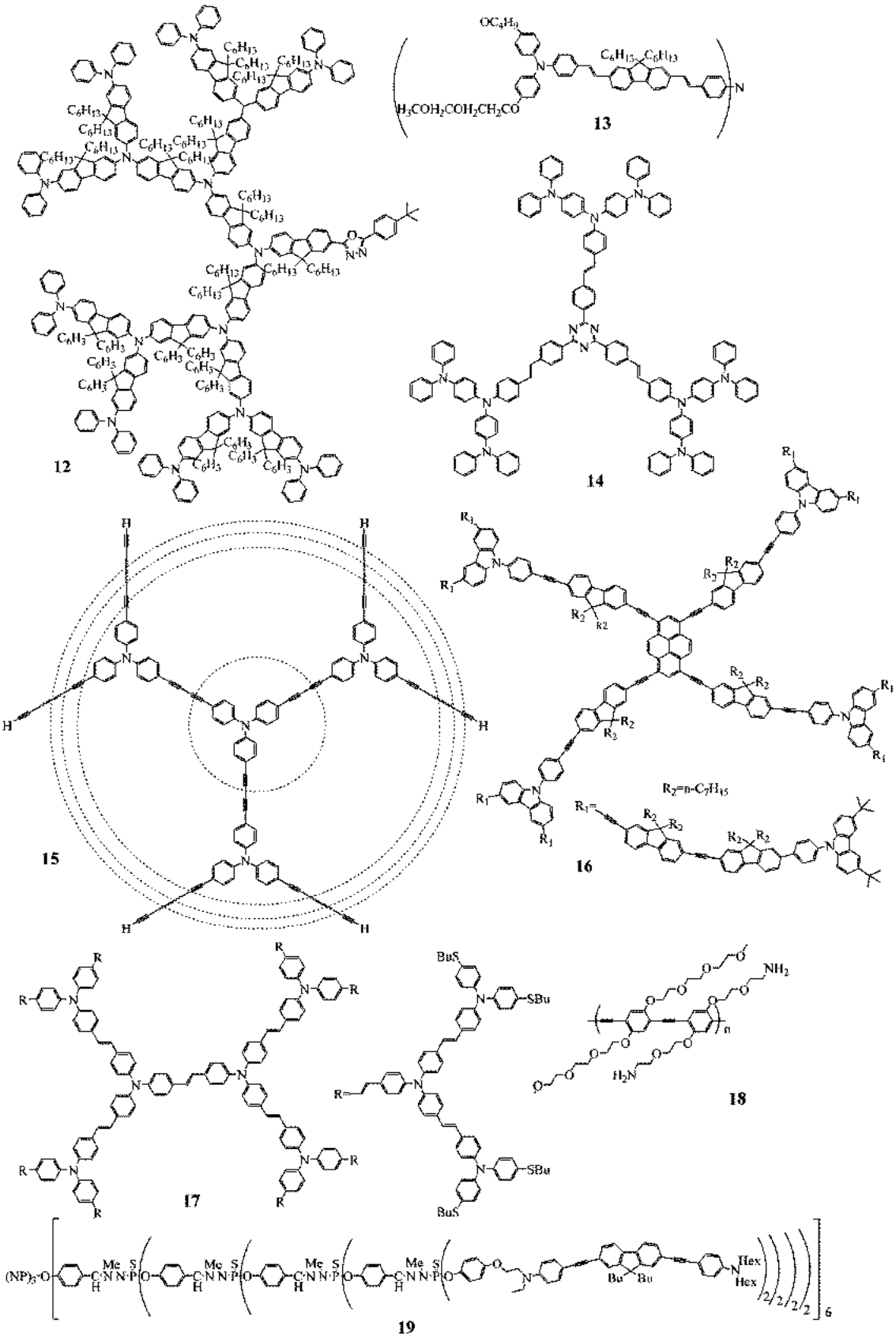

Fig. 2.9 Two-dimensional structures of efficient organic TPA molecules.

Table 2.1 TPA properties of organic materials are shown in Figure 2.8 and Figure 2.9. The properties are presented for materials in molecular solution and in the form of nanoparticles.

	Quantum yield (Φ_F)	**σ_{TPA} (solution)** GM/technique	**σ_{TPA} (NPs)** GM/technique	**Reference**
		Linear structures		
1	0.025 (in solution) 0.13(NPs)	172 / TPEF	217	[48]
2	1 (solution) 0.49 (SNPs)	~400/TPEF	-	[49]
3	-	1200	8000000	[32a]
4	0.082 (solution)	5250 /TPEF	-	[50]
5	0.805 (solution)	6670 /TPEF	-	[51]
6	~0.5 (aqueous solution) 1.0 (solution)	3000 ACN/TPEF ~6000 Water/TPEF		[52]
7	-	93,600/Z-scan	-	[53]
8	0.017 (solution)	1.0×10^6 /TPEF	-	[54]
9	~0.25 (in toluene) 0.08 (SNPs)	~7080/TPEF	6 800	[55]
10	-	-	200000 *	[56]
11	0.99 (solution)	128	-	[57]

Table 2.2. Continued

	Quantum yield (Φ_F)	**σ_{TPA} (solution)** GM/technique	**σ_{TPA} (NPs)** GM/technique	**Reference**
Two-dimensional materials				
12	0.43	2990 /TPEF	-	[58]
13	0.86 (solution) 0.56 (NPs)	5300 /TPEF	2790	[59]
14	0.24 (TNP0), 0.25 (NPs)	TPEF	2015 (FTNP0, with DSPE-PEG) 2241 (BTNPs, without DSPE-PEG)	[60]
15	0.57	9068 /TPEF	-	[61]
16	~0.49	25000 /TPEF	9750	[62]
17	0.55	11000 /TPEF	-	[63]
18	0.09 (CPNs)	-	11 000*/TPEF	[64]
19	0.48 to 0.75	~56 000 GM/TPEF	-	[65]

* Two-photon action cross section

Usually organic molecules and polymers comprise π-conjugation in their structures, as those shown in Figure 2.8 and Figure 2.9, exhibit one-photon excitation (linear absorption) in the UV-Vis of the spectrum. According to these range of energies, the maximum two-photon excitation (assuming roughly that the peak of the two-photon absorption spectrum is located at twice the wavelength of the one-photon absorption) occurs in the Vis-IR range. For biomedical applications the interest is focused in chromophores with TPA in the red and near-infrared region (650–1000 nm). Effective two-photon excitation at this range of wavelengths is observed with organics with relatively small optical band gap. Further, the effectiveness in nonlinear absorption must be accompanied by a second molecular functionality. For instance, when a molecule o polymer is intended as a fluorescent label or contrast agent in multiphoton microscopy, it needs to exhibit a large value of quantum yield

of fluorescence, Φ_F. This is not always achieved, as it can be observed in Table 2.1. Sometimes, large σ_{TPA} values are obtained in detriment of Φ_F. In these cases, or in other cases where the needed functionality is other than fluorescence, the energy transfer concept can work satisfactorily. For instance, an effective fluorescent dye (energy acceptor) with poor two-photon activity is indirectly excited through resonant energy transfer from an effective TPA dye unit (energy donor).

CHAPTER 3

Organic nanostructured materials with TPA properties

Intense studies have been focused on developing efficient TPA organic fluorescent molecules that can be excited in the 650-1000 nm region, since they offer potential application in two-photon microscopy (TPM) and photodyamic therapy.[11] For these kind of applications it is mandatory that the molecules show excellent TPA activity in aqueous media, however, most of them are hydrophobic and those that are soluble in water commonly exhibit low values of σ_{TPA} and Φ_F.[41,66] The hydrophobic nature of the TPA chromophores means that, in some cases, organic polar solvents as dimethylsulfoxide (DMSO) or dimethylformamide (DMF) are required. These and other solvents imply high cytotoxicity. To circumvent these limitations, nanoscience has recently provided methods to bring organic molecules into biological media such as water. Different fabrication strategies have been developed and widely applied for obtaining organic nanoparticles in aqueous media with interesting morphologies and optical properties. Reprecipitation (RP),[67] self-assembly,[68] ion-association,[69] condensation,[70] microemulsion[71] and laser ablation (LA)[72] are some methods used to fabricate O-NPs. For the preparation of O-NPs comprising luminescent properties the most commonly employed methods are RP and ME.

First, in this section a classification of fluorescent nanostructures will be provided. Also some examples of organic fluorescent nanostructures and the methods used in this dissertation to incorporate hydrophobic materials into aqueous suspensions are presented.

3.1 Fluorescent nanostructures

There are many classifications of fluorescent nanostructures according to the compositions, structure, fluorescence mechanisms and applications in bioimaging; however, here we present the classification proposed by M. Chen and M. Yin.[20] They divided the fluorescent nanostructures into three categories, i.e., organic, inorganic and hybrid (organic/inorganic) (Figure 3.1). Among all fluorescent nanostructures used in bioimaging, organic ones are the most widely studied due to their rich chemical structures, easy chemical modification and high fluorescence quantum yield (Φ_F). Generally, these organic nanoparticles include carbon-based fluorescent nanostructures, fluorescent macromolecules, fluorescent polymeric nanoparticles, fluorescent supermacromolecular nanoassemblies and aggregation-induced emission fluorophores.

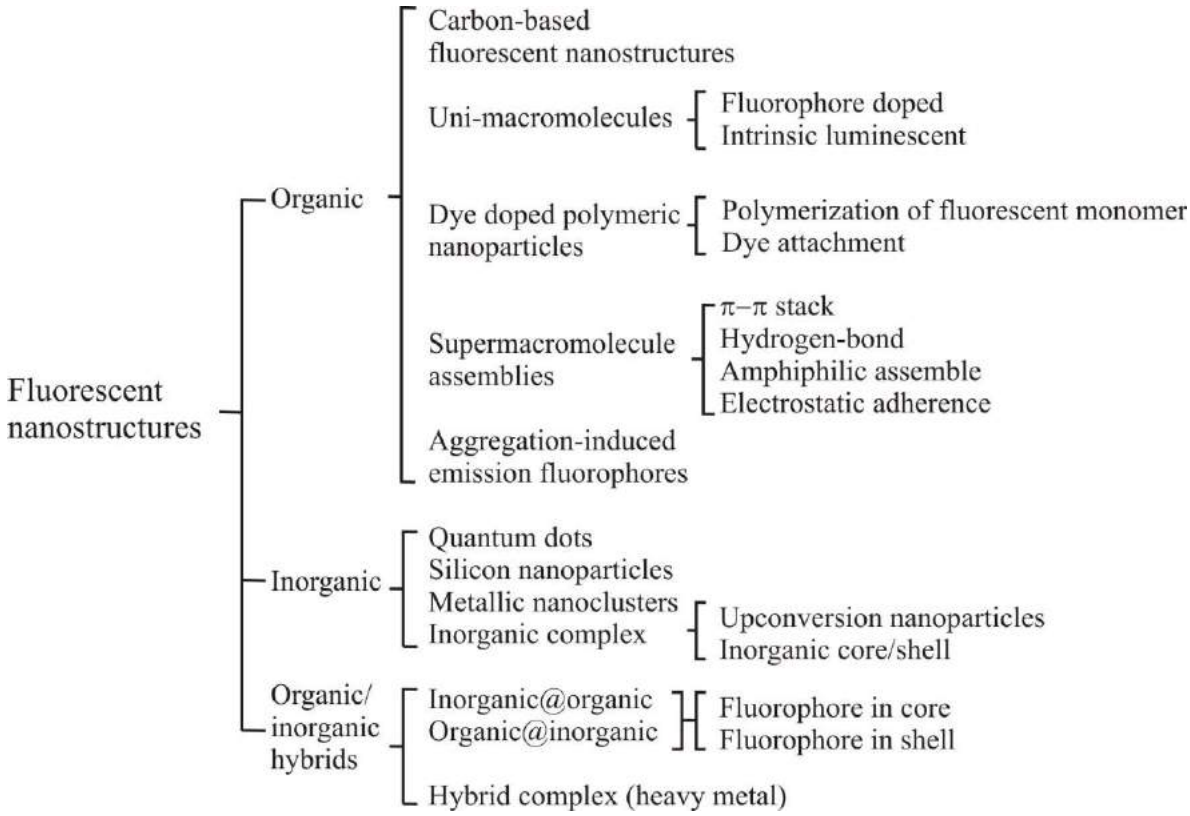

Fig. 3.1 Classification of fluorescent nanostructures based on their different chemical structural compositions according to M. Chen and M. Yin.

Particularly, organic fluorescent (supermacromolecular nanoassemblies) and hybrids nanoparticles (flurophore in core and silica in shell) are of interest for this work. These nanoparticles have fluorescent units with amphiphilic structures that can self-assemble into micelle-like aggregates, which result from the intermolecular interaction within hydrophobic and hydrophilic moieties, respectively. **Nanoaggregates**, **NPs-surfactant**, nanoparticles covered by a biocompatible polymer or copolymer (**NPs-PEG**) and nanoparticles produced from laser ablation (**NPs-LA**) belong to this group (their fabrication methods are discussed below). Organic/inorganic hybrid fluorescent nanostructures are another interesting nanoparticles, they combine multiple constituents into a single nanostructure to improve the application in bioimaging. The core and shell segments alternatively contributed to the desired fluorescent properties or acted as protecting agents of matrix or scaffold, which thus offers better functionalization and biocompatibility. Fig. 3.2. The doping of fluorescent TPA chromophores into silica NPs is also well-established in the literature. The fabrication of these fluorescent silica nanoparticles (**FSNPs** or **NPs-**

ME) is performed by using a microemulsion method. The advantages of **FSNPs** are their optical transparency, non-antigenicity, and rich surface chemistry for facile bioconjugation. The silica shell protects the dyes from photobleaching and prevents their interaction with the biological environment. The absorption and emission of the nanoparticles are determined by the properties of encapsulated fluorophores. One of the major disadvantages of this type of nanoparticles is the phenomenon of aggregation induced fluorescence quenching of the loaded dyes.[2] Organic chromophores can also be covalently encapsulated in silica nanoparticles.

Fig. 3.2 Architectures of organic fluorescent nanostructures and their fabrication methods. NPs-PEG could have different functions in the block sections or simply to self-assemble into uniform structures and silica shell in FSNPs acted as protecting agents of matrix or scaffold, which thus offers better functionalization and biocompatibility.

3.2 Fabrication methods of organic fluorescent nanostructures

Reprecipitation and microemulsion are the methods more common to fabricate organic nanoparticles (**O-NPs**) used as contrast agents in fluorescence microscopy. There are other methods to fabricate organic nanoparticles, but they have not been utilized in fluorescence microscopy. For example, to the best of our knowledge, there are no reports of the use of contrast agents (organic nanoparticles) fabricated by laser ablation method.

All fabrication methods of organic nanoparticles allow obtaining a wide distribution of sizes that can be finely adjusted with the preparation conditions (reprecipitation and microemulsion method) or tuning the laser wavelength, pulse width, fluence, and the number of laser shots (laser ablation). The morphology of the O-NPs obtained by reprecipitation method differs according to the molecule used, these NPs can have irregular shape with amorphous structure[73] and some particular cases ordered structures (nanocrystals).[74] Some general characteristics of nanoparticles fabricated by LA, RP and ME methods are summarized in Table 3.1 and a more detailed description of each method

is presented in later sections. It is important to note that this table contains only few of the properties of O-NPs produced by LA since so far the number of studies in this topic is very limited. Thus it results of interest to get additional insight in some of the characteristics of O-NPs fabricated by LA and comprising nonlinear chromophores intended for their use in biophotonic applications.

Table 3.1. Characteristics of organic nanoparticles produced by laser ablation (LA), reprecipitation (RP) and microemulsion (ME) methods.

Characteristics	Laser ablation (LA)	Reprecipitation (RP)	Microemulsion (ME)
Preparation time	0.5-3 h	4 h	24 h+ purification time
Morphology	Irregular,[75] triangular and hexagonal shapes,[76] nanocubes [77,78]	Irregular or spherical [79-81]	Spherical [49]
Structure	Amorphous or crystalline[82,83]	Amorphous or crystalline[67,79,84]	Amorphous
Size distribution	Medium[75,76]	Wide[80,85]	Narrow [49]
Size tunability	Easy[a] [72,83]	Easy[86]	Easy[87,88]
Stability	Stable fluorescence [a89]	Stable fluorescence[79]	Stable fluorescence[90,91]
Aggregation	Low[72,76,92]	Low-medium [93]	Medium but it can be reduced by adding inert functional groups to the surface of O-NPs[94-96]
Surfactant	No necessary[97,98]	No necessary[79,99]	Removed after purification
Coupling to specific biomolecules	Not reported	Possible [60]	Relatively easy bio-conjugation [28,49,100]
Cell penetration	Easy [a101]	Easy [74a)]	More difficult without biomolecule [28]
Toxicity	Dependent on amount of surfactant and material[a101]	Dependent on amount of surfactant and fluorophore[102]	Very low [102,103]
Nonlinear optical properties	Not reported	σ_{TPA} ~100-2000 GM [48,60]	σ_{TPA} ~217-1200 GM[32]
Fluorescence images	No reported for O-NPs and there is only one report for inorganic NPs. [a101]	Good quality [81,99,105]	Acceptable quality without biomolecule [28,106]

[a] Property reported from inorganic NPs

3.2.1 Laser ablation method to produce organic nanoparticles

Pulsed laser ablation is a simple, clean, flexible and promising technique because of its ability to ablate almost all kinds of materials (metals or organic compounds) and obtain various compositions, morphologies (spherical nanoparticles, nanocubes, nanorods, etc.) and structures (amorphous or crystalline).

In this work, I am interested in the method known as liquid phase pulsed laser ablation, in which a solid target is immersed in a liquid medium and the laser beam is focused through the liquid onto the target surface. Melting of the solid is a necessary condition for the formation of nanoparticles under ablation in liquid environment. This condition is obtained under sufficiently high laser fluence and depends on the absorptivity of the material at the laser wavelength. This technique allows controlling the growth process by manipulating parameters like irradiation time, duration, energy density, wavelength, etc. The final product is usually obtained without any byproducts and therefore no need for further purification. However, in some cases it requires a minimum amount of chemical species (surfactant) for synthesis compared to the conventional chemical process.

There are two laser ablation mechanisms to fabricate nanoparticles in a solvent: photothermal for nanosecond laser ablation and photomechanical for femtosecond ablation. For nanosecond photothermal ablation in a solvent, rapid temperature elevation upon pulse excitation is compensated by a cooling process due to thermal diffusion to the solvent, and its balance gives the transient temperature determining the nanoparticle size. Higher fluence gives higher effective transient temperature, leading to efficient fragmentation to smaller particles. Figure 3.3a. In the case of femtosecond irradiation, multiphoton absorption leads to very rapid increase in molecular and lattice vibrations giving transient high pressure in the irradiated area. As a result explosive mechanical fragmentation is started before thermal equilibrium with the solvent, leading to the small nanoparticles. Figure 3.3b. T. Asahi and co-workers described nanoparticle formation of quinacridone in water and they presented results about nanoparticles produced from several organic compounds including C60, and an anticancer drug.[72,76,89,97,107,108]

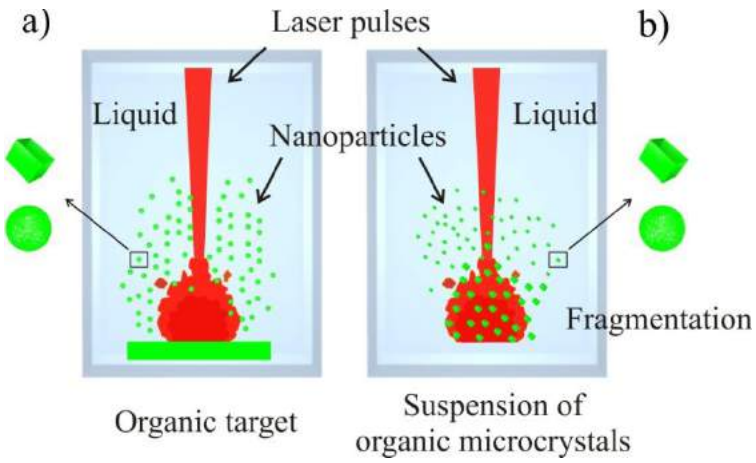

Fig. 3.3 Fabrication method of organic nanoparticles utilizing laser ablation of amorphous target (a) or microcrystals in water (b), where the bulk solids are converted directly into nanoparticles which are caught by water and stabilized as nanocolloids.

3.2.2. Reprecipitation method to produce organic nanoparticles

From the three preparation methods schematized in Figure 3.2, the reprecipitation technique is the most facile and commonly used to assist the formation of nanoparticles in the aqueous medium.

In this method, a small amount of concentrated stock solution of the target compound is injected rapidly into a vigorously stirred poor solvent. The great disparity between the solubilities of the target compound in the good and poor solvents, and the miscibility between the two solvents are essential for this method. The rapid mixing of the stock solution and the poor solvent changes the micro-environment of the target compound molecules. The molecules are exposed to the poor solvent surroundings in a very short time, inducing the nucleation and growth of the molecules to nanoparticles or nanocrystals. The size and morphology of the resulting nanoparticles can be controlled by varying the reprecipitation conditions, i.e., by tuning concentration, temperature, stirring speed, or adding surfactant. [109]

Typically, a target compound is first dissolved in a good water-miscible solvent such as alcohol, tetrahydrofuran or in acetone so that its concentration is of the order of mM. Next, a few microliters of the diluted solution is injected rapidly into a vigorously stirred poor solvent (10 ml, commonly water) at a constant temperature, using a microsyringe. Then, the solvent is evaporated and the target compound is reprecipitated in the form of organic

nanoparticles or nanocrystals dispersed in the aqueous medium, usually in a stable dispersion. Figure 3.4.[77]

The reprecipitation method induces the formation of nanoaggregates that can be stabilized with a surfactant agent (CTAB, triton X-100, albumin, SDS, etc.). The use of surfactants not only stabilizes the suspensions but also protects the surfaces of the formed fluorescent nanoparticles. The morphology of the organic nanoparticles obtained by reprecipitation method differs according to the molecule used, these NPs can have irregular shape with amorphous structure[73] and some particular cases ordered structures (nanocrystals).[74] Moreover, the lack of surface functional groups in O-NPs fabricated by reprecipitation greatly restricts their applications in specific targeted imaging. According to experimental results, the O-NPs fabricated by reprecipitation method not always tend to conserve the nonlinear properties showed by the corresponding molecules in solution, although in some cases they showed high cytotoxicity.[110,111] To further reduce the cytotoxicity of O-NPs and increase their circulation time *in vivo*, they can be encapsulated with polyethylene glycol (PEG). PEG is considered an ideal biocompatible polymer with low toxicity, high water solubility and negligible immunogenicity. Some attractive TPA chromophores as silole and hexa-peri-hexabenzocoronene (~1000 GM) have been covered with PEG derivatives to form NPs-PEG with nonlinearities ~350 GM.[36,112]

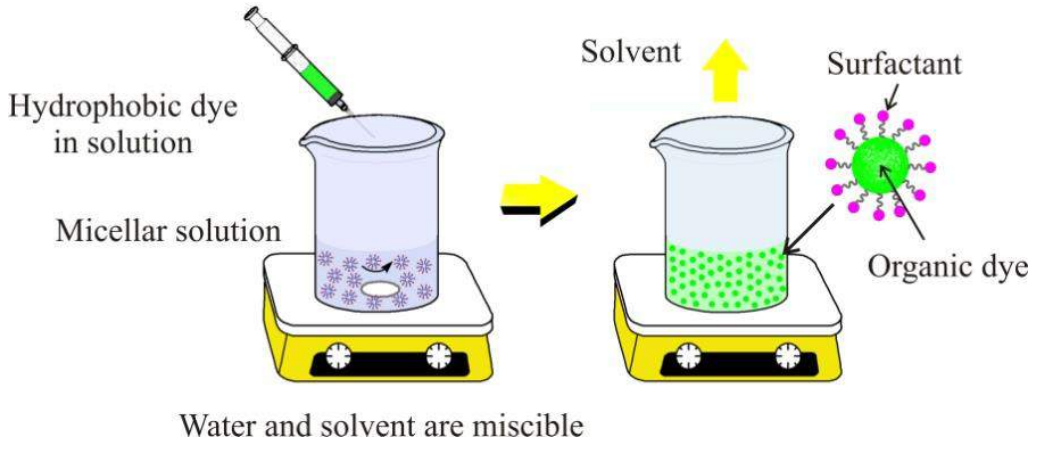

Fig. 3.4 Reprecipitation method.

3.2.3 Microemulsion O/W to produce organic nanoparticles

There are some methods of forming O-NPs from microemulsions, for instance, nanoparticles by polymerization, lipid nanoparticles, precipitation in aqueous droplets, direct solvent evaporation. Factors that should be taken into consideration when aiming to prepare O-NPs from microemulsion are: the physicochemical properties of organic substance, its solubility, desired characteristics of the final NPs (size, charge, encapsulating material), suitability of the system for the application goal (presence of solvents, surface active agents, polymer) and the techno-economical aspects of the chosen method. There are two models that have been proposed by the researchers in an attempt to explain the formation mechanism of the particles Therefore, prediction of the particle formation process outcome is very challenging, and many times is based on experimental knowledge only.[113]

The microemulsion method is a versatile technique which allows the preparation of a great variety of nanomaterials alone or in combination with other techniques. The precise control of all the parameters which can be varied affecting the final particle sizes and shapes is still a challenge, but the richness of the possibilities which can be achieved from nano- to macroscales is a big spur to work.[114]

The main advantage of the microemulsion method to prepare nanomaterials, over other preparation methods, is the ability to control the formation of different kind of core-shell(s) structures. The procedure used, shown in Fig. 3.5, consists of a two-step process: (1) formation of uniform particles (core) and (2) adding new reactants for the second reaction (shell). Hereafter, when I am speaking of microemulsion, I am referring to the method used to fabricate core-shell type nanoparticles, where the core is the fluorescent organic dye and the shell is the silica layer.

Silica emerged as an excellent option to replace surfactant molecules on the surface of hydrophobic materials, thus eliminating their cytotoxicity and improving their biocompatibility. Also silica has a number of advantages, mainly including: (1) The preparatiion processes involved are quite facile; (2) the thickness of silica shell can be tuned to the desired size; (3) silica is extremely stable; (4) silica surface is easily modified with a variety of functional groups using silane chemistry and commercially available organosilicon reagents for biotargeting. Therefore doped silica nanoparticles with fluorophores has been reported in the literature for solving this problem of hydrophobicity, now having these materials in the form of aqueous suspensions of nanoparticles in a manner that increases their stability, biocompatibility, allowing its application in the biological area.

In general, the synthesis of silica nanoparticles doped with an organic fluorescent dye is carried out starting from a micellar solution, which consists of a surfactant called Aerosol OT (AOT), a co-surfactant (butanol) and water. A micelle is a group of amphiphilic molecules, i.e., molecules which have at their ends a hydrophobic part and a hydrophilic part. These molecules are linked together by their hydrophobic ends forming a uniform space that tends to be spherical (micelle core), being this space wherein the hydrophobic dye is staying. Figure 3.5. Subsequently, adding silicon precursors as triethoxyvinylsilane (VTES) and 3-aminopropyltriethoxysilane (APTES) cover the organic dye with silica, to finally obtain the core-shell nanoparticles.

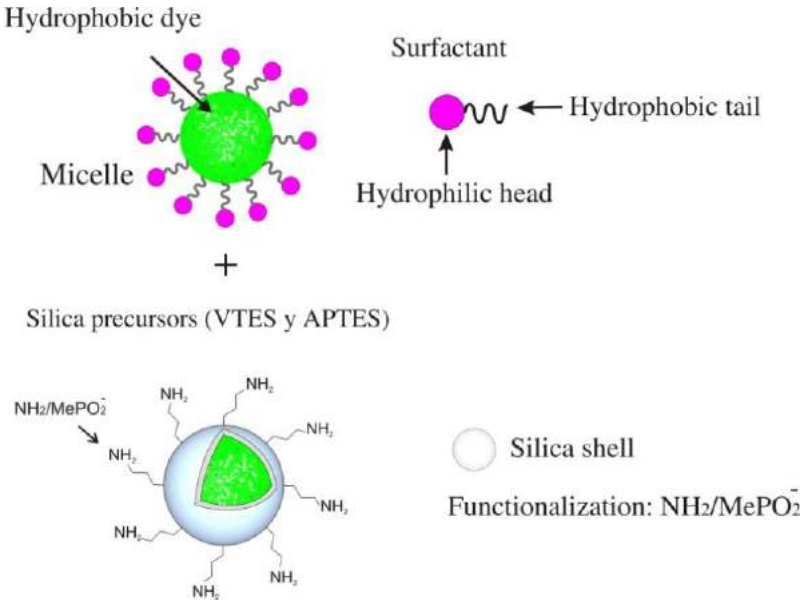

Fig. 3.5 Synthesis of silica nanoparticles doped with hydrophobic organic dyes.

Reactions describing the formation of the silica layer are shown in Figure 3.6. The first reaction step involves the hydrolysis of silicon precursor (VTES) to form highly reactive silanols which react with other silanol in the solution forming hydrogen bonds. Subsequently, the condensation of the silane coupling agents is carried out and the network (-Si-O-Si-) is formed, wherein each network element is covalently bonded by stable siloxane bonds (or oxane bonds). After, the APTES is added and it interacts similarly as in the procedure described for VTES, so, the coating formed with the resulting organosilane precursor is a thick layer of polymer due to organic reagents used (amino groups) that extend out from the surface. The layer thickness depends on the concentration of the silane coupling agents used in the reaction (VTES and APTES) and the amount of water present in the solution. Gelest reported the deposition of a silane coupling agent using a 0.25% aqueous solution, resulting in a layer thickness of 3-5 silanes, approximately.[115]

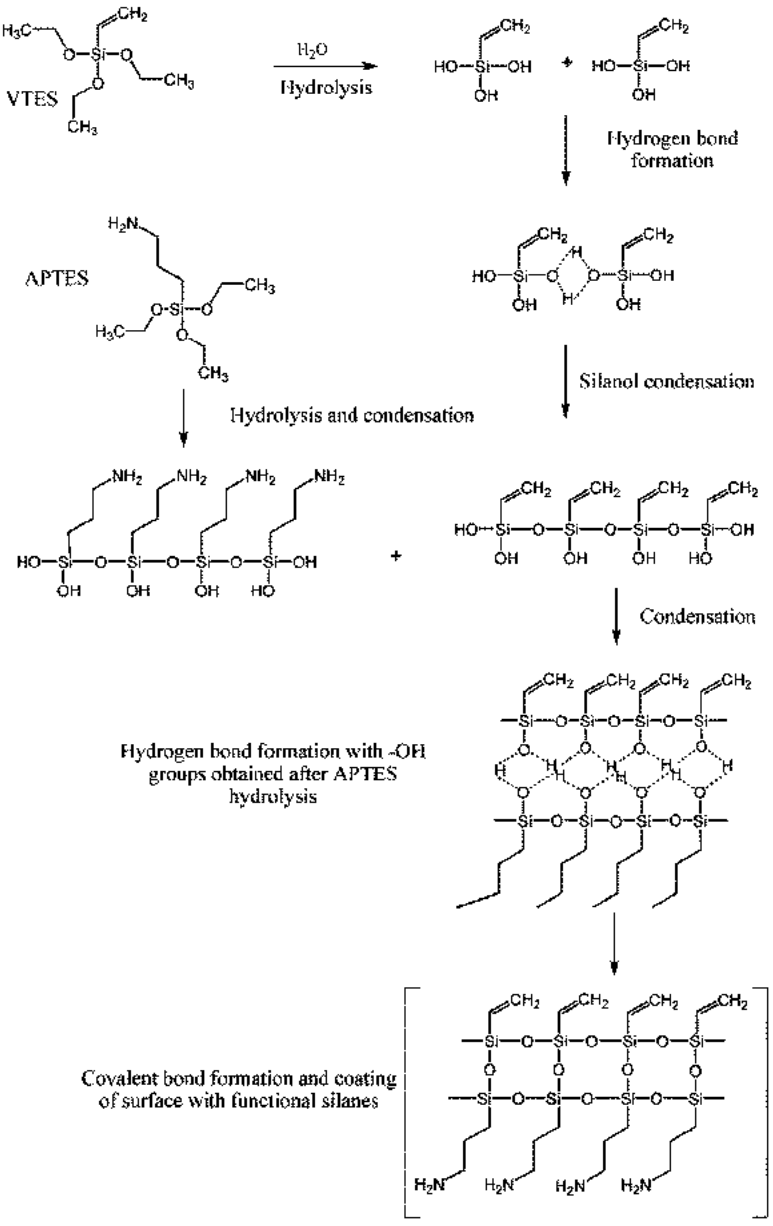

Fig. 3.6 Formation of the silica layer functionalized with amino groups.

3.2.3.1 Functionalization of fluorescent silica nanoparticles

The surface of silica nanoparticles can be easily modified by the addition of functional groups, thus providing a charge on the surface of the nanoparticle and consequently a change in behavior or suspension stability. By adding these functional groups, reactive sites with other molecules for specific applications are provided. Functionalization of the silica nanoparticles is typically performed using alkyl functional silanes. Appropriate selection of the functional or reactive group for a particular application can allow attachment of

proteins, oligonucleotides, whole cells, organelles, tissue sections or substrates. Organosilanes used for these applications include functional or reactive groups such as carboxyl, aldehyde, hydroxy, amino, epoxy, thiol, and even alkyl groups linking molecules through hydrophobic interactions, Figure 3.7. These reagents and many other silane derivatives are commercially available. 3-aminopropyltriethoxysilane (APTES) and 3-(trihydroxysilyl) propyl methylphosphonate monosodium salt solution (THPMP) are silane coupling agents used to functionalize the nanoparticles in this work.

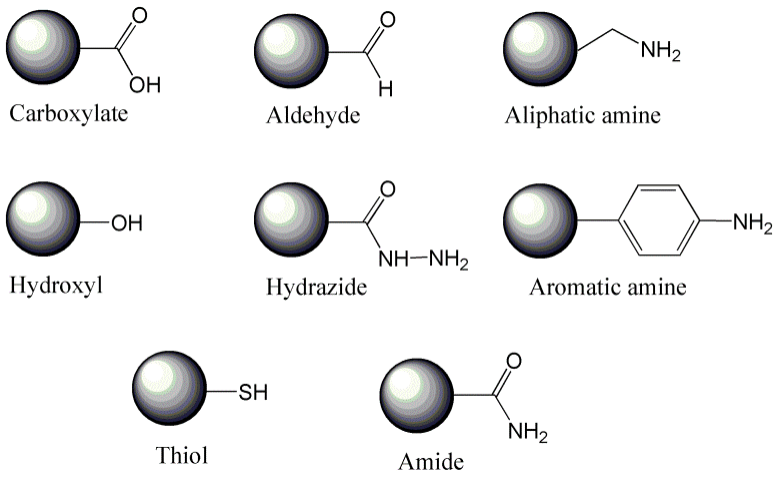

Fig. 3.7 Common functional groups on nanoparticles that provide the ability to couple to biomolecules.

3.4 Bioconjugation

Bioconjugation involves the linking of two or more molecules to form a novel complex having the combined properties of its individual components.[115] Bioconjugation has had a great impact over the years, making possible numerous applications such as modulation and monitoring of specific biological processes, detection or location specific substances or cancer cell lines. Fluorescent nanoparticles to be used in a biological environment need to be biofunctionalized and bioconjugated appropriately, which remains a significant challenge. Not surprisingly, a great deal of research work was carried out to make them not only biocompatible, but also to attach biological molecules in order to extend their applications into the life sciences. Sometimes, the internalization of nanoparticles into cells is severely limited by the low efficiency of uptake. Hence, in order to increase the internalization of nanoparticles, the nanoparticles surface is modified with a ligand known to be efficiently internalized by target cells.

After FSNPs and NPs-PEG have been modified with different functional groups, they can act as a scaffold for the grafting of biological moieties, such as peptides, proteins, sugars and polysaccharides, nucleic acids and oligonucleotides, lipids, and can be chemically bonded with nearly any other imaginable molecule, by means of standard covalent bioconjugation schemes, Figure 3.8, such as carbodiimide chemistry, disulfide-coupling chemistry and succinimidyl ester hydrolysis chemistry. Some techniques are reported and characterized, thus obtaining general protocols that may be useful to have excellent prospects of success in bioconjugation.[115]

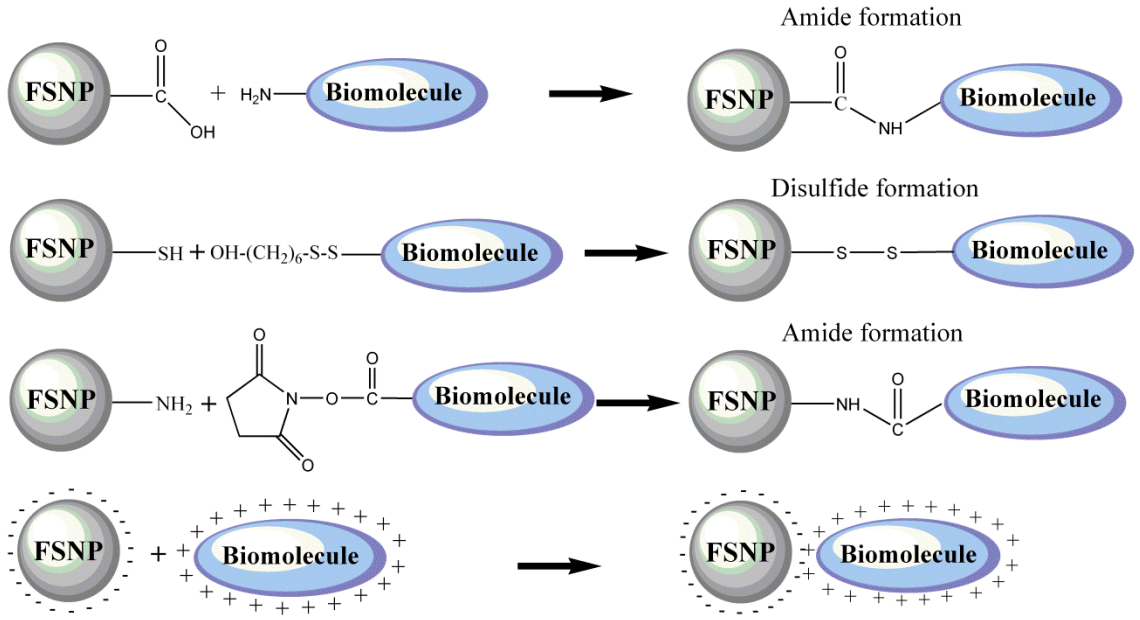

Fig. 3.8 Representative bioconjugation scheme for attachment of biomolecules onto the surface of silica nanoparticles.

Nanoparticles conjugated with a specific antibody, aptamer, peptide and protein have been documented for cancer cell targeting.[116] Over the last two decades, folic acid has been studied widely as a recognition element for imaging and cancer therapy because folate receptors (FAR) are up-regulated (over expressed) on a variety of human cancers, including cancers of the breast, ovaries, lungs, colon, endometrium, kidneys, brain, and myeloid cells of hematopoietic origin. The lack of folate receptors in nonproliferating normal cells differentiates them from tumor cells.[117]

Several studies about nanoparticles with folic acid have been reported, for example, Zhaowu Zhang and Jun Ai report the development of gold nanoparticles-folate conjugate system.[48,60] Moreover, Kai Li and et. al reported a strategy for one-step formation of

hydrophobic TPA chromophore-doped NPs with surface folic acid groups by encapsulating this chromophore in a mixture of 1,2-distearoyl-sn-glycero-3-phosphoethanolamine-N-[methoxy(polyethylene glycol)-2000] (DSPE-PEG2000) and DSPE-PEG5000-Folate.[91] Although these targeting systems have good biocompatibility and internalization efficiency, the large size of these macromolecule-based systems does not facilitate intravenous delivery.[118] Silica-modified gold nanorods,[119] albumin nanospheres,[120] Pluronic F127 magnetic nanoparticle clusters[121] and two-photon dye-doped mesoporous silica nanoparticles conjugated with folic acid also have been reported,[122] unfortunately the last nanoparticles, the grafting of folic acid enables the formation of charge transfer complexes between the two-photon dye and folic acid which leads to quenching of the fluorescence of the nanoparticles.

Section 4.3.3 presents the work performed in this dissertation concerning silica surface modification with carbonyl groups, addressing the bioconjugation of fluorescent nanoparticles with biological molecules and proteins as folic acid or transferrin, respectively. Moreover, thinking in future studies, FSNPs were functionalized with other groups as carboxyl and amide to inhibit their internalization into cells. Particularly, for FSNPs with carboxyl groups also can be used to couple with other molecules of biological interest.

CHAPTER 4

Fluorescent organic materials, photophysical characterization

As mentioned in Chapter 2, there are a variety of materials with significant TPA properties. In the search for materials with potential linear and nonlinear optical properties it resulted interesting to study a family of eight fluorescent borinates, considering that in the literature there are reports on boron containing fluorophores whose cross sections are between 325 and 1016 GM.[66,123,124] On the other hand, we decided to study four BODIPIES with tetraphenylethene (TPE) units introduced as periphery to the methylated BODIPY core. Recently, BODIPY has regained considerable research attention owing to its excellent photophysical properties. The third family under study in this work consisted in flourene-based compounds. Flourene is a moiety able to provide π-conjugation and intense fluorescent and nonlinear effects to a variety of molecules. For instance, nowadays many flourene-based polymers are fundamental for organic optoelectronic technology; similarly, they result very attractive for biophotonic applications. Conjugated polymers have also been employed for the synthesis of nanoparticles.[49,125,126] The advantage of employing this type of polymers as fluorescent probes is that they comprise TPA cross sections between two to three orders of magnitude larger compared with common dyes, and also exhibit low levels of aggregation-induced fluorescence quenching. In this work it is demonstrated that a flourene-based polymer is an excellent material for the fabrication of contrast agents for fluorescent microscopy. Finally, a novel fluorene-chromophore called BT2 was also studied. The results obtained from all materials are presented in this chapter. Reagents and equipment used to fabrication and characterization of fluorescent materials in solution and nanostructures is shown in Appendix A.

4.1 Borinates

4.1.1 Linear Optical Properties

Eight borinates (5**a**-5**h**) were synthesized by Cristina Jiménez from the group of Dr. Norberto Farfan (Facultad de Química, UNAM). These borinates contain an electronic π-bridge that connects a strong donor group ($–NEt_2$) in one terminal of the molecular structure with a variety of substituents R_1 located at the other end (see Figure 4.1). The photophysical properties of borinates are summarized in Table 4.1. The linear absorption and emission spectra for the boron complexes in THF solution are shown in Figure 4.2. These boron complexes have an intense absorption band from 402 to 425 nm, which is assigned to typical n $\rightarrow\pi^*$ electronic transition. In particular, compounds 5**g** and **5h**

possessing both the strong donor (–NEt_2) but different acceptor groups (–COOEt and –COOMe), showed a red shift $\Delta\lambda$ of 16 and 23 nm, respectively, compared with the absorption band of the borinate 5**a** (having a –H end group). Similarly, a shift of 23 nm was observed in the case of compound **5f** containing the –NEt_2 donor group in a quadrupolar architecture D–π–C=N^+–π–D. In the case of borinate **5e**, possessing a quadrupolar architecture with an –OMe group, the absorption band is similar to **5a**. It is also observed an increment of molar absorption (ε) in compounds with architecture D–C =N^+–A and surprisingly a reduction in compounds with D–C=N^+–D design. It is important to note that, after boron complexation, compounds **5a-h** give intense green emission (band around 500 nm) when excited at 370 nm.

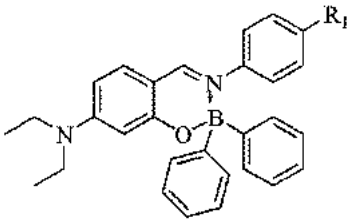

5a R_1=H
5b R_1=F
5c R_1=Cl
5d R_1=I
5e R_1=OCH_3
5f R_1=NEt_2
5g R_1=$COOCH_3$
5h R_1=$COOCH_2CH_3$

Fig. 4.1 Molecular structure of borinates **5a-5h**.

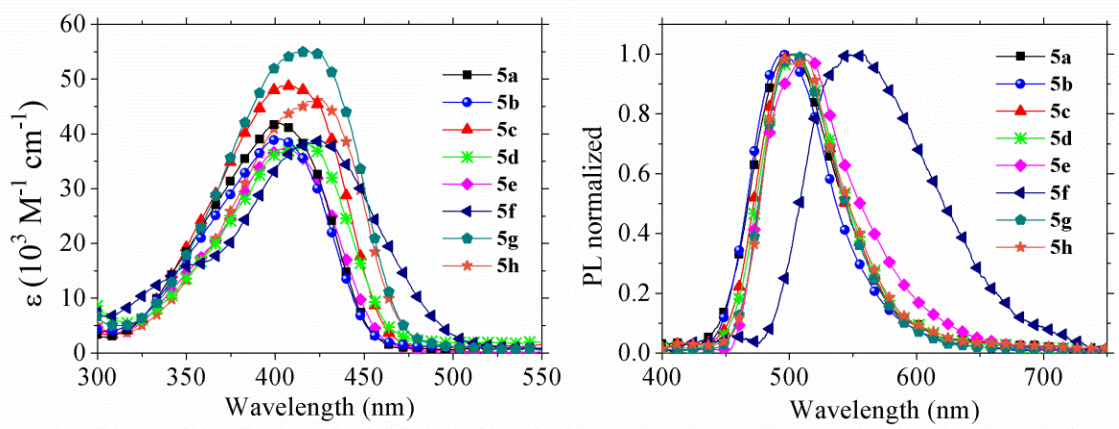

a) b)

Fig. 4.2 Linear absorption (a) and emission spectra (b) for borinates ***5a-5h*** in THF solution.

Quantum yields Φ_F for all borinates were measured in THF solutions, giving values from 0.03 to 0.26 (see Table 4.1), which are in agreement with those values obtained from similar boron compounds (0.01-0.6) reported by other authors,[127] but lower that those reported in the range 0.31-0.65 for boron compounds derivates from benzoxazole.[128]

A possible explanation of the low Φ_F values is the non-planar conformation observed in the π-backbone of **5c** and **5e** in comparison to the π-system of benzoxazole derivatives that have flat conformation. In general, the experimental Φ_F values obtained from **5a-h** showed a dramatic decrement for compounds with D–C=N^+–D architecture, in which there is an increase of electronic density in the π-skeleton.

4.1.2 Two-photon absorption

To obtain information of the efficiency of the TPA process in this series of compounds, the cross section (σ_{TPA}) of borinates **5a-h** were calculated from data of TPEF experiments. This technique is based on a comparison of the two-photon excited fluorescence spectra from the sample (borinate) with a standard (Rhodamine 6G). Figure 4.3 displays the values measured for σ_{TPA} at the wavelength range 740-830 nm. From this figure we observe that at such wavelength range the molecules exhibit only small variations in their σ_{TPA} values. For shorter wavelengths (corresponding to energies higher than the one-photon transitions that define the peaks shown in Figure 4.2a), it is expected that some TPA resonances might occur. In our case, however, the two-photon absorption spectra were not extended to shorter wavelengths due to the limited tunability of our laser system. Nevertheless, the σ_{TPA} values shown in Figure 4.3 allowed comparison of the effect of the molecular structure on the nonlinear optical properties.

The studied borinates can be grouped in two categories, those comprising a D–π–C=N^+–π–D architecture with strong electron donor groups at the end of the molecule, i.e., **5e** (–OCH_3) and **5f** (–NEt_2), and compounds containing a D–π–C=N^+–π–A architecture, **5b** (–F), **5c** (–Cl), **5d** (–I), **5g** (–$COOCH_3$) and **5h** (–$COOCH_2CH_3$). Surprisingly, the architecture D–π– C=N^+–π–D produced the lowest values of σ_{TPA} and the smallest fluorescence quantum yields. Larger values of σ_{TPA} were obtained for the D–π–C=N^+–π–A architecture, and for the particular case of **5b**, **5c**, and **5d** the cross section values are inversely related to the electronegativity. For the same architecture, the highest cross section was found for the ester groups **5g** and **5h** where the acceptor provides stabilization.

5h exhibited the largest fluorescence quantum yield among all set of studied molecules. This system with architecture D–π–C=N^+–π–A has larger two-photon activity (light emission induced by TPA) than ferrocenyl substituted pyrazaboles with architecture D–π–A–π–D.[36]

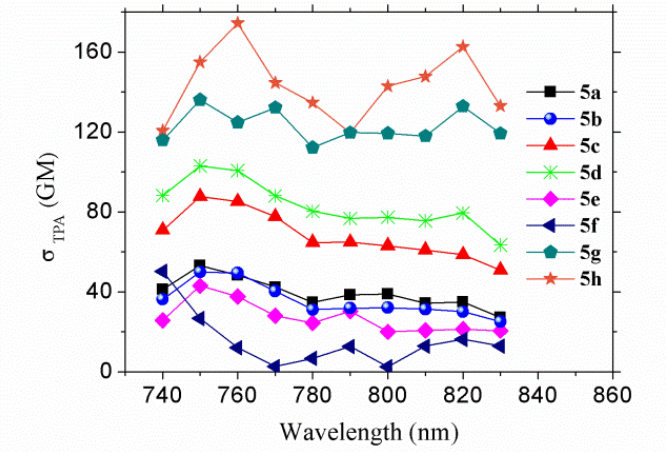

Fig. 4.3 TPA cross section spectra of borinates ***5a-5h*** in THF solution.

Table 4.1. Photophysical properties of borinates ***5a-5h.***

Molecule	λ_{abs} (nm)	$\varepsilon\ 10^3$ ($M^{-1}\ cm^{-1}$)	λ_{em} (nm)	Φ_F [a]	σ_{TPA} (GM)[b]
5a	402	42	502	0.11	53
5b	402	39	494	0.11	49
5c	409	48	500	0.16	85
5d	417	38	503	0.17	100
5e	403	37	513	0.03	37
5f	425	38	547	0.04	12
5g	418	55	503	0.10	124
5h	425	46	504	0.26	174

[a] Using Rhodamine 6G as reference, Φ_F = 0.95 in methanol, λ_{ex}= 370 nm
[b] using a excitation irradiation of 760 nm

All borinates exhibit fluorescence induced by one and two-photon absorption at the wavelengths about 400 and 800 nm, respectively. The highest two-photon absorption cross-section (σ_{TPA} = 174 GM) of the series of studied compounds corresponds to **5h** with a D–π–C=N^+–π–A (D = NEt_2 and A = $COOCH_2CH_3$) architecture. It is low and similar to commercial dyes, so that we decided not to process them into organic nanostructures. However, the results provided important insight on the structure/properties for borinanes, which were included in the scientific article paper "Synthesis and chemical-optical characterization of novel two-photon fluorescent borinates derived from Schiff bases", Cristina C. Jiménez, Norberto Farfán, Margarita Romero-Avila, Mario Rodríguez, **Laura Aparicio-Ixta**, Gabriel Ramos-Ortiz, José Luis Maldonado, Rosa Santillan, Nancy E.

Magaña-Vergara, Ma. Eugenia Ochoa. *Journal of Organometallic Chemistry*, 755, 33-40, 2014.

4.2 Bodipys

We decided to study four BODIPYS (4,4-difluoro-4-bora-3a,4a-diaza- *s* -indacene) with tetraphenylethene (TPE) units introduced at the periphery to a methylated BODIPY core because they are classical chromophores that recently have regained considerable research attention owing to their excellent photophysical properties, including large molar extinction coefficients, intense photoluminescence (PL), narrow absorption and emission bandwidths, high photostability, etc. They comprise an attractive chemical nature that allows facile modifications at the meso-, 2,6- and 3,5-positions of BODIPY ring or fusing other aromatic rings to pyrroles,[129] which offers an abundant possibility to fulfill specific requirements of practical applications. TPE-decorated BODIPY luminogens, illustrated in Figure 4.4, were synthesized by Prof. Zujin Zhao and coworkers (College of Material Chemistry and Chemical Engineering, Hangzhou Normal University, China).

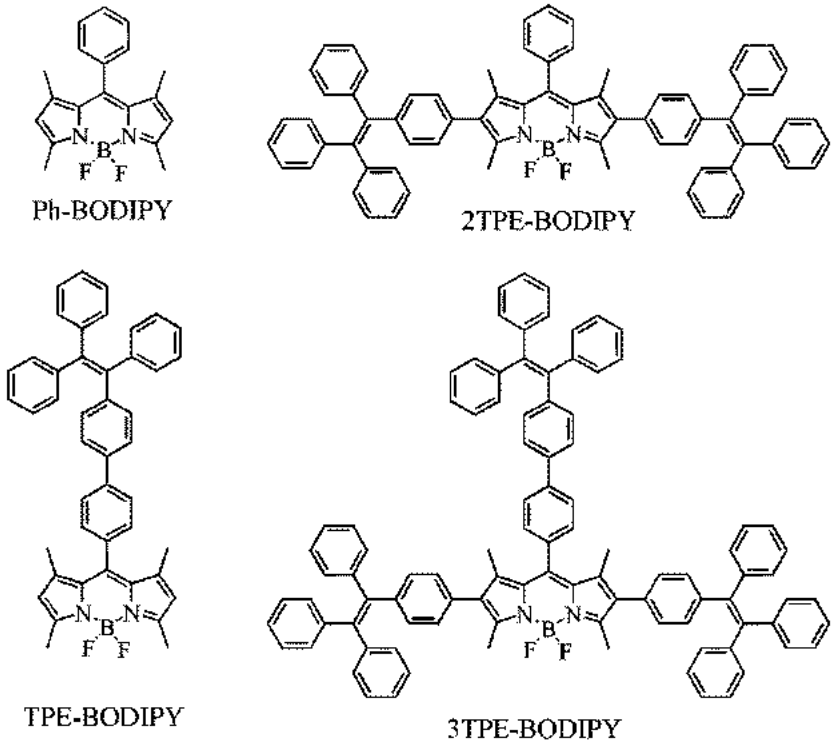

Fig. 4.4 TPE-decorated BODIPY luminogens.

For biophotonic applications, it is necessary that TPA materials be water soluble or dispersible and remain highly fluorescent in aqueous media. Many TPA materials, however, are hydrophobic and their fluorescence quantum yields are considerably reduced in water owing to the aggregation of molecules, which generally leads to fluorescence quenching. As an effective approach to overcoming the notorious aggregation-caused quenching (ACQ) problem in the usage of traditional fluorescent dyes, materials with aggregation-induced emission (AIE) or aggregation enhanced emission (AEE) properties can dramatically boost the fluorescence from luminogen aggregation when their concentrations increase. AIE phenomenon is caused by restricted intramolecular vibrational and rotational motions in the aggregated solid. Although AIE luminogens with various functionalities have been prepared, there are few examples available in the literature that reports the synthesis of luminogenic compounds with both AIE features and TPA absorption.[130]

Consequently a special molecular design for a TPA material is required not only to ensure a large two-photon activity, but more importantly, to offer a new path to the solution of the thorny problem of aggregation-caused quenching. Therefore, the usage of AIE and AEE compounds with strong TPEF could revolutionize fluorescence microscopy. To solve the notorious aggregation-caused quenching problem of many widely used fluorescent dyes, an AIE phenomenon was reported in a series of propeller-shaped molecules such as tetraphenylethene (TPE).[131] TPE and its derivatives are composed of an ethenyl core and multiple rotational phenyl rings. Due to the steric repulsion between the adjacent phenyls, these molecules have to take a nonplanar conformation. As a result, there is only a little intermolecular π–π interaction possessed in their solids.

The attachment of AIE moieties to traditional ACQ dyes can also successfully transform them into AIE compounds with desirable aggregated state emission. A number of TPE-based derivatives have been synthesized. Nevertheless, there is still huge space to modify the structure and to develop TPE-based advanced functional materials. In an attempt to overcome the aggregation-caused quenching limitation of the current TPA fluorophores four BODIPYS with tetraphenylethene units (TPE) were synthesized. The aim was to investigate how conjugation affects their properties such as light emission and TPA absorption, and Prof. Zujin Zhao investigated their potential practical applications in bioimaging.

4.2.1 Linear Optical Properties

The one-photon absorption (OPA) spectra of TPE-decorated BODIPY luminogens in THF solutions are shown in Figure 4.5a. 3TPE-BODIPY and 2TPE-BODIPY that bear two TPE

units at the 2,6-positions of BODIPY ring exhibit almost the same spectral profiles with absorption maxima at 534 nm, associated with the π–π * transition. TPE-BODIPY containing one TPE moiety linked through a phenyl bridge at the *meso*-position of BODIPY core shows absorption maximum at 500 nm, which is close to that of Ph-BODIPY (495 nm).[132] The absorption spectra of 3TPE-BODIPY and 2TPE-BODIPY are bathochromically shifted by 34 nm with respect to TPE-BODIPY, demonstrating that the conjugation length of luminogen is noticeably more extended by covalently attaching π-conjugated substituents at the 2,6-positions of BODIPY ring than at the *meso*-position. Figure 4.5b displays the one-photon excited fluorescence (OPEF) spectra of the luminogens in THF solutions. 3TPE-BODIPY and 2TPE-BODIPY show fluorescence peaks at 584 and 583 nm, respectively, which are much redder than those of TPE-BODIPY (516 nm) and Ph-BODIPY (507 nm).[116] The Stokes shifts of 3TPE-BODIPY and 2TPE-BODIPY are 46 nm, which are much larger than those of TPE-BODIPY (16 nm) and Ph-BODIPY (12 nm), evidently disclosing that incorporation of TPE units at the 2,6-positions of the BODIPY ring is an effective approach to create BODIPY derivatives with large Stokes shifts.

The good conjugation and large Stokes shift enable 3TPEBODIPY to fluoresce efficiently. The fluorescence quantum yield (Φ_F) of 3TPE-BODIPY is 44%, which is higher than those of 2TPE-BODIPY (38%) and TPE-BODIPY (28%), measured in THF solutions by the integrating sphere method. Although many luminogens consisting of TPE units fluoresce faintly in the solution state due to exciton annihilation by intramolecular rotation,[24,133,134] there are also some exceptions.

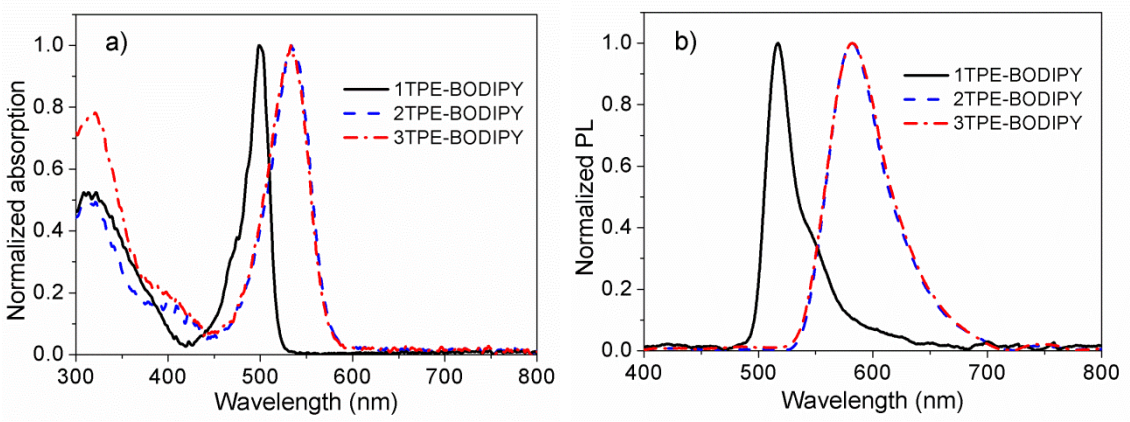

Fig. 4.5 a) Absorption and b) fluorescence spectra of TPE-decorated BODIPY luminogens in dilute THF solutions.

4.2.2 Two-photon absorption

Significantly, these TPE-decorated BODIPY luminogens show good two-photon absorption and two-photon excited fluorescence within the window of biomedical interest, in particular at the wavelength range of 750–830 nm. The cross-sections of TPA (σ_{TPA}) and TPEF (σ_{TPEF}) of these luminogens vary with the molecular structure as well as wavelength of the laser excitation (Figure 4.6). The values become augmented obviously with the increase of TPE units in the luminogens. 3TPE-BODIPY shows the best nonlinear optical property, with the highest σ_{TPA} and σ_{TPEF} values of 264 and 116 GM, respectively, when its THF solution is pumped with laser pulses at wavelength of 810 nm. These values are much higher than those of Ph-BODIPY[135] and other BODIPY dyes in the literatures (4–128 GM).[56] Figure 4.7 compares the spectrum of fluorescence excited by one photon (OPEF) with TPEF spectrum of 3TPE-BODIPY excited at 375 and 800 nm, respectively. The TPEF spectrum resembles the OPEF one except for a tiny bathochromic shift of ≈3 nm, suggesting that the red emissions of both TPEF and OPEF originate from the same decay of singlet excitons. Table 4.2 summarizes the optical properties of bodipys in THF solution.

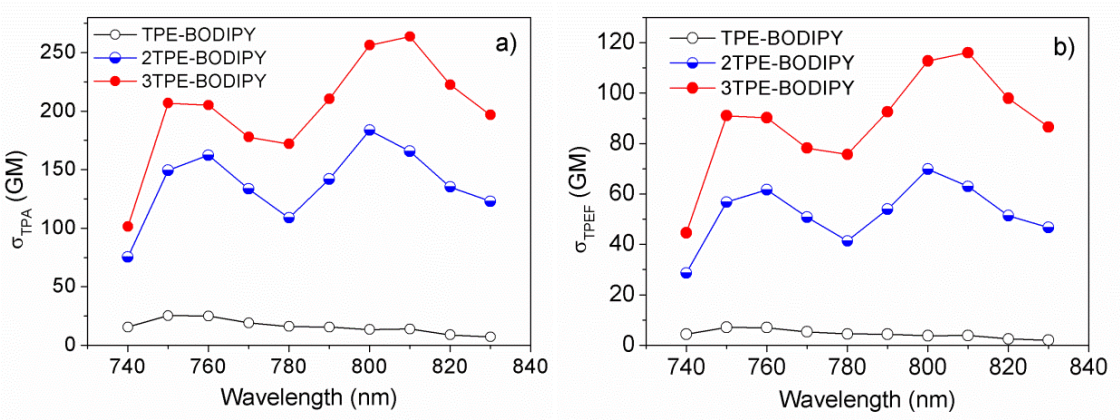

Fig. 4.6 a) TPA and b) TPEF dispersion curves of TPE-decorated BODIPY luminogens dissolved in THF.

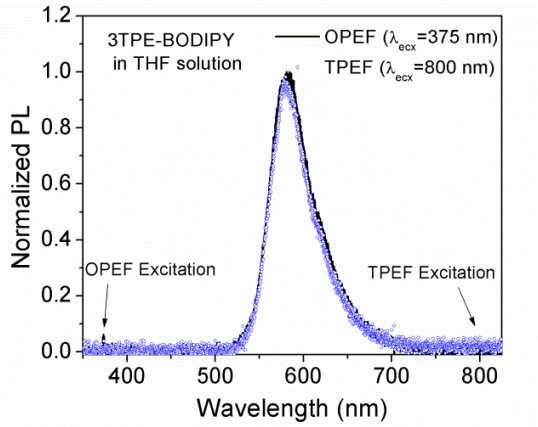

Fig. 4.7 OPEF and TPEF spectra of 3TPE-BODIPY in THF solution.

Table 4.2. Optical properties of BODIPYS.

Molecule	λ_{abs} (nm)	λ_{em} (nm)	Φ_F [a]	$\sigma_{TPA\ (GM)}$ [b]
1TPE-BODIPY	500	516	0.28	14
2TPE-BODIPY	534	583	0.38	165
3TPE-BODIPY	534	584	0.44	264

[a] Using Rhodamine 6G as reference, $\Phi_F = 0.95$ in methanol, λ_{ex}= 370 nm
[b] using a excitation irradiation at 810 nm

In summary, linear and nonlinear optical properties of a series of luminescent materials consisting of TPE peripheries and a BODIPY core were investigated to gain a deeper insight into the structure–property relationship of these BODIPY luminogens. The accumulation of TPE units can not only ameliorate the fluorescence emission in the aggregate state but also benefit the TPA and TPEF properties of the luminogens.

These important results were include in the paper "Red Emissive Biocompatible Nanoparticles from Tetraphenylethene-Decorated BODIPY Luminogens for Two-Photon Excited Fluorescence Cellular Imaging and Mouse Brain Blood Vascular Visualization", Zujin Zhao, Bin Chen, Junlong Geng, Zhengfeng Chang, **Laura Aparicio-Ixta**, Han Nie, Chi Ching Goh , Lai Guan Ng , Anjun Qin , Gabriel Ramos-Ortiz, Bin Liu, and Ben Zhong Tang, *Part. Part. Syst. Charact.* 2014, 31, 481–491.

4.3 Fluorene derivatives

The fluorene-based compounds are of great interest since they show a strong π-electron conjugation, i.e., large electron delocalization and, additionally, high fluorescent efficiency. They have been used for different optical applications, such as organic electroluminescence devices (OLEDs) and organic photovoltaic cells (OPVs).[136] Other optical uses are for two-photon absorption (TPA),[137] and sensors.[138]

Fluorene-based monomer (M1) and its cross conjugated polymer (P1) studied in this dissertation were designed and synthesized by Prof. Mikhail G. Zolotukhin (Instituto de Investigaciones en Materiales, Universidad Nacional Autónoma de México) while BT2 was designed by Mario Rodríguez (Centro de Investigaciones en Óptica, A.C.) and synthesized by Jesús Rodríguez-Romero in the Group of Dra. Rosa Santillán (Departamento de Química, Centro de Investigación y de Estudios Avanzados del IPN, México D.F.). Figure 4.8 a) shows the molecular structures of these three organic compounds and Figure 4.8 b) shows THF solutions of the same compounds excited by UV light.

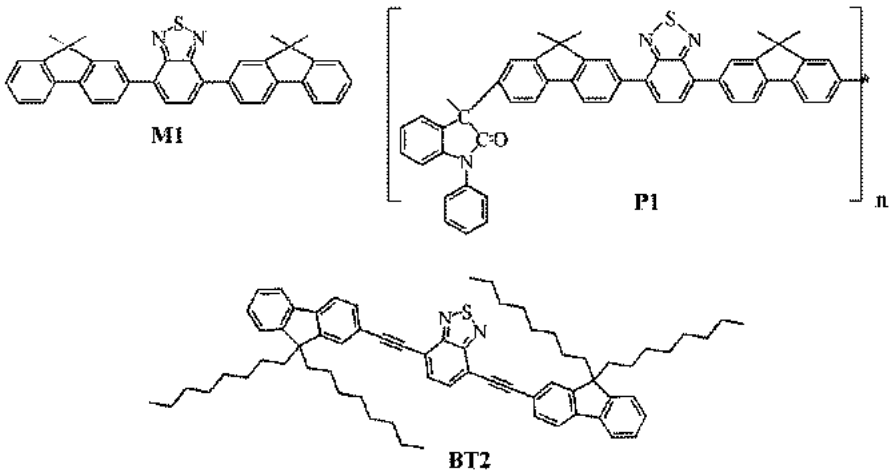

a)

b)

Fig. 4.8 a) Chemical structures of the fluorene-based compound **BT2**, the monomer **M1** and its cross-conjugated polymer **P1**. b) THF solutions of the same compounds excited by UV light.

4.3.1 M1 and P1

This section reports on the fabrication and TPA properties of aqueous suspensions of silica nanoparticles loaded with the fluorene-based cross-conjugated polymer (P1). The results are compared with those obtained from dye-loaded silica nanoparticles, this dye being the monomer (M1) of such a conjugated polymer. Our study also includes the TPA properties of organic solutions of M1(P1) and aqueous suspensions of nanoparticles of M1(P1)

fabricated by reprecipitation method, M1 (M1-NPs) and P1 (P1-NPs). The procedure to fabricate these nanoparticles is described in Appendix B.

On the other hand, doped silica nanoparticles were synthesized based on methods described by Wang et al., Qian et al., and Arriagada et al.[49,139,140] The process consists of the preparation of a microemulsion system based in the nonpolar core of Aerosol-OT/1-butanol micelles in water, following by addition of dyes and silica precursors. The details are shown in Appendix C.

4.3.1.1Transmission electron microscopy of M1(P1)-NPs

Our nanoparticles were analyzed through transmission electron microscopy (TEM). The size and dispersion of nanoparticles were determined by parameters used during the synthesis such as the concentrations of surfactants, organic materials, and silica precursors. In the following our attention is focused on nanoparticles obtained from **P1.** For instance, Figure 4.9a and 4.9b present micrographs of **P1**-NPs from suspensions (4.1×10^{-7} M) processed with two different concentration of CTAB (0.08 and 0.8 mM, respectively). The mean sizes of **P1**-NPs so obtained were 29 nm and 19 nm, respectively. As expected, higher concentration of surfactant reduced the nanoparticles size. Likewise, for the case of **P1**-SNPs different sizes were obtained from suspensions (3.1×10^{-7} M) by varying the amount of aerosol-OT utilized during their synthesis. Figure 4.9c and 4.9d present **P1**-SNPs with mean sizes of 125 nm and 40 nm obtained with two different concentrations of aerosol-OT (50 mM and 98 mM, respectively). From these TEM micrographs it is clearly observed that the reprecitation method produced **P1**-NPs with irregular shapes while silica encapsulation produced **P1**-SNPs with spherical shape. The insets of Figure 4.9 show the nanoparticles size distribution obtained from the analysis of various TEM micrographs using the software ImageJ. We performed additional experiments to obtain NPs size distribution through dynamic light scattering (DLS). In this case, the size of nanoparticles were in relatively good agreement with TEM results, although the mean sizes resulted somewhat larger and with broader size distribution. This was expected because when a liquid medium moves a dispersed particle, often an electric dipole layer adheres to its surface which has influences in the particle motion, for this reason in dynamic light scattering (DLS) the measured particle diameter, which is known as hydrodynamic, most of times is greater than the diameter measured with a transmission electron microscope (TEM). For instance, suspension of **P1**-NPs processed with CTAB at 0.8 mM of concentration resulted in mean sizes of 41 nm, while **P1**-SNPs synthesized with aerosol-OT at concentrations of 50 mM resulted in 154 nm (see Figure 4.9).

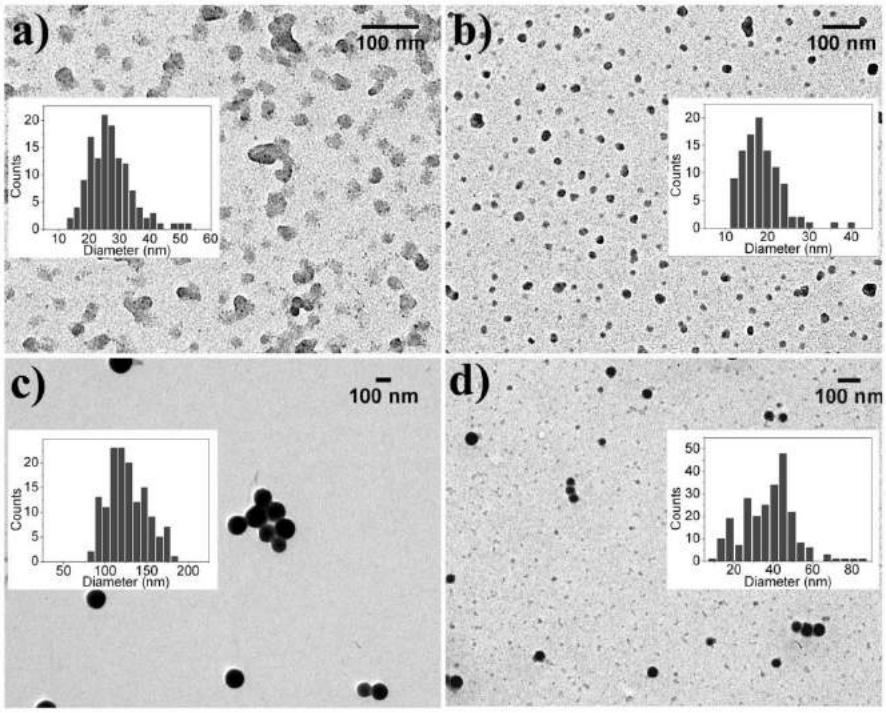

Fig. 4.9 TEM micrographs of **P1**-NPs obtained from suspension processed with two different concentration of CTAB: a) 0.08 mM and b) 0.8 mM. TEM micrographs of **P1**-NPs obtained with two different concentrations of aerosol-OT: c) 5 mM and d) 10 mM. Insets: nanoparticles size distribution from the analysis of various TEM micrographs.

4.3.1.2 Linear Optical Properties

Linear absorption

Figure 4.10a shows the UV-vis absorption spectra from THF solution of M1 (M1-THF) and from aqueous suspensions of nanoparticles of M1 (M1-NPs) and M1-doped silica nanoparticles (M1-SNPs). Two absorption bands are present in these spectra. Our calculations performed within the framework of DFT for a model of M1-THF showed that the long wavelength absorption maxima ($S_0 \rightarrow S_1$) at 415 nm nm is due to a significant intramolecular charge transfer (ICT) process, where the charge is transferred from π orbitals of fluorene fragments to π* orbitals of benzothiadiazole (charge density distribution for the HOMO and LUMO orbitals are displayed in inset of Figure 4.10a and in Fig. 4.11). In the case of M1-NPs it is observed that the π - π* transition (404 nm) is blue-shifted compared with M1-THF. Commonly, blue shifting is assigned to molecular bending or to a decrease in the Stokes shift that results from restraint of vibronic relaxation, as it has been

observed by other authors who reported on organic nanoparticles in mixtures of solvent and water.[101] In our case, however, the use of surfactants to stabilize nanoparticles in water plays a role in the localization of the absorption peak. For instance, nanoparticles stabilized with CTAB and Triton X-100 produced a blue shifting of 9 nm as compared with THF solution, but red shifting of 8 nm was detected when albumin was employed as surfactant (result not included in Figure 4.10). In regard to M1-SNPs the peak of maximum absorption did not display significant shifting with respect to M1-THF. The presence of silica nanoparticles, however, is clearly evident in absorption spectra since it produces light scattering, i.e., the real absorption bands are superimposed into a baseline of scattering. The so obtained absorption spectra from M1-SNPs were the same independently of the silane-based precursors (APTES or THPMP) utilized during their synthesis. To correct the absorption spectra and remove the scattering artifact in Figure 4.10, we used the empirical approach followed by Lebret *et al.*[141] Thus, the region of null absorption of M1, from 550 to 700 nm, was used as model of the baseline that is extrapolated to shorter wavelengths through a polynomial regression. A good approximation of the real absorption spectrum was then obtained by subtracting the scattering baseline from the measured spectrum.

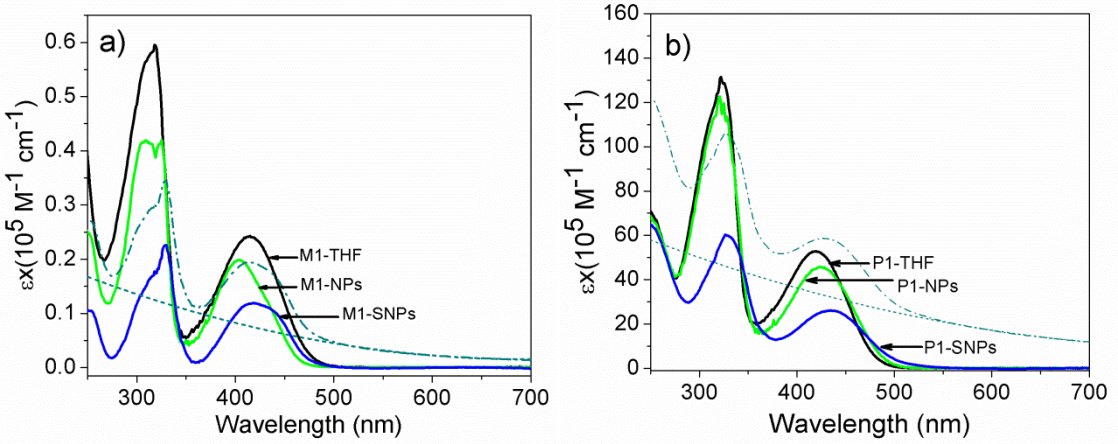

Fig. 4.10 Linear absorption spectra from a) THF solution of **M1**, aqueous suspensions of **M1**-NPs and aqueous suspensions **M1**-SNPs; b) THF solution of **P1,** aqueous suspensions of **P1**-NPs and aqueous suspensions **P1**-SNPs. In the case of **M1**(**P1**)-NPs the suspensions are stabilized with CTAB. The dash-dotted line represents the **M1**(**P1)**-SNPs absorption spectrum before scattering subtraction and the dotted line the scattering baseline.

Figure 4.10b displays the UV-vis absorption spectrum from a THF solution of **P1** (**P1**-THF). Similarly to the case of **M1**, DFT calculations demonstrated that absorption at long wavelengths in **P1**-THF is also dominated by ICT character. In this case the optical properties of the polymer were simulated by using an oligomer as a model (see Figure 4.12). We can observe that four molecular orbitals are involved in $S_0 \rightarrow S_1$ transition

(HOMO-1, HOMO, LUMO, LUMO+1). Such π - π* transition appears at 419 nm in **P1**-THF but it is red-shifted to 423 and 435 nm for **P1**-NPs and **P1**-SNPs (independently of the use of APTES or THPMP as silane-based precursor), respectively. Comparable red-shifting has been observed previously in nanoparticles synthesized from fluorene polymers[142] although other authors have reported a blue-shifting effect in similar compounds.[113] The discrepancy between these observations is ascribed to the specific structure of the utilized hydrophobic polymer and the conformational changes introduced in the structure when it is brought in an aqueous environment.

Charge transfer (CT) character of M1 and P1

Figure 4.11 shows the model used for **M1** in DFT calculations and the most important molecular orbitals involved in the electronic transitions. The long wavelength absorption maxima ($S_0 \rightarrow S_1$) resulted to be λ_{max}=397 nm (415 nm experimentally). This transitions shows a significant charge transfer (CT) character, where the charge is transferred from π orbitals of fluorene fragment to π* orbitals of benzothiadiazole moiety. Broad and intense absorption maxima for **M1** in the range 280-340 nm can be attributed to $S_0 \rightarrow S_2$ and $S_0 \rightarrow S_3$ transitions. In the case of $S_0 \rightarrow S_3$, the transition has high oscillator strength (1.22) and involves π orbitals extended over the entire molecule (HOMO→ LUMO+1). On the other hand, the weaker $S_0 \rightarrow S_2$ transition (HOMO-1 →LUMO) has CT character similar to $S_0 \rightarrow S$.

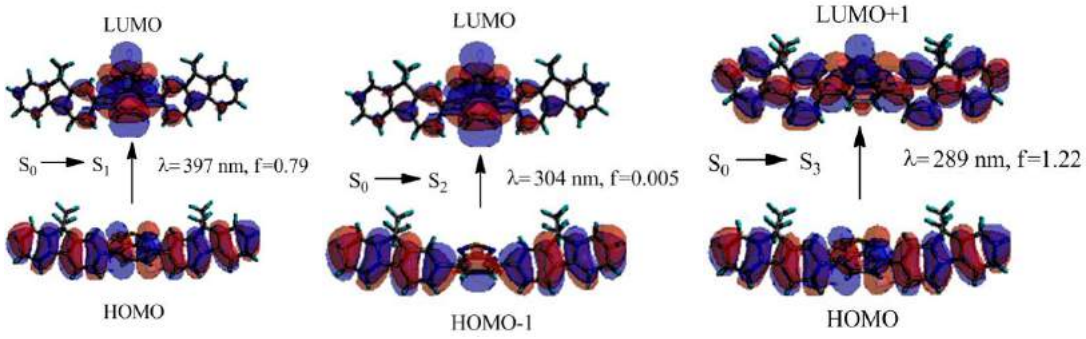

Fig. 4.11 The most important excitations contributing to the transitions in **M1**.

Figure 4.12 shows the model used for **P1** in DFT calculations. In this case **P1** was modelled using an oligomer as depicted in the figure. The long wavelength absorption maxima ($S_0 \rightarrow S_1$) involves mostly four molecular orbitals (HOMO-1, HOMO, LUMO, LUMO+1, LUMO+2 and LUMO+3) as it has a charge transfer character similar to **M1**. It is noteworthy that the $S_0 \rightarrow S_2$ transition also has CT character and lies very close to $S_0 \rightarrow S_1$ (395 mn), contributing to the long wave absorption of **P1**, but with very weak oscillator

strength. For short wavelength absorption, the most intense transition is S_0-S_5 (λ_{max}=291, oscillator strength 2.40), corresponding to a combination of HOMO-1→LUMO+3 and HOMO→LUMO+2, with no CT character.

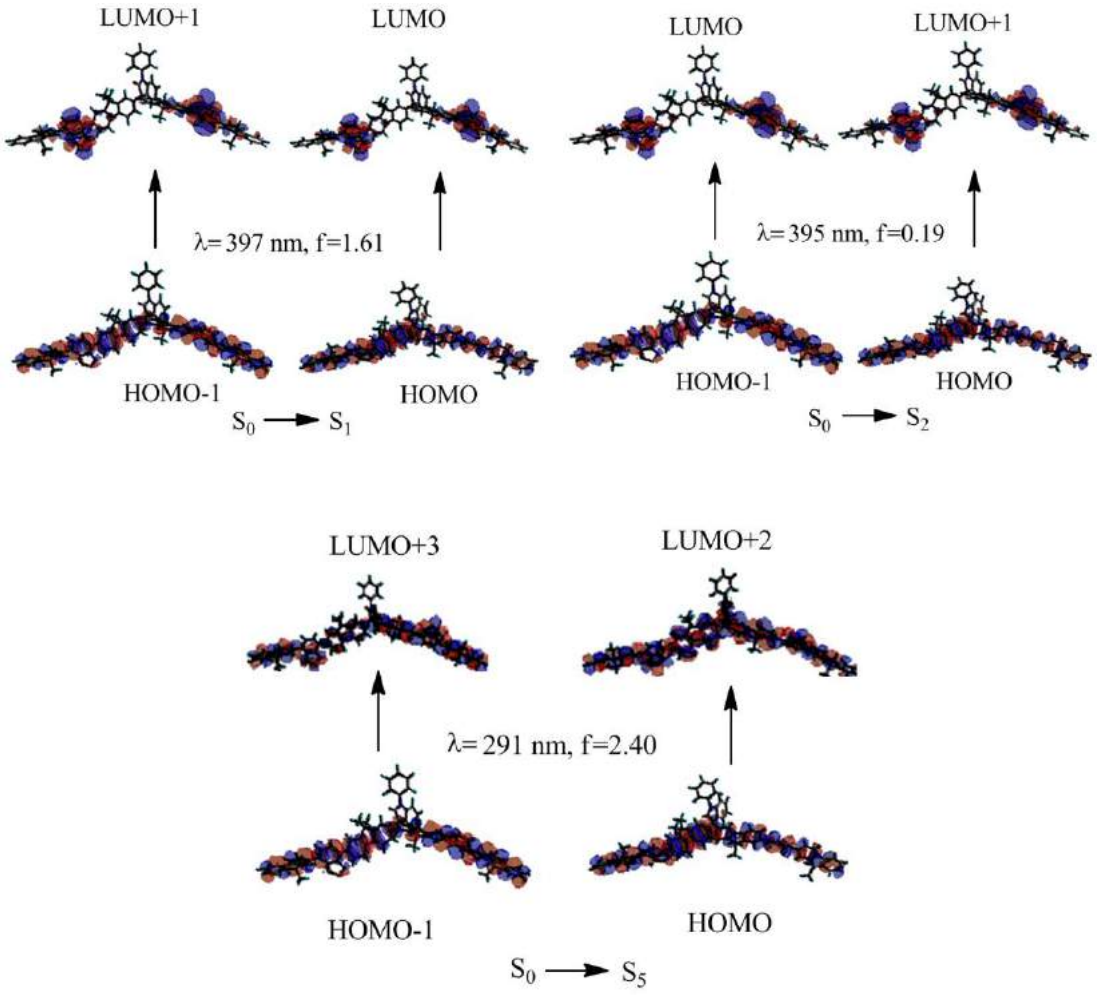

Fig. 4.12 The most important excitations contributing to the transitions of an oligomer structure used as model for **P1**.

Photoluminescence properties

One-photon excited fluorescence spectra from monomer **M1** and polymer **P1** in solutions and aqueous suspensions are displayed in Figure 4.13. Emission spectra undergo wavelength shifting for the case of nanoparticles. In particular, the monomer **M1** exhibited notorious changes such that the emission peaks in **M1**-NPs and **M1**-SNPs were blue-shifted

approximately 5 nm and 16 nm, respectively, compared with the peak of **M1**-THF. In contrast, fluorescence peaks in **P1**-NPs and **P1**-SNPs exhibited red-shifting of 4 nm and 9 nm, respectively. Thus, the chances in the energies corresponding to the π-π^* transition in the absorption spectra shown in Figure 4.10 are consistent with the wavelengths shifts observed in photoluminescence spectra shown in Figure 4.13.

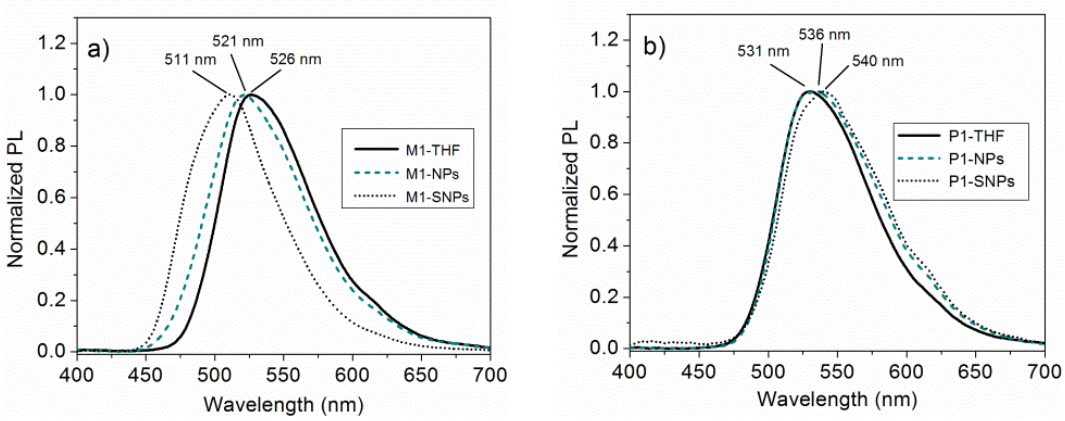

Fig. 4.13 Normalized photoluminescence (PL) spectra for a) monomer **M1** and b) polymer **P1** in solutions and aqueous suspensions. Excitation: UV lamp.

Fluorene based molecules and polymers are recognized for exhibiting high quantum yields (Φ_F) of fluorescence. Our measurements through the integrating sphere method demonstrated that both **M1** and **P1** in dilute THF solutions have values of Φ_F~1, in agreement with the values for similar fluorene compounds reported by other authors.[49,143,144] The integrating sphere method was also applied to aqueous suspensions under study in order to know to what extent Φ_F is affected due to the introduction of channels of non-radiative decays for excited states when **M1**(**P1**) are agglomerated or loaded into silica nanoparticles. Table 4.2 summarizes the results. For these measurements concentrations of aqueous suspensions were kept below 1×10^{-5} mol/L. Notoriously, both **M1**-NPs and **P1**-NPs did not exhibit strong effects of photoluminescence quenching and the quantum yields remained near to one, although for the case of **M1**-SNPs and **P1**-SNPs there was a reduction of about 30% and 25%, respectively. Despite the photoluminescence quenching exhibited by **M1**- and **P1**-loaded silica nanoparticles, the obtained values for Φ_F are comparable with those exhibited by some representative fluorescent nanoparticles reported recently, i.e., organically modified silica nanoparticles entrapping fluorene dyes (Φ_F =0.49)[122] and polymeric nanocarriers encapsulating aggregation-induced emission (AIE) dyes (Φ_F =0.62).[145] For these examples as well as for our nanoparticles, Φ_F resulted

considerably much larger than most of the quantum yields reported in seminal works on nanoparticles of conjugated polymers.[85,113]

4.3.1.3 Two-photon absorption

M1 and **P1** in THF solutions and aqueous suspensions of **M1**-NPs, **M1**-SNPs, **P1**-NPs and **P1**-SNPs emit intense upconverted fluorescence under infrared excitation within the tunability of Ti:Sapphire laser (740–820 nm). We verified the nature of the fluorescence induced by femtosecond pulses at 800 nm by measuring its intensity as a function of the input laser power; a quadratic dependence confirmed that the nature of the upconverted fluorescence was indeed induced by two-photon absorption (Figure 4.14).

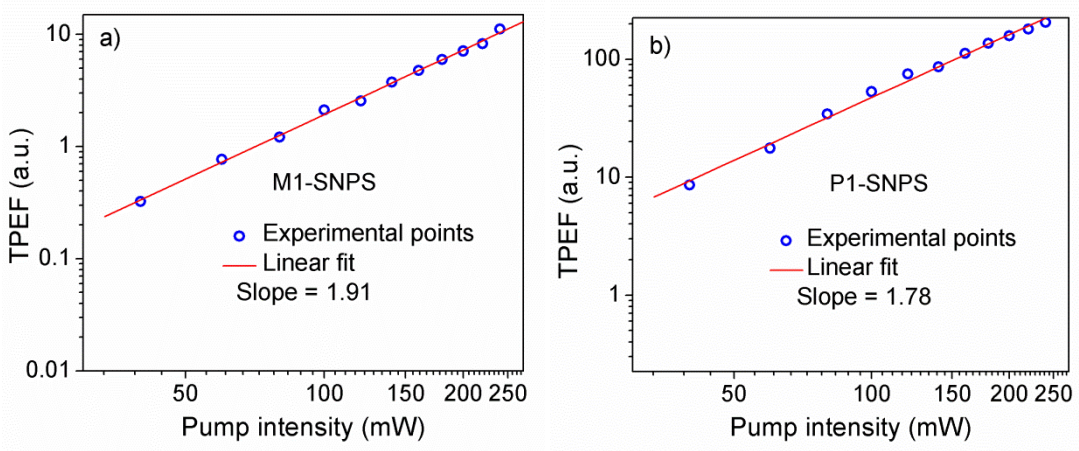

Fig. 4.14 Log-log plot for the dependence of TPEF on pump intensity taking **M1**-SNPS and **P1**-SNPs as an example.

For all samples, the TPEF spectra were the same compared with the OPEF spectra shown in Figure 4.13, indicating that in both cases the light emission originated from the same lowest lying transition in the singlet manifold (see TPEF spectra in Figure 4.15). Figure 4.16 shows the two photon-absorption cross sections (σ_{TPA}) as a function of the excitation wavelength for all samples. We point out that the measured values of σ_{TPA} resulted practically the same when Rhodamine 6G or Rhodamine B where employed as standards in our TPEF experiments, this in spite that their σ_{TPA} values and quantum yields differ appreciably.[6] This confirmed that our experimental setup was well calibrated. For all samples the nonlinear absorption increases at shorter wavelengths (within the range of tunability of the excitation source). The maximum σ_{TPA} was obtained at 740 nm for **P1**-

THF with a value of approximately 9.8×10^3 GM. This is a 117-fold increment with respect to the maximum nonlinearity measured in **M1**-THF. We see that such increment is in correspondence with the number of repeating units in **P1**, and in consequence the large nonlinearity of **P1** is due to an additive effect of the nonlinearities from individual units, i.e., the σ_{TPA} values per repeating unit are similar to that exhibited by **M1**. As it was explained previously, **M1** and **P1** exhibit an ICT character upon excitation, such that charge is transferred from fluorene fragments located at the edges of each monomer/polymer section to the central benzothiadiazole moety (see Figure 4.8). This means that the nonlinear response of **M1** and **P1** is of quadrupolar origin.

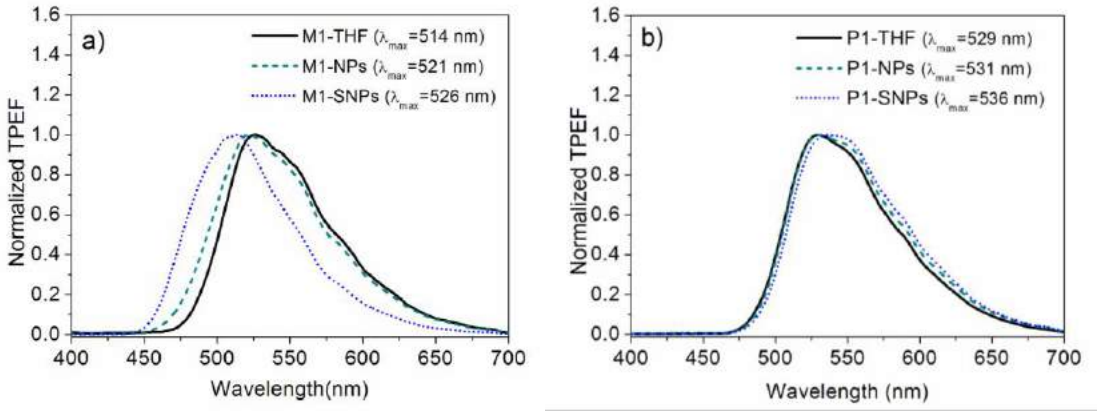

Fig. 4.15 Normalized TPEF spectra for a) monomer **M1** and b) polymer **P1** in solutions and aqueous suspensions. Excitation: femtosecond pulses at 750 nm.

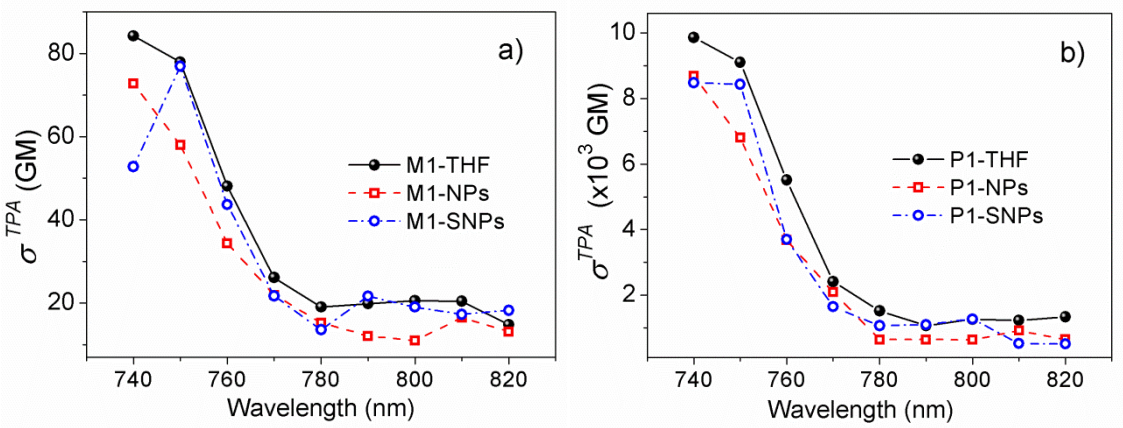

Fig. 4.16 Two-photon absorption spectra of a) **M1** and b) **P1** in solutions and aqueous suspensions of nanoparticles and loaded silica nanoparticles.

Notice from Figure 4.16 that nonlinearities from **M1** and **P1** measured in THF solutions are not substantially affected when such materials agglomerate to form nanoparticles or they are encapsulated into silica nanoparticles. It should be mentioned that the optical properties of aqueous suspensions of bare nanoparticles synthesized through the reprecipitation method without the use of surfactants were also studied and gave similar results than those in **M1**-NPs and **P1**-NPs prepared with the use of surfactants such as CTAB and Triton X-100, but they lacked a desirable stability for long periods and in general generated suspensions with lower nanoparticle concentrations. Similarly, in the case of **M1**-SNPs and **P1**-SNPs the measured σ_{TPA} values were independent on the silane-based precursors (APTES or THPMP) and the amount of surfactants utilized during their synthesis. There are in the literature many examples of silica nanoparticles loaded with organic dyes[146-149] and recently the attention has focused in nanoparticles loaded with dyes exhibiting enhanced TPA.[66,106a),113,139,150] However, to the best of our knowledge, **P1**-SNPs is the first example of polymer-loaded silica nanoparticles intended for two-photon activity. The use of a polymer to be loaded into silica nanoparticles represents an advantage in terms of low fluorescence quenching and high nonlinearities, as in the case of **P1** whose two-photon activity is between two and three orders of magnitude higher than in common dyes and other representative materials.[151,152] It should be emphasized that such high nonlinearities in the cross conjugated polymer P1 are based on the additive effect of repeating units, as it is observed for many polymers, but the same approach of encapsulation into silica nanoparticles can be used for cross-conjugated polymers similar to P1 for which cooperative enhancement of σ_{TPA} values have been achieved.[153]

Further, our approach can also be extended to oligomers[154] and other polymers,[155] hyperbranched polymers[156] and dendrimers[157] for which large nonlinearities are due to cooperative enhancement rather than the additive effect of repeating units. Our results demonstrate that even when the polymer chains are constrained into a small volume in P1-NPS and P1-SNPs, there is no significant reduction of the optical nonlinearities due to possible bending of the polymer backbone or other polymer interactions or conformations. This is also supported by the data displayed in Figure 4.10 which did not show any sign of reduction for the π-conjugation, i.e., there is no blue shifting for the absorption peaks compared with those exhibited by the polymer in solution. Table 4.3 summarizes the nonlinear optical properties of our nanoparticles. In the following chapter we demonstrate the utility of our nanoparticles for the imaging of cells through two-photon microscopy.

Table 4.3 Wavelengths of maximum absorbance and fluorescence, quantum yield and maxima TPA cross sections.

Sample	Absorbance λ_{max} (nm)	Fluorescence λ_{max} (nm)	Φ_F	σ^{TPA}(max) (GM)
M1-THF	415	526	~ 1	84
M1-NPs	404	521	~ 1	72
M1-SNPs	415	511	0.7	76
P1-THF	419	531	~ 1	9860
P1-NPs	423	536	0.95	8481
P1-SNPs	435	540	0.75	8686

Moreover, in order to know the weight percentage of M1 and P1 relative to silica nanoparticle doped with them and functionalized with amino groups, a differential thermal analysis and thermogravimetric analysis was performed. Two suspensions of M1-SNPs and P1-SNPs (~20 mL) were prepared to carry out these analyses; subsequently the fluorescent silica nanoparticles were purified by centrifugation and dialysis procedure. Immediately they were precipitated by centrifugation and placed in the oven to dry. Thermogram experiments were run on a thermo-analyzer model SDT Q600 Simultaneous TGA/DSC, TA Instruments brand under dynamic atmosphere of ultra high purity air (100 mL/min), heating rate of 10 °C/min using reference standard grade alumina and platinum sample holder. The analysis of the thermogravimetric experiments showed that polymer P1 has a glass transition temperature around 205 °C. The sample P1-SNPs lost 23.5 % of initial weight between 229 and 310°C. This weight loss corresponds to the organic fluorophore contained in the sample additionally of the vinyl and aminopropyl groups. Similar loss weight had M1-SNPs (25.8%) between 231 and 319 °C. Both Thermogram experiments were run from 21 °C to 900°C and the residue color of the samples (M1-SNPs and P1-SNPs) was white. In Figure 4.17, table 4.4 and table 4.5 are shown the results obtained.

Table 4.4 Results of thermogravimetric analysis of **M1-SNPs.**

Temperature range ^{0}C	Thermic process	% Loss
21 – 136	No reaction	0.6
136 – 231	No reaction	0.7
231 – 319	Exothermic	25.8
319 – 518	Exothermic	21.8
518 – 735	Exothermic	10.4
735 – 900	No reaction	0.01

Table 4.5 Results of thermogravimetric analysis of **P1-SNPs.**

Temperature range ^{0}C	Thermic process	% Loss
24 – 161	No reaction	1.0
161 – 229	No reaction	1.4
229 – 310	Exothermic	23.5
310 – 474	Exothermic	19.7
474 – 521	Exothermic	5.0
521 – 602	Exothermic	11.4
602 - 900	No reaction	1.6

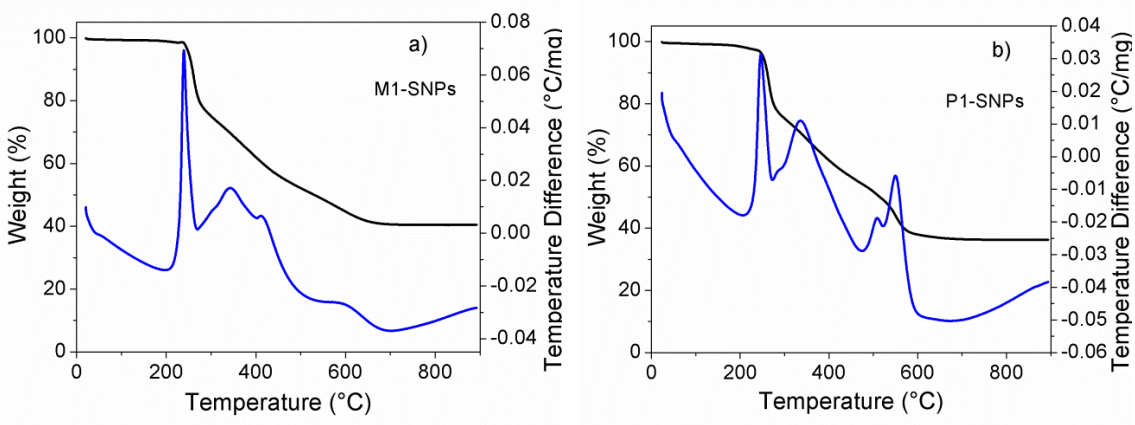

Fig. 4.17 Differential thermal analysis and thermogravimetric analysis of a) M1-SNPs and b) P1-SNPs to determine the percent of fluorophore encapsulated in the silica.

4.3.1.4 Photostability

Organic fluorophores usually suffer of irreversible photobleaching upon intense light irradiation due to photochemical reactions. Photobleaching is a drawback of organic fluorophores used in fluorescence microscopy. To evaluate how the formation of nanoparticles prevents this effect we compared the photostability of aqueous suspension of nanoparticles with the photostability of molecular solutions of M1 and P1. To carry out this study, quartz cells of 0.1×1×4 cm^3 were filled with M1(P1)-THF, M1(P1)-NPS and M1(P1)-SNPs and exposed to the illumination from a 150 watts Xenon lamp. The peak of absorption for each sample corresponding to the π-π^* transition was then monitored as a function of time. Figure 4.18 illustrates the relative photobleaching of the samples. In this figure both M1-THF and P1-THF exhibit low photostability. i.e., their absorbance decreased to approximately 50% of the initial value during the period of time chosen for light irradiation. Meanwhile, the decrease of absorption was less than 10% for all of aqueous suspensions of nanoparticles, with the exception of P1-SNPs in which the photobleaching reached a maximum value of 13 %. This demonstrates that the formation of

nanoparticles prevents the photobleaching effect. We assign this effect to the isolation of the fluorescent materials from the medium. Photobleaching is often caused by molecular oxygen dissolved in the liquid medium that generates photo-oxidation reaction in dyes. When M1 (or P1) are encapsulated within the silica matrix, the reaction with oxygen is significantly hindered. Similarly, the molecular aggregation of M1 and P1 and the subsequent covering with surfactant micelles can effectively exclude oxygen outside M1-NPs and P1-NPs. Such reduction in photobleaching effect results very useful for long time bio-imaging.

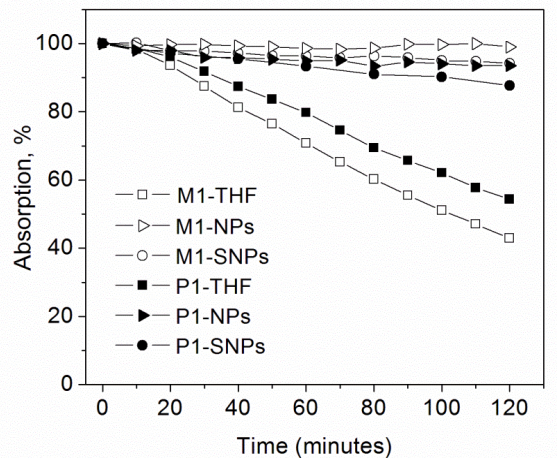

Fig. 4.18 Photostability of **M1** and **P1** in THF solutions and aqueous suspensions of nanoparticles. The samples were exposed to illumination from a Xenon lamp and the absorption at the peak of the π-π^* transition was measured as a function of exposure time.

4.3.2 BT2

Electronic π-systems containing fluorene rings represent an attractive class of aromatic compounds to build different molecular structures, including those with a D-A-D arrangement.[158] Fluorene has been largely used as donor in D-A materials due to its interesting properties which are a consequence of a large HOMO-LUMO energy gap.[159,160] Moreover, fluorene based systems possess unique photophysical properties such as high fluorescent quantum yield, large optical nonlinearities, large photostability, and excellent hole-transporting properties.[161-164]

In this section we study a novel fluorescent molecule with D-A-D architecture based on fluorene moieties linked to the acceptor benzothiadiazole rings called BT2 (4,7-bis((9,9-dioctyl-2-fluorenyl)ethynyl)-2,1,3-Benzothiadiazole, see Figure 4.8). In the design we chose the fluorene ring as donor group since it exhibits excellent photon harvesting and

good charge transfer properties toward the acceptor core. The aims of this work were divided in two parts. First, the study the effect of the solvent-solute interaction on the Intramolecular Charge Transfer character of BT2 and consequently on its luminescent and non-linear optical properties and, second, to study the linear and non-linear optical properties of the same chromophore in different nanostructures and their application as contrast agent in fluorescence microscopy.

4.3.2.1 Linear Optical Properties

Linear absorption

UV-Vis absorption spectra of BT2 were obtained in different solvents such as hexane, toluene, dioxane, tetrahydrofuran, acetone, acetonitrile and methanol to evaluate the influence of the polarity of the medium over their photophysical properties. The linear absorption spectra of the compound are shown in Figure 4.19 and the main characteristics are summarized in Table 4.6. A "camel back" spectrum shape is observed with two strong absorption bands around 319–321 ($\pi \rightarrow \pi^*$) and 431–441 nm. According to previous reports,[165,166] the intense bands observed in the range 431–449 nm should correspond to an ICT transition that occurs between the fluorene edge units and benzothiadiazole central cores.

Table 4.6 shows that the position of the $\pi \rightarrow \pi^*$ electronic transitions in different solvents are practically independent of solvent polarity. As for the ICT bands, it is known that they usually show bathochromic shifts when the solvent polarity is increased; however, only slight shifts were recorded with a non–monotonic behavior. In any case, it is known that the absorption spectra are less sensitive to polarity changes in comparison with the emission spectra.[38,158]

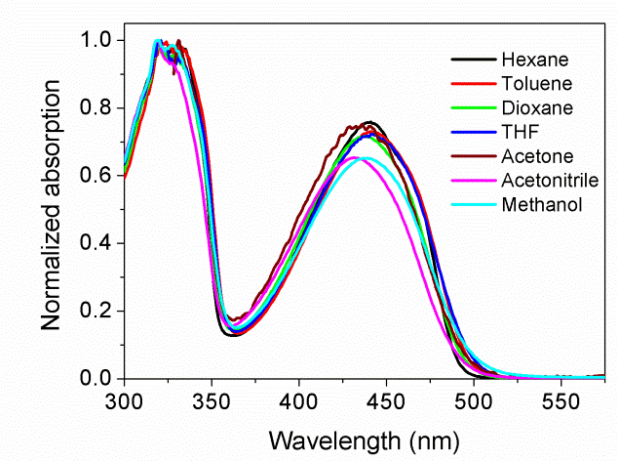

Fig. 4.19 UV-Vis normalized absorption spectra of BT2 in different solvents.

Table 4.6 One-photon absorption data for BT2 compound obtained in different solvents.

		BT2	
Solvent	**P. I.**[a]	$\lambda_{\pi\rightarrow\pi^*}$[b] (ε)[c]	λ_{ICT}[b] (ε)[c]
Hexane	0.009	320(43450)	441(33000)
Toluene	0.099	320(47600)	441(34750)
Dioxane	0.164	320(43550)	438(31200)
THF	0.207	321(51950)	441(37500)
Acetone	0.355	320(87200)	435(63400)
Acetonitrile	0.460	319(36560)	431(23900)
Methanol	0.762	320(25300)	439(16700)

[a] Polarity Index see ref [167]
[b] Value expressed in nanometers
[c] Value expressed in $M^{-1}cm^{-1}$

Photoluminescence properties

The photoluminescence (PL) spectra were also obtained in different solvents (see Figure 4.20). The corresponding wavelengths of maximum emission, intensity of emission and Stokes shifts are summarized in Table 4.7, as well as the quantum yield values. No significant blue PL generated by fluorene moieties was observed. The quenching of the emission of the fluorene moiety is compatible either with a charge transfer process from the fluorenes to the acceptor core center,[165,168] or with an energy transfer process, although the latter is rather related to bimolecular systems.[169] It is noteworthy that the PL spectra from BT2 is strongly dependent on the solvent and show a monotonic bathochromic shift through the solvent polarity, going from greenish emission in hexane solution to reddish in methanol (see Table 4.7 and Figure 4.20).

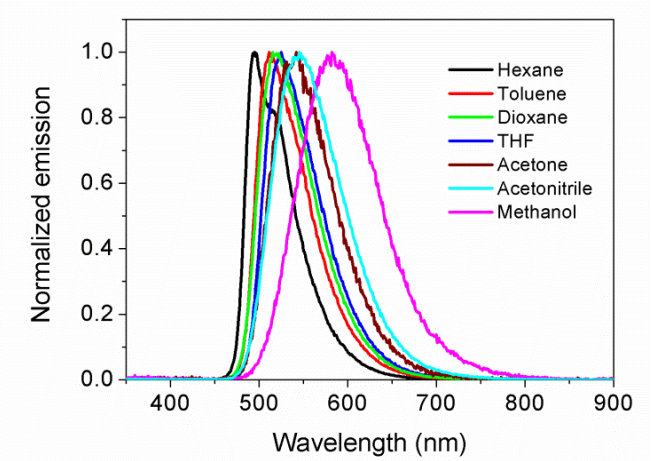

Fig. 4.20 Emission spectra of BT2 in different solvents.

Table 4.7 Emission data for derivatives studied in different solvents.

Solvent	BT2[a]		
	λ_{em}[b] (I. E.)[c]	Φ_F[d]	Stokes Shift[e]
Hexane	495(670)	0.85	11048
Toluene	511(530)	0.76	11681
Dioxane	515(530)	--	11833
THF	525(540)	0.87	12105
Acetone	541(720)	1	12766
Acetonitrile	545(440)	0.9	12999
Methanol	582(120)	0.3	14068

a Concentration 5.2×10^{-5} M. λ_{ex}=320 nm. The slit aperture was of 2.5 for excitation and emission.
b Value expressed in nm.
c Intensity emission expressed in arbitrary units.
d Rhodamine 6G methanol solution (Φ_F = 0.95) was utilized as reference.
e Value expressed in cm^{-1}.

Firstly, to verify the ICT character of this molecule we obtained its excitation spectrum. Fig. 4.21a presents the PL intensity detected at 510 nm for BT2 dissolved in toluene. As expected, the largest green emission was recorded with the excitation from 320 to 340 nm, corroborating that the PL properties of compound BT2 are due to the ICT. In general, the wavelength of maximum emission for this derivative shows a monotonic shift effect when the solvent polarity is increased. This bathochromic shift was accompanied with changes in the fluorescence quantum yield (see Table 4.7). Results show a significant reduction for

this photophysical property going from non polar aprotic to polar protic solvents. Acetone, acetonitrile and THF solutions gave quantum yields higher than 0.85, however, in methanol, there was a drastic PL quenching (Φ_F = 0.3) which was assigned to hydrogen bonding interactions between the solvent and benzothidiazole core.[170-172] The quenching was also observable in mixtures of solvents. For instance, Fig. 4.21b displays the PL spectra of BT2 (at concentration of 6×10^{-5} M) in mixtures of THF–methanol. The data shows that as the ratio of methanol present in the solution is increased, the emission band undergoes a bathochromic shift. A reduction of the PL intensity is also clearly observed.

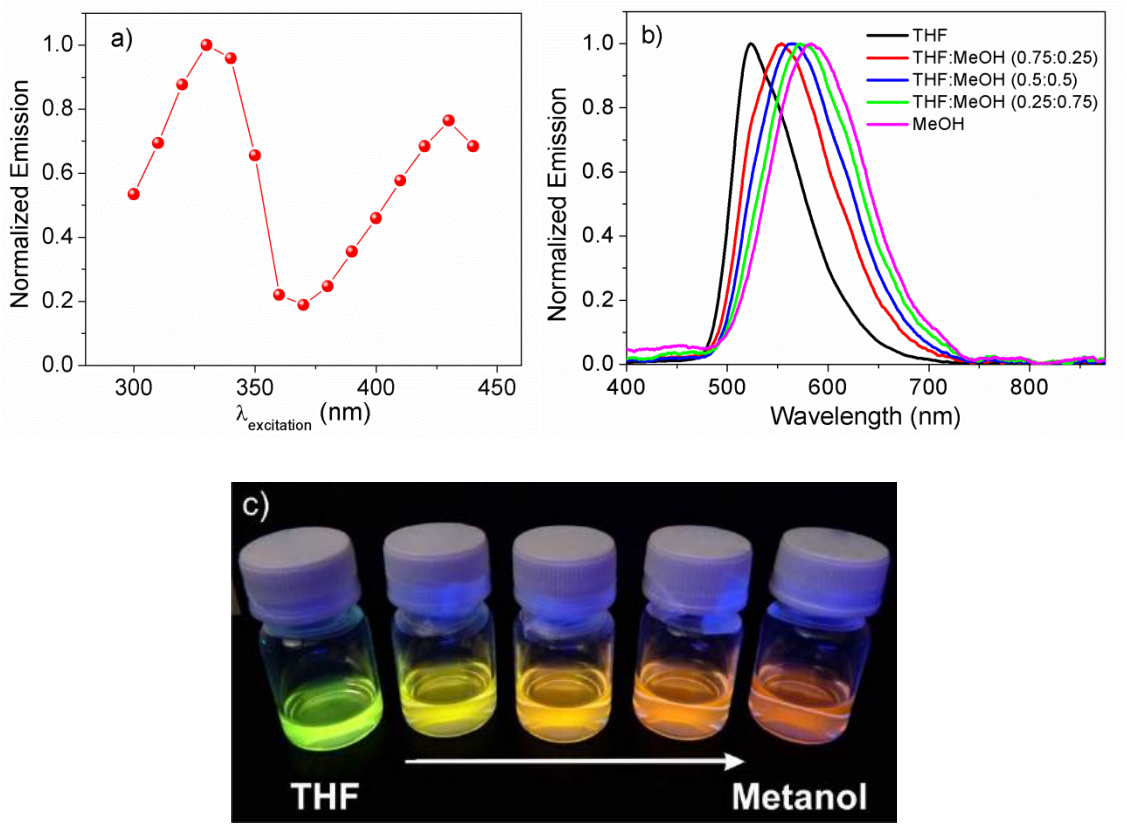

Fig. 4.21 a) Excitation spectrum from BT2 in toluene solution. The PL is detected at 510 nm b) PL spectra of BT2 in mixtures of THF-methanol. The concentration of BT2 in these mixtures was kept constant (6×10^{-5} M), c) PL exhibited by the mixtures.

4.3.2.2 Two-photon absorption in different solvents

TPA properties were also evaluated, taking advantage of the PL exhibited by solutions of the fluorene derivative BT2. The TPA cross-sections (σ_{TPA}) for BT2 compound using the TPEF technique with femtosecond laser pulses, described in Chapter 2, were obtained. Table 4.7 summarizes a comparison between the σ_{TPA} values measured at 750 nm using

different solvents. TPA effect in BT2 is comparable with recent reports on D-A-D structures. For instance, Cheng et al.[173] observed values of σ_{TPA} ~1600 GM when they used diphenylamine and benzothiadiazole moieties as D and A, respectively, and fluorene units as π-bridges. Similarly, Wang et al. measured σ_{TPA} values up to 2103 GM (with Φ_F ~0.36) in THF solutions of a D-A-D compound containing a benzothiadiazole core and fluorene units as a π-bridges;[174] note that in this case the two-photon activity (the product of $\Phi_F \times \sigma_{TPA}$) is similar to the activity of BT2. The enhanced TPA properties observed in BT2 can also be visualized by comparison with other D-A-D systems that employed benzothiadiazole as acceptor group but lack the presence of fluorene units in their structure, i.e., in the representative works performed by Kato et al. in a variety of such compounds they obtained σ_{TPA} in the range 43-330 GM.[175] Small chromophores with D-π-A structure comprising fluorene units also display similar σ_{TPA}, although the TPA effect can be certainly improved incorporating fluorene moieties into multibranched chromophores to reach values of σ_{TPA} in the order of 600-3000 GM.[58]

Figure 4.22a displays the σ_{TPA} measured for BT2 in different solvents. The recorded data indicate that for all solvents the maximum TPA cross-sections for BT2 is obtained at 750 nm, with a maximum value of nearly 1000 GM in THF solution. However, the non-linear response decreases notably in hexane, acetonitrile and methanol solutions, with measured σ_{TPA} values of 317, 238 and 236 GM, respectively. To summarize these results, Figure 4.22b presents the maximum value of σ_{TPA} for BT2 as a function of solvent dielectric constant. We can see that σ_{TPA} has a non-monotonic behavior with respect to the dielectric constant. It is evident that the interaction between the chromophore and solvent molecules produced enhanced ICT process (which is the basis of TPA response) with medium polar solvent such a THF, but such process was considerably reduced in non-polar (hexane) and polar (methanol) solvents. For the case of methanol, chromophore-solvent interactions were also responsible for strong fluorescence quenching effects. The relatively large σ_{TPA} values and high quantum yield exhibited by BT2 are attractive properties; in fact the two-photon activity of this chromophore is larger than those measured for commercial biomarkers, i.e., Rhodamine-Phalloidin with ~80 GM, open the possibility of use this material as contrast agent in fluorescence microscopy.[176]

Table 4.8 Summary of σ_{TPA} values of **BT2** compound at 750 nm.

Hexane	Toluene	THF	Acetone	Acetonitrile	Methanol
317	819	1000	660	238	236

TPA cross section given in GM units (1 GM = 10^{-50} cm^4 s).

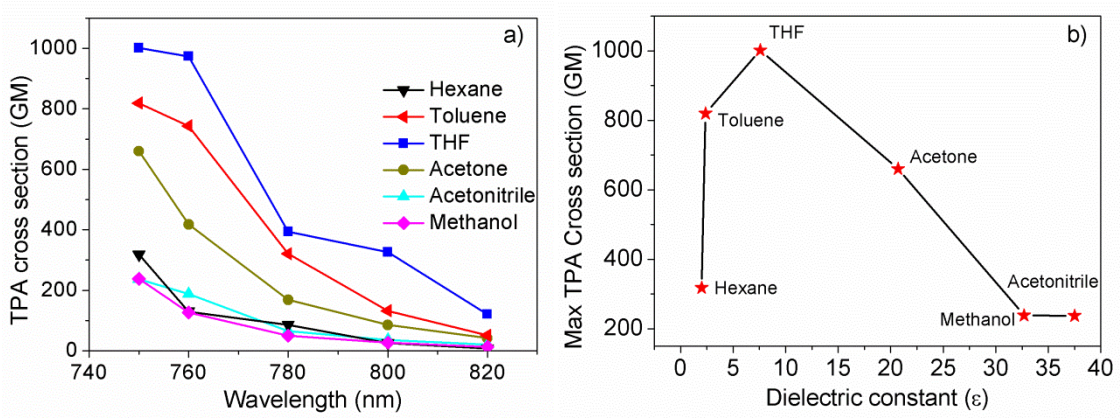

Fig. 4.22 a) TPA spectra of BT2 dissolved in hexane, toluene, THF, acetone, methanol, acetonitrile. b) Non-monotonic behavior of the maximum σ_{TPA} of BT2 as a function of dielectric constant for each solvent.

A parameter that plays a significant role on the TPA properties exhibited by organic chromophores is the molecular environment; this is because in solutions the dipole moments for ground and excited states are affected by solvent polarity. The effect of solvent polarity on TPA is not well understood yet, although some theoretical and experimental results show that the solvent effect on σ_{TPA} values for D-π-D and D-A-D systems displayed a nonmonotonic behavior with respect to solvent polarity.[176,177] In general, for these π-systems the highest σ_{TPA} values are obtained using solvents with low or intermediate polarity, although sometimes the highest σ_{TPA} values are observed in polar solvents, as in the case of dibenzothiophene core-branched structures.[178]

4.3.2.3 Fabrication of nanoparticles

Silica nanoparticles doped with BT2 (**BT2-SNPs**) were fabricated by microemulsion method where micelles were prepared by dissolving 0.22 g, 0.44g or 0.6g of Aerosol-OT, 300 μL of 1-butanol and 200 μL of NMP in 10 mL of deionized water by magnetic stirring. The rest of the conditions used in the fabrication of BT2-SNPs remained constant as were described in the Appendix C. The linear absorption spectra of the BT2-SNPs are shown in Figure 4.23. For the synthesis conditions of the BT2-SNPs used, the resulting mean particle sizes were of 97 nm, 58 nm and 51nm for the 0.2g, 0.4g and 0.6g of AOT, respectively. These values were revealed by scanning electron microscopy observation (Figure 4.24). It can be observed in the distribution graphs that the BT2-SNPs fabricated with 0.4g AOT

have a narrower size distribution than the other BT2-SNPs fabricated with 0.2g and 0.6g de AOT. For this reason, in the following studies and comparisons we use BT2-SNPs fabricated with 0.4g AOT.

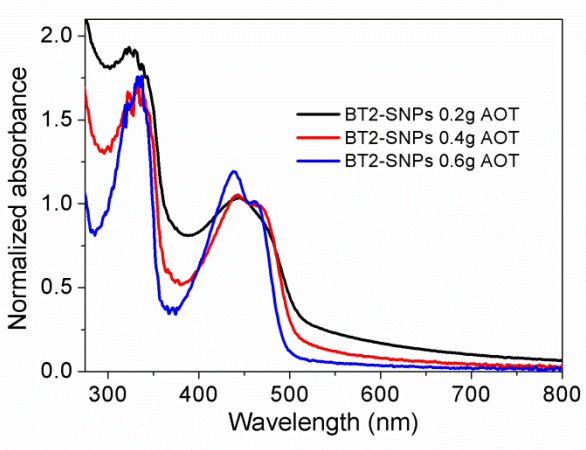

Fig. 4.23 UV-Vis normalized absorbance spectra of BT2-SNPs fabricated with 0.2g, 0.4g and 0.6g of AOT.

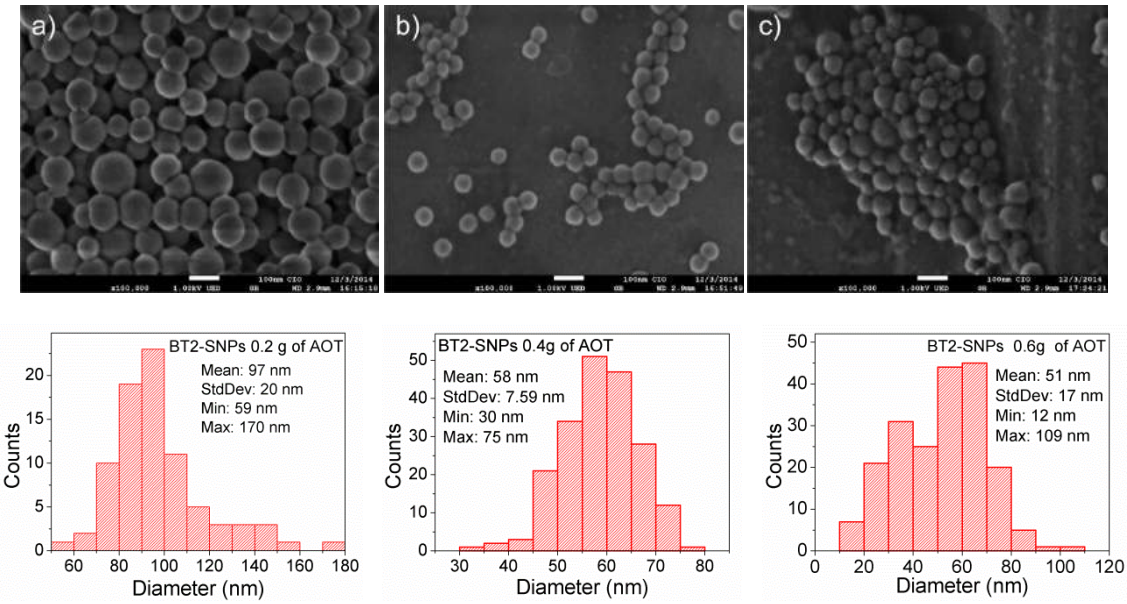

Fig. 4.24 TEM micrographs and size distribution graphs of BT2-SNPs obtained by different amount of AOT surfactant used in the fabrication process a) 0.2g, b) 0.4g and c) 0.6g.

Moreover, in order to know the weight percentage of BT2 relative to silica nanoparticle doped with them and functionalized with amino groups, a differential thermal analysis and

thermogravimetric analysis were performed. The sample BT2-SNPs lost 29.9 % of initial weight between 219 and 310°C. This weight loss corresponds to the organic molecule contained in the sample additionally of the vinyl and propyl groups. In table 4.9 are shown the results obtained.

Table 4.9 Results of thermogravimetric analysis of **BT2-SNPs.**

Temperature range ^{0}C	**Thermic process**	**% Loss**
21 – 219	No reaction	1.2
219 – 310	Exothermic	29.9
310 - 511	Exothermic	18.9
511 – 715	Exothermic	11.6
715 - 900	No reaction	0.01

To determine if the silica layer of BT2-SNPs is porous, the following experiment was performed: first, BT2-SNPs dispersed in water were centrifuged, the supernatant (water) was removed and the precipitate (BT2-SNPs) was redispersed in different proportions of THF and water (9:1, 8:2 and 7:3). Subsequently the absorption spectra of these samples were obtained and compared to the spectra of BT2-SNPs in water and molecule in THF. Once redispersed BT2-SNPs in the mixtures above mentioned, it is not possible to precipitate them by centrifugation again. From the absorption spectra shown in Figure 4.25, it was observed that when BT2-SNPs are redispersed in THF-water mixtures the absorption spectra match with the spectrum of the molecule in solution, which is different than when the molecule is forming BT2-SNPs. Thus we can conclude that the BT2-SNPs are porous. So, BT2-SNPs obtained by microemulsion method offer numerous advantages over other organic nanoparticles, such as well defined and tunable structures in terms of size (modifying the amount of surfactant, i.e. micelle size) and morphology.

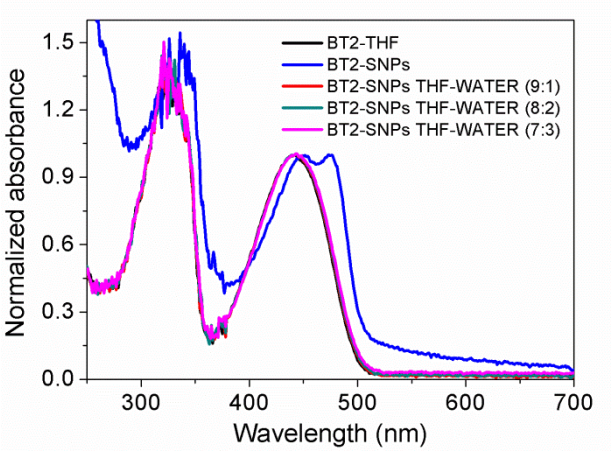

Fig. 4.25 Absorption spectra of BT2 in THF solution and FSNPs in THF-water mixtures.

Comparing the absorption spectra of BT2 in solution and BT2-SNPs, a shoulder was clearly observed at 465 nm. With the goal to clarify the reason for this observation, other nanoparticles were fabricated by reprecipitation method using CTAB or TRITON as medium stabilizer (conditions are shown in Appendix B). All BT2-NPs spectra were compared, in addition to BT2 films with and without polystyrene. Figure 4.26. In general, BT2 spectra both in NPs as BT2 films with and without polystyrene showed a broadening in the absorption band compared to the absorption band in solution. Presumably, this widening is due to the formation of charge-transfer complexes between the molecules BT2. Figure 4.27 shows the spectra of BT2-Hexane solutions, the first spectrum was obtained from a stock solution 20 µL (1mg / 2mL) with 3 mL of hexane, next, 20 µL of stock solution were added to the previous solution and the absorption spectrum was again obtained, this procedure was performed until the spectrometer allowed us to obtain the spectra without being saturated. We can observe a widening in the band corresponding to ICT transition when the concentration of the organic molecule is increased, which indicates that when the molecules are closer there are interactions between them.

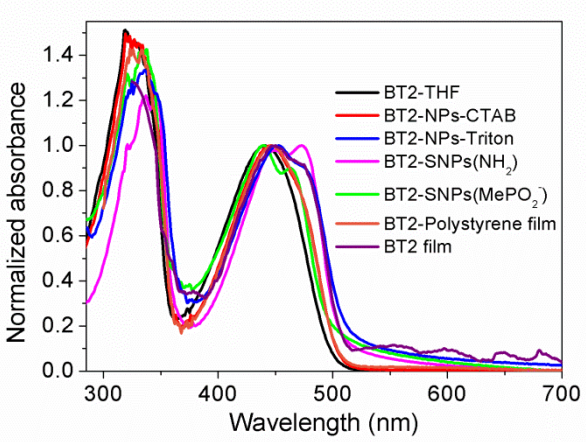

Fig. 4.26 a) Comparison of absorption spectra of BT2 in THF solution, BT2-NPs, BT2-SNPs and BT2 films. Comparing the absorption spectra of the BT2 in solution, BT2 film and BT2 nanoparticles, a shoulder was clearly observed in BT2 nanoparticles and BT2 film. Presumably, this widening is due to the formation of charge-transfer complexes between BT2 molecules.

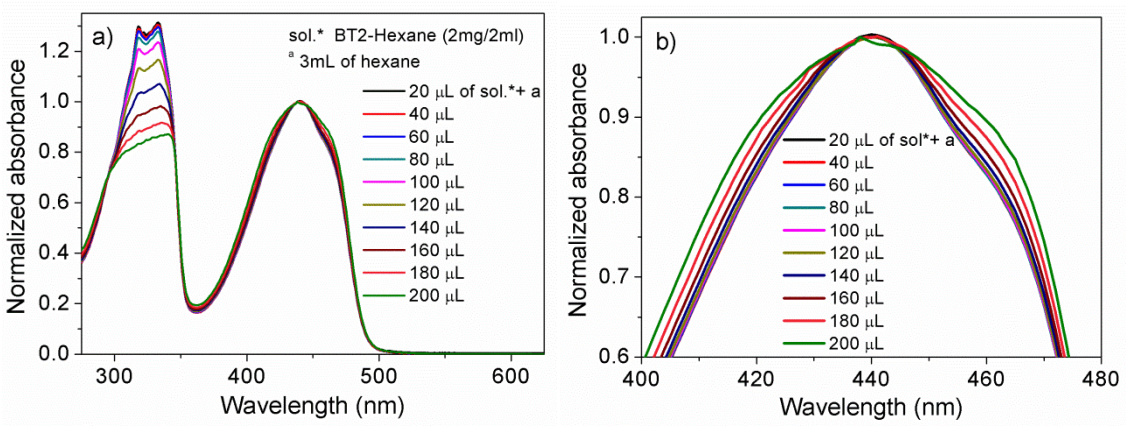

Fig. 4.27 Effect of the increase of BT2 concentration in hexane solution. When the concentration of BT2 increases a) a decrease of the band corresponding to $\pi \rightarrow \pi^*$ transition is observed and b) a widening of the band corresponding to ICT transition also is observed.

Other BT2 nanostructures were fabricated using three different types of polyethylene glycol (PEGs), **PEG 5000** (O- [2- (3-Mercaptopropionylamino) ethyl] -O'-methylpolyethylene glycol 5000, purchased from Sigma-Aldrich), **PEG 3400** (PEG Succinimidyl 3400 MW succinimidyl ester, INC NANOCS) and **PEG 2000** (1,2-distearoyl-sn-glycero-3-phosphoethanolamine-N- [methoxy (polyethylene glycol)-2000] (ammonium salt), purchased from Avanti Polar Lipids Inc.), average molecular weight is 5000 g/mol, 3400 g/mol and 2000g/mol, respectively. The nanostructures were fabricated by reprecipitation method. An aqueous solution of PEG at a concentration of 6 x 10^{-4}M was prepared. To 5mL of this solution 0.5mL of stock solution BT2 in THF (1mg/2mL) was injected and then the solvent was evaporated. Figure 4.28 shows absorption and emission spectra of the nanoparticles.

This type of nanoparticles (NPs-PEG) will be studied in a future work; it is a first approximation to obtaining a methodology for the fabrication of other type of organic nanoparticles poorly explored in our group and uses it with other fluorophores of interest. Some PEGs with functional groups or bioconjugated of interest that can be used to fabricate nanoparticles are Cholesterol PEG acid (CLS-PEG-COOH), Folic acid PEG acid (FA-PEG-COOH) and Folic acid PEG DSPE (FA-PEG-DSPE).

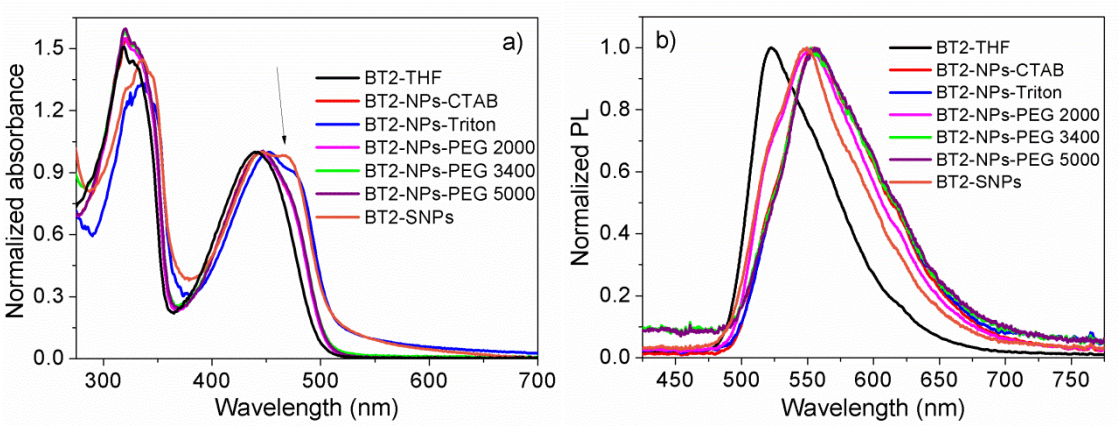

Fig. 4.28 b) Absorption and b) photoluminescence spectra of BT2 in THF solution, BT2-SNPs and BT2-PEG-NPs.

4.3.2.3 Comparative study of BT2-Nanoparticles fabricated by three different methods

In contrast to inorganic nanoparticles, in the literature there are no extensive studies about the influence of the synthesis method on the optical properties of O-NPs fabricated with a single type of molecule. In particular, little attention has been paid to the possible alterations of the linear absorption, quantum yield and fluorescence induced by two-photon absorption when a π-conjugated system is part of a nanoparticle. Motivated by this fact, a comparative study was performed on the linear and nonlinear optical properties and stability exhibited by **BT2** in: i) molecular solution, ii) O-NPs synthesized by RP method (**NPs-RP**), iii) O-NPs in aqueous solutions fabricated by Laser Ablation (**NPs-LA**) and, iv) fluorescent silica nanoparticles synthesized by microemulsion method **(NPs-ME)**.

In this section a change of notation for clarity on the comparative study of the nanoparticles fabricated by different methods was made, however it must be remembered that BT2-NPs and BT2-SNPs is equal to NPs-RP and NPs-ME, respectively.

BT2 nanoparticles fabricated by reprecipitation method (**NPs-RP**) were synthesized using cetyltrimethylammonium bromide (CTAB), tetrahydrofuran and milli Q water, the procedure is described in Appendix B.[110] To fabricate O-NPs via LA **(NPs-LA)** single organic crystals of BT2 and a Ti:Sapphire Regenarative Amplifier (800 nm wavelength, 60 fs FHWM pulse width, energy of 650 μJ/pulse, 1 kHz repetition rate) from Coherent Inc were used. The ejected nanoparticles obtained were caught by water and stabilized as nanocolloids with CTAB. Appendix D.

4.3.2.3.1 Size of the nanoparticles

The size of O-NPs is an important parameter for biomedical applications. In general, the size of O-NPs determines properties as luminescence intensity, penetration ability, intracellular mobility and cytotoxicity.[179] Therefore, O-NPs with appropriate sizes are essential for optimal image contrast. The mean sizes of the synthesized **BT2**-based nanoparticles were 25 nm for the case of **NPs-LA**, 34 nm for **NPs-RP** and 53 nm for **NPs-ME.** These values were estimated from SEM images (Figure 4.29) using the software ImageJ. SEM images reveal that laser ablation and reprecipitation methods tend to produce nanoparticles with irregular shape, while microemulsion method produce **BT2**-loaded silica nanoparticles of spherical shape. Among these O-NPs, the reprecipitation method produces some agglomerates. The insets in Figure 4.29 display histograms with the nanoparticles size dispersion (such agglomerates were not considered to estimate the nanoparticles size dispersion in the case of **NPs-RP**).

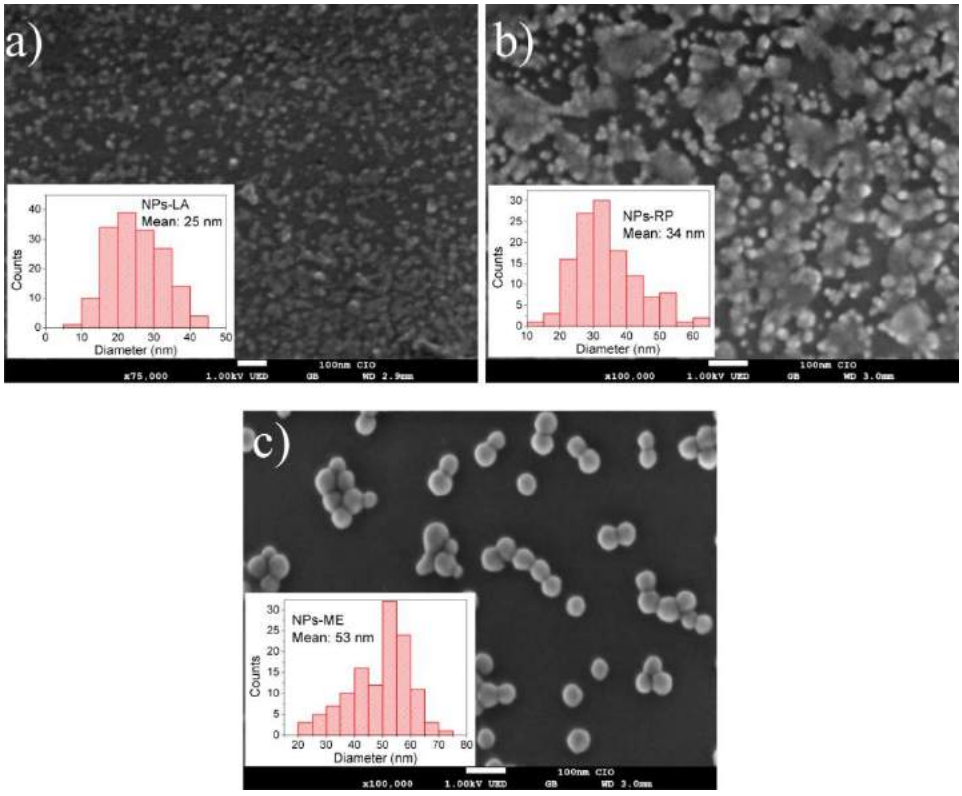

Fig. 4.29 SEM micrographs of **BT2**-NPs obtained by different fabrication methods a) reprecipitation, b) laser ablation and c) microemulsion.

4.3.2.3.2 Linear Optical Properties

Linear absorption

For comparison purposes, suspensions of nanoparticles of **BT2** synthesized by reprecipitation, laser ablation and microemulsion were prepared by dilution at the same concentration (1×10^{-6} M). In addition, a solution of **BT2** in THF (**BT2-THF**) was prepared also at the same concentration. The UV-Vis absorption spectra of **BT2-THF** and suspensions of nanoparticles are shown in Figure 4.30. Distinctive characteristics for each sample are clearly observed. For instance, while the maximum absorption band of **BT2-THF** is at 439 nm, in the case of **NPs-RP** and **NPs-ME** the maximum is red-shifted to 445 nm and 443, respectively. **NPs-ME** also exhibited a small shoulder at 465 nm. The optical characteristics of **NPs-ME** were practically the same independently of the precursors (APTES or THPMP) used to modify the surface of such nanoparticles with amine groups (NH_2) or methyl phosphonate groups ($MePO_2^-$). For the case of **NPs-LA**, a slight blue-shift is observed in their maximum of absorption (438 nm) compared to **BT2-THF.** The molar absorption was calculated for all O-NPs, resulting a maximum value in the order of 30 000 $M^{-1}cm^{-1}$.

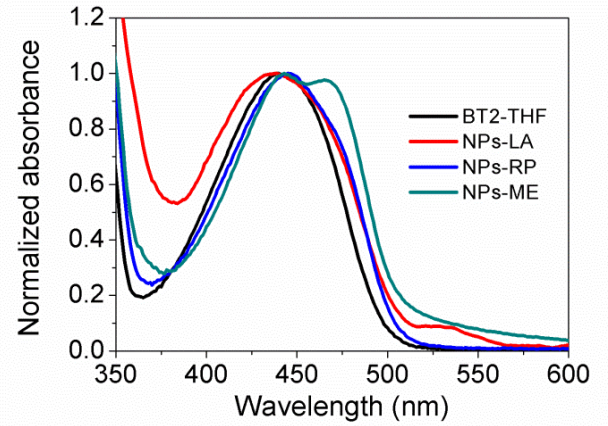

Fig. 4.30 UV-Vis normalized absorption spectra of **BT2-THF, NPs-LA**, **NPs- RP** and **NPs-ME** obtained at the concentration of 1 μM.

Photoluminescence properties

One-photon excited fluorescence spectra of **BT2** in solutions, microcrystal (before laser ablation) and aqueous suspensions of **BT2-NPs** (at the same concentration of **BT2**) were obtained using an excitation wavelength of 375 nm. Figure 4.31. Emission spectra undergo wavelength shifting for the nanoparticles. In particular, the **BT2** processed as **NPs-RP** and

NPs-ME exhibited a notorious red-shifting of the emission peak compared with **BT2** in solution, the maxima are red-shifted 32 and 26 nm, respectively compared with the peak of **BT2-THF** while the maximum emission for **NPs-LA** exhibited a small blue-shifting and a notorious change in the spectrum emission width.

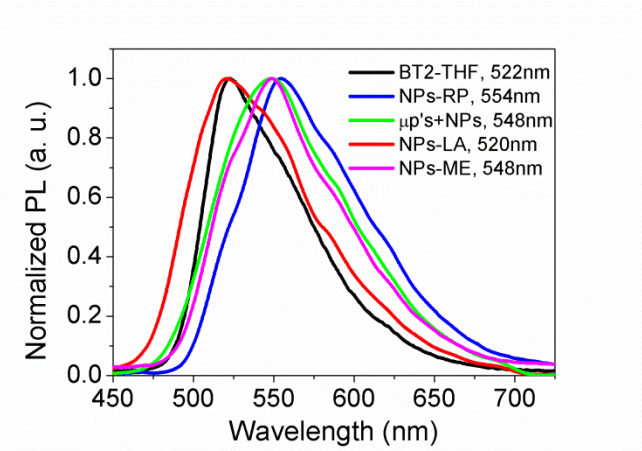

Fig. 4.31 Normalized photoluminescence (PL) spectra for BT2 in solution and aqueous suspensions of nanoparticles.

Fluorescence lifetime measurements

Fluorescence lifetimes were obtained at room temperature by the time correlated single photon counting (TCSPC) technique on a Horiba Jobin Yvon TemPro instrument with a nanoLED laser of 455 nm excitation. A 0.01% suspension of Ludox AS40 (Aldrich) in ultrapure water was used for the prompt signal. Calibration of the equipment was realized with a POPOP [1,4-Bis(4-methyl-5-phenyl-2-oxazolyl)benzene] methanol solution (optical density <0.1 and lifetime of 0.93ns.[180] The samples under test were at the concentration of 1 μM. Data were fitted in the software DAS6 available with the equipment.

The fluorescence lifetime of **BT2-THF** presents a mono-exponential decay with a lifetime of 3.42 ns (see Figure 4.32). The observed fluorescence decay profiles for the O-NPs suspensions had a bi-exponential decay. For instance, for the case of **NPs-LA** the fluorescence decay had a fast component (that accounts for approximately 65% of the signal) with a time constant τ_1 of 0.23 ns and a slow component (about 35%) with a time constant τ_2 of 3.61 ns. For the case of **NPs-RP** the fast component (about 69%) had a τ_1 value of 0.09 ns and the slow component (about 31% of the signal) a τ_2 value of 3.44 ns. As we can see, the time constants τ_2 corresponding to the slow components of the signals from **NPs-LA** and **NPs-RP** are similar to the fluorescence lifetime of the molecular solutions **BT2-THF**. The fast decay components τ_1 arise from the molecular interactions that take

place in nanoparticles. Moreover, the differentiated behavior of the fluorescence decay between **NPs-LA** and **NPs-RP** means that **BT2** is possibly assembled in different manner in each case. In particular, it can be suggested that **NPs-LA** are nanocrystals as they resulted from the ablation and fragmentation of microcrystals while **NPs-RP** are amorphous nanoparticles as they resulted from the nano-aggregation of molecules.

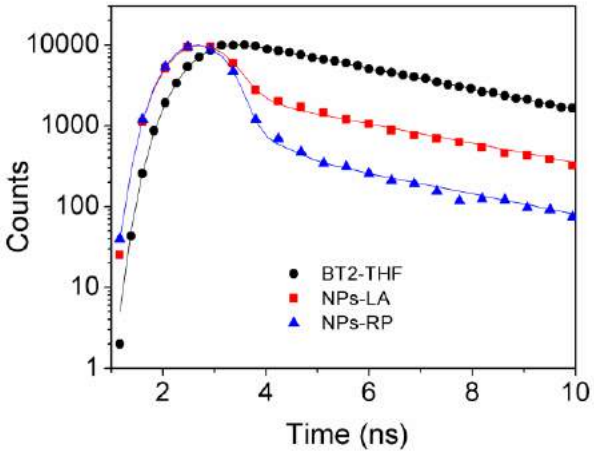

Fig. 4.32 Fluorescence decay curves of **BT2-THF**, **NPs-LA** and **NPs-RP**.

4.3.2.3.3 Two-Photon Absorption

Two-photon absorption (TPA) is a property of paramount importance when O-NPs are intended for application such as the imaging of biological samples through multiphoton microscopy. The values for our samples at 1 μM were measured through the TPEF technique.[181] The maximum TPA cross section was of nearly 1000 GM for **BT2-THF** measured at 750 nm (see Figure 4.33). O-NPs exhibited similar spectra of nonlinear absorption but with decreased values of their maximum TPA cross sections. The maximum σ_{TPA} values were 790 GM, 600 GM and 545 GM for **NPs-LA**, **NPs-RP** and **NPs-ME**, respectively. So, **NPs-LA** exhibited the most intense luminescence among all NPs studied and a little decrease in the TPA cross section.

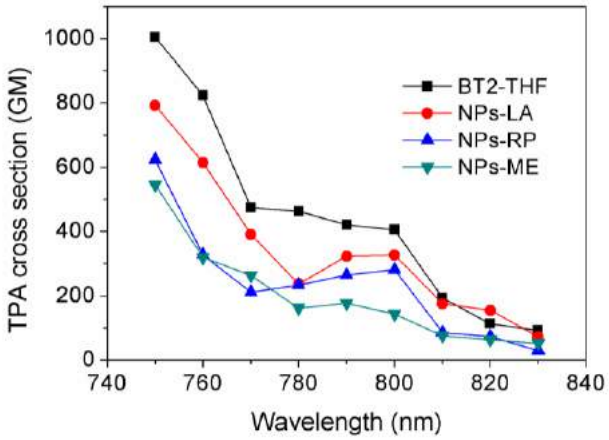

Fig. 4.33 Two-photon absorption spectra of **BT2** in solutions and aqueous suspensions of nanoparticles.

4.3.2.3.4 Photostability

It is well known that most of commercial fluorophores used as labels and markers in fluorescent microscopy suffer of photodegradation after few minutes of excitation. The integration of fluorophores into nanostructures can alleviate photodegradation effects. To evaluate the photostability of molecular solution and O-NPs based on **BT2**, the samples were exposed to the focused illumination from a 150 watts Xenon lamp. The peak of emission of samples was then monitored over different intervals of time. Figure 4.34 illustrates the decay in the intensity of photoluminescence during the degradation experiment. The molecular solution **BT2-THF** showed a total photodegradation after 45 minutes. In contrast, O-NPs exhibited only a partial decay of photoluminescence after 45 minutes of being exposed to irradiation, with 72% (**NPs-LA),** 50% (**NPs-RP)** and 28% (**NPs-ME)** of the original intensity. Interestingly, after two hours of exposure to constant irradiation from the Xenon lamp, the O-NPs still exhibited photoluminescence. Clearly, the formation of nanoparticles is a good option to prevent irreversible photodegradation of the fluorophores. Such photodegradation is often caused by a photo-oxidation reaction when molecular oxygen is present. When **BT2** is covered with surfactant micelles (in the case of **NPs-LA** and **NPs-RP**) or encapsulated within the silica matrix (**NPs-ME**), the reaction with oxygen is then significantly hindered. Reduction in the photobleaching effect is very useful for long time bio-imaging.

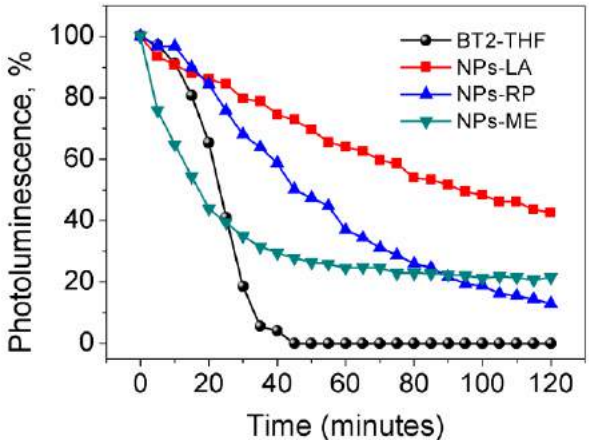

Fig. 4.34 Photostability of **BT2** in molecular solution (THF) and aqueous suspensions nanoparticles. Samples were exposed to illumination from a Xenon lamp and the photoluminescence was measured as a function of exposition time.

Photophysical properties of **BT2-NPs** were obtained from the absorption, fluorescence, and Two-photon absorption spectra as well as photostability curve and summarized in Table 4.10.

Table 4.10 Photophysical Properties of fluorescent organic nanoparticles and BT2 in THF solution.

Type of NPs	Fabrication method	Mean size (nm)	Absorption λ_{max}(nm)	Emission λ_{max} (nm)	Φ_F	$\tau^{a)}$ (ns)	σ_{TPA} (GM)	PL after 2 hours of illumination (%)
BT2-THF	Solution	-	439	522	0.87	3.42	1000	0
NPs- LA	Laser ablation	25	438	520	0.86	0.23 (3.61)[b]	790	42
NPs-RP	Reprecipitation	34	445	554	0.83	0.09 (3.44)[b]	600	12
NPs-ME	Microemulsion	53	443, 465	548	0.8	-	545	21

[a] Fluorescence lifetime
[b] Time constant of the slow fluorescence decay component

4.3.3 Functionalization and bioconjugation

The functionalization of fluorescent silica nanoparticles with amino groups (NH_2) was simple because a silica precursor containing this group was used during the fabrication procedure. An accurate determination of the amino groups in the surface of the silica

nanoparticles doped with BT2 (BT2-SNPs) before or after modification may be important for the evaluation of the reaction yield or suitability for subsequent croosslinking procedures. In the literature there is an assay called TNBS (2,4,6-Trinitrobenzene Sulfonic Acid) that allows to realize counts by simple spectrophotometric absorption measurements.[115] Subsequently, functionalizations on surface of the BT2-SNPs with different groups as carbonyl (CHO) were realized in order to obtain bioconjugated BT2-SNPs with folic acid and transferrin. The methods used to obtain bioconjugated BT2-SNPs are shown in Appendix E.

To obtain CHO groups, a modification of the BT2-SNPs with the most popular *bis*-aldehyde homobifunctional crosslinker Glutaraldehyde (GA) was realized (Figure 4.35).[115] Different quantities of Glutaraldehyde (always was considered a molar excess over the amount of amines to be modified) were added to BT2-SNPs suspension using buffers as sodium phosphate, HEPES and sodium acetate. Then, to remove excess glutaraldehyde, BT2-SNPs were washed with coupling buffer at least several times using centrifugation.

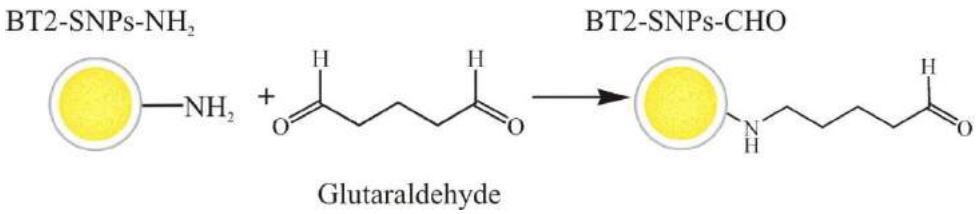

Fig. 4.35 Functionalization of BT2-SNPs with carbonyl groups.

It has been reported in the literature that fluorescent silica nanoparticles with amino groups can penetrate nonspecifically into the cells;[28] motivated by this fact and thinking in future studies, BT2-SNPs were functionalized with other functional groups to finally obtain acetylated and carboxylic BT2-SNPs to inhibit their internalization (Figure 4.36). Also, they can be used as a negative control and compare the cellular uptake of all fabricated BT2-SNPs, both functionalized as bioconjugated BT2-SNPs.

BT2-SNPs modified with succinic anhydride to create terminal carboxylate functionalities may be further conjugated to other bio-molecules of interest. Succinic anhydride was used to block amino groups and to convert an existing functionality into a carboxylic acid in buffers as Sodium acetate and potassium carbonate in a 0.1–1.0 M concentration.

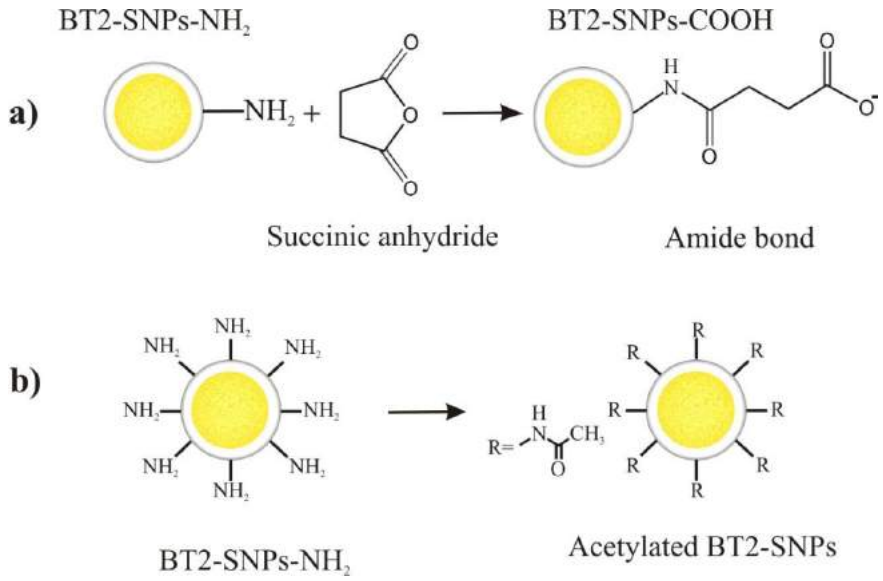

Fig. 4.36 a) BT2-SNPs functionalized with carboxyl groups. Succinic anhydride reacts with primary amine groups in a ring-opening process, forming an amide bond and a terminal carboxylate. b) BT2-SNPs functionalized with amide group (acetylated BT2-SNPs) to inhibit the internalization into cells.

The functionalization and bioconjugation of BT2-SNPs surface can be confirmed from the changes in the electrostatic charge, which could be analyzed by electrophoresis. This technique is based on the mobility of the nanoparticles through the agarose gel promoted by electric field. This mobility is affected for an increased overall size of the nanoparticles, as well as a modification in the surface charge and the intensity of the electric field applied. The photoluminiscence properties of BT2-SNPs allow direct visualization of their mobility after the electrophoresis experiment. A shift in a lane relative to BT2-SNPs-NH_2 (control) in the agarose gel corresponds to a successful functionalization and bioconjugation of BT2-SNPs.

For the functionalization of BT2-SNPs with carbonyl groups, different amounts of GA (12, 36 and 60 μL) in Sodium phosphate, Sodium acetate and Hepes buffers were used to obtain BT2-SNPs-CHO (intermediate step to bioconjugate the BT2-SNPs-NH_2 with folic acid or transferring, route S2, Apendix D). To evaluate the best functionalization with carbonyl groups, an electrophoresis on agarose gel containing 0.5 % TAE after applying a 90 mV voltage for 30 min and using TAE as electrophoresis electrolyte was realized. Figure 4.37. The results showed a better surface modification of BT2-SNPs-NH_2 with Hepes buffer and there is not difference between use 36 or 60 μL of GA.

Fig. 4.37 Agarose gel electrophoresis showing comparative methodologies to functionalize BT2-SNPs-NH_2 with CHO group. (Lane 1) fluorescent molecule BT2, (Lane 2) BT2-SNPs with amino groups used as control or reference, (Lanes 3-5) BT2-SNPs functionalized with 12, 36 and 60 µL of GA, respectively using hepes buffer, (Lanes 6-8) BT2-SNPs functionalized with 12, 36 and 60 µL of GA, respectively using Sodium phosphate buffer.

Figure 4.38 shows the electrophoresis gel of BT2-SNPs-FA (bioconjugated by route 1 Apendix D) and BT2-SNPs-CHO fabricated using 36 µL of GA and the 3 buffers (Sodium phosphate, Sodium acetate and Hepes). The result of the electrophoresis showed a greater mobility of BT2-SNPs-CHO when Hepes buffer is used and moreover, the mobility of BT2-SNPs-FA loaded in the well 4 and fluorescence of folic acid showed that bioconjugation was carried out.

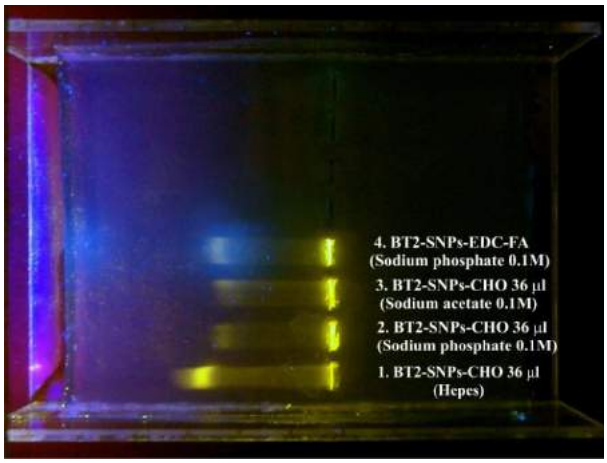

Fig. 4.38. Agarose gel electrophoresis showing BT2-SNPs-NH_2 modified with 36 µl of GA in Hepes (lane 1), Sodium phosphate (lane 2), Sodium acetate (lane 3) buffer and BT2-SNPs-FA (route 1).

In conclusion, we have synthesized nanoparticles, having a covalently incorporated fluorophore BT2, with a variety of functional groups on their surface (amine, carbonyl, carboxyl, and amide). These nanoparticles were conjugated to folic acid to be selective targeting to cancer cells. However, the work in this dissertation was limited to demonstrate bioimaging using the synthesized nanoparticles; it was decided to leave for future work the demonstration of selective cellular uptake of these nanoparticles. Nevertheless, the results obtained in this dissertation are the foundation for the development of theranostic multifunctional nanoparticles, combining the conjugation of other suitable fluorophores (e.g., dyes with TPA properties) and incorporating therapeutic molecules, drugs, for the purpose of combined diagnosis and therapy.

CHAPTER 5

Organic nanostructures as contrast agents in confocal and two-photon microscopy

A useful parameter for determining whether a material has potential applications as a contrast agent (fluorescent probe) in confocal microscopy is its brightness, which is defined as the product of the maximum molar absorbance and the quantum yield of fluorescence. For confocal microscopy the fluorescence from the probe is produced via one-photon excitation. It has been reported that a material does not have practical application if its brightness is below than 5000 $M^{-1}cm^{-1}$.[182] The O-NPs under this study (fabricated with monomer **M1**, polymer **P1** and **BT2**) surpass this limit as they exhibit typical molar absorbance and they have high quantum yields of fluorescence. Likewise, for multiphoton microscopy the brightness or figure of merit for a good contrast agent is the product of the TPA cross section and the quantum yield. According to Table 4.2 and Table 4.9, our O-NPs have a good brightness (typically $\Phi \times \sigma_{TPA} \geq 500$ GM) compared with most of commercially available dyes for multiphoton microscopy which are limited by typical TPA cross sections in the range 0.1-100 GM.[2]

Although bodipyies also have acceptable TPA properties, they are not used for cell staining in this thesis. However, our colleagues at the Hangzhou Normal University in China continued with this work, other nanostructures were fabricated in which the dyes were encapsulated with the biopolymer 1,2-sistearoyl-*sn*-glycero-3-phosphoethanolamine-*N*-[methoxy(polyethylene glycol)-2000] and demonstrated its potential use as contrast agents in MCF-7 breast cancer cells.

In this chapter the results of the *in vitro* cytotoxicity of **M1** and **P1** nanoparticles to A549 and HeLa cells as well as the micrographs obtained by the multiphoton microscope are presented. Moreover, it is presented for the first time (to the best of our knowledge) the use of O-NPs synthesized by LA as exogenous fluorescent agents in two-photon microscopy. Finally, a comparison of micrographs (under similar experimental conditions) of HeLa cells using **BT2-NPs** fabricated by three methods is presented.

5.1 Cell staining

HeLa (line derived from cervical cancer) and A549 (line derived from lung adenocarcinoma) cells were cultivated in Dulbecco's minimum essential media (DMEM) with 10% fetal bovine serum (FBS), 1% penicillin-streptomycin solution and 2mM

glutamine at 37°C in an atmosphere with 5% CO_2 until a confluence of 70-80%. Then the cells were washed twice with phosphate-buffered saline (1X PBS). After fixation with 4% paraformaldehyde, the fluorescent samples (**M1**-NPs, **P1**-NPs, **M1**-SNPs or **P1**-SNPs) were added and the cells were incubated for 1 hr at room temperature away from light. Then the volume was removed and the cells were washed once with 1X PBS. Cell nucleus was stained with 1 μM of Hoechst 33258. Finally the cells were imaged through a Leica TCS-SP5 MP two-photon laser scanning microscope (Leica Microsystem, Wetzlar Germany).

5.2 Cell viability

In vitro cytotoxicity of nanoparticles and silica-loaded nanoparticles to A549 and HeLa cells was investigated by MTT assay. All tests were performed using suspensions with different concentration of nanoparticles (see Figure 5.1). First, we compared the toxicity of nanoparticles stabilized with CTAB and Triton X-100, that is, **M1**(**P1**)-NPs-CTAB and **M1**(**P1**)-NPs TRITON, finding that at the concentration of 7.5×10^{-5} M for **M**1 and 4.1×10^{-7} M for **P1** (denoted in the figure as no dilution), respectively, there is no cell viability. In the case of **M1**(**P1**)-NPs-TRITON viabilities greater than 50% are achieved in A549 and HeLa cells after 1:4 and 1:32 dilution of the suspensions, respectively, while for **M1**(**P1**)-NPs-CTAB the viabilities remained very poor compared with **M1**(**P1**)-NPs-TRITON even at more diluted suspensions, in particular for the case of HeLa cells. The low viability of **M1**(**P1**) nanoparticles synthesized through the reprecipitation method either with the use of CTAB or TRITON was substantially improved in silica nanoparticles loaded with **M1** or **P1**. For instance, Figure 5.1a shows that at the relatively high concentrations (1:1 dilutions) of 5.2×10^{-5} M and 3.1×10^{-7} M for **M1**-SNPs and **P1**-SNPs, respectively, the viability in A549 cells is approximately 80%, which is higher than in **M1**(**P1**)-NPs-CTAB and **M1**(**P1**)-NPs-TRITON. Similarly, Figure 5.1b shows how the viability is also improved in HeLa cells through the use of loaded silica nanoparticles, although in this case viabilities higher than 80% are obtained in 1:8 dilutions. These results provide clear evidence of the importance of encapsulating the TPA materials in order to reduce their cytotoxicity.

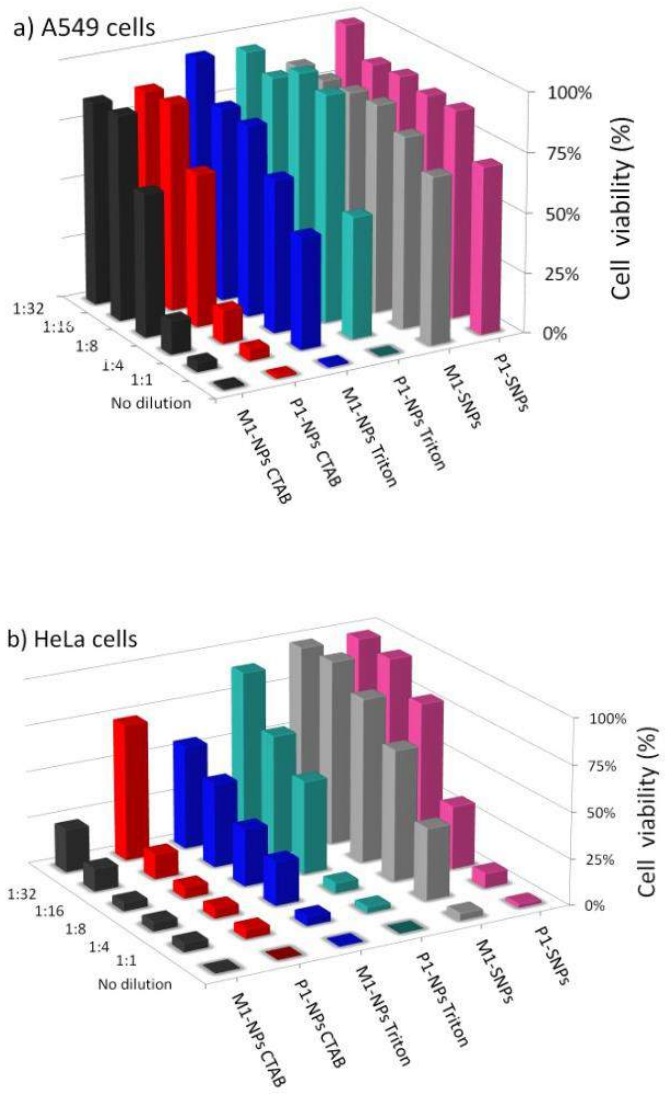

Fig. 5.1 Viability of a) A546 cells and b) HeLA cells cultured after the addition of aqueous suspensions at different dilutions of **M1**(**PI**)-NPs (stabilized with surfactants such as CTAB and Triton X-100) and **M1**(**P1**)-SNPs. The concentrations of suspensions before dilution were 7.5×10^{-5} M (**M1**-NPs), 4.1×10^{-7} M (**P1**-NPs), 5.2×10^{-5} M (**M1**-SNPs) and 3.1×10^{-7} M (**P1**-SNPs).

5.3 Fluorescence Microscopy

5.3.1 Fluorescence images of HeLa cells treated with M1(P1)-NPs

One-photon and two-photon fluorescence microscopy was used to study the uptake of all samples under study. For example, Figure 5.2 displays micrographs of He-La cells treated with **P1**-NPs and **P1**-SNPs as fluorescent probes and Hoechst 33258 to stain specifically

the nucleus of cells (Hoechst 33258 is a commercially available dye). For the case of one-photon excitation the cells were illuminated with a wavelength of 488 nm (micrographs in the first and third row) while 740 nm was used for two-photon illumination (micrographs in the second and fourth row). For clarity, the images were taken with green and blue filters to identify nanoparticles (left column) and nucleus (middle column), respectively. The column at the right is the merging of both images. Notice that under illumination at 740 the nucleus of cells (micrographs E and K) is not detected due to the poor two-photon activity of Hoechst 33258 at such wavelength. Figure 5.2 shows clearly that **P1**-NPs (micrographs A, B, C, D and F) and **P1**-SNPs (micrographs G, H, I, J and L) penetrated the cells and reversibly stained the cytoplasm, without specific binding to cellular components. This was expected, since for the particular case of **P1**-SNPs no specific treatment was followed after silica encapsulation to conjugate the nanoparticle surface. Similar micrographs were obtained from cells treated with nanoparticles synthesized from **M1** but with the use of suspensions with larger concentrations due to the lower two-photon activity of such samples. The concentrations used to obtain these micrographs were the same as for cytotoxicity tests before dilution.

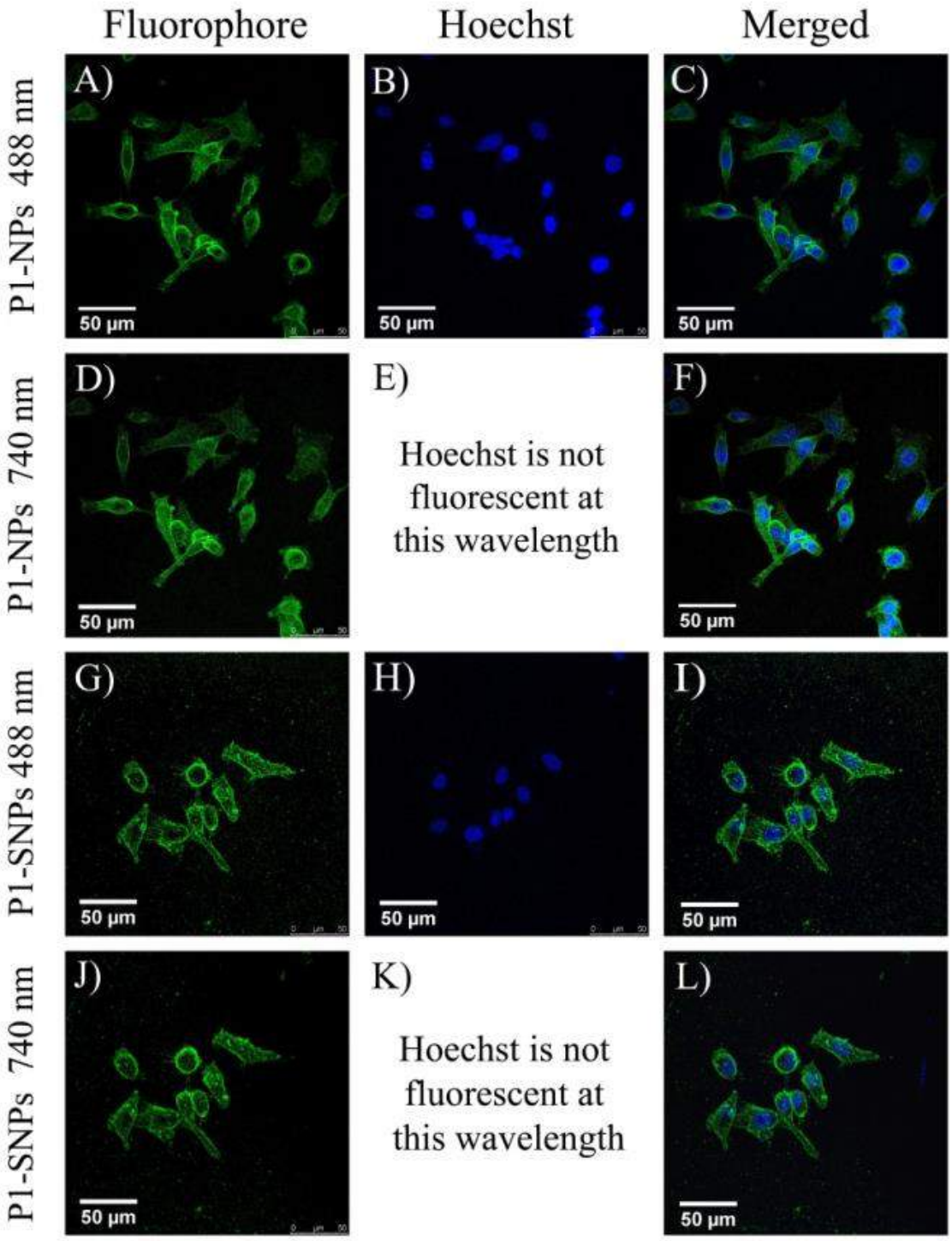

Fig. 5.2 One-photon (first and third row) and two-photon (second and fourth row) fluorescence images of HeLa cells treated with Hoechst 33258 and **P1**-NPs (A, B, C, D, F) and **P1**-SNPs (G, H, I, J, L). Left column: images taken with green filter to identify cytoplasm stained by nanoparticles under test. Middle column: the images taken with blue filter. Right column: superposition of images from the left and middle column. The wavelengths for one- and two-photon excitation is indicated to the left of the columns.

5.3.2 Fluorescence images of HeLa cells treated with BT2-NPs

Confocal (one-photon excitation at the visible wavelength of 488 nm) and multiphoton (two-photon excitation at the infra-red wavelength of 740 nm) microscopy were used to study the uptake of O-NPs by HeLa cells (human cervical cancer cell line). For comparison purposes, in all cases the cells were treated with aqueous suspension at the same concentration (1μM). Figure 5.3 displays micrographs of HeLa cells treated with **NPs-LA**, **NPs-RP**, and **NPs-ME** as fluorescent probes. The micrographs corresponding to one-photon imaging (first row in the figure) were obtained by setting the confocal microscope with the same parameters of image acquisition, i.e., laser excitation intensity, scanning times, gain of detectors, etc. Similar procedure was followed for the two-photon imaging (second row in the figure). The confocal micrographs show that the nanoparticles (with greenish light emission) penetrated nonspecifically into the HeLa cells and remained mainly in the cytoplasm. In this case DAPI dye was used to stain specifically the nucleus of cells. The blue emission is from DAPI dye bound to rich regions of DNA in the nucleus. In regards to the microscopy performed with two-photon excitation (second row of the figure), light emission from the nanoparticles is detected from cytoplasm, although the cell nuclei is no longer observed due to the very small TPA activity of DAPI (~ 37 GM).[183] **NPs-RP** produced images of relatively poor quality compared with those obtained with **NPs-LA**. This is an interesting result since in both cases the samples were treated with suspensions of nanoparticles of the same concentration and stabilized with the same surfactant (CTAB). Micrographs show cellular uptake of NPs-ME, but images of less quality compared with those obtained with **NPs-LA** and **NPs-RP**. There was not significant difference in the images obtained with **NPs-ME** whose surfaces were functionalized with either amino or methyl phosphonate groups.

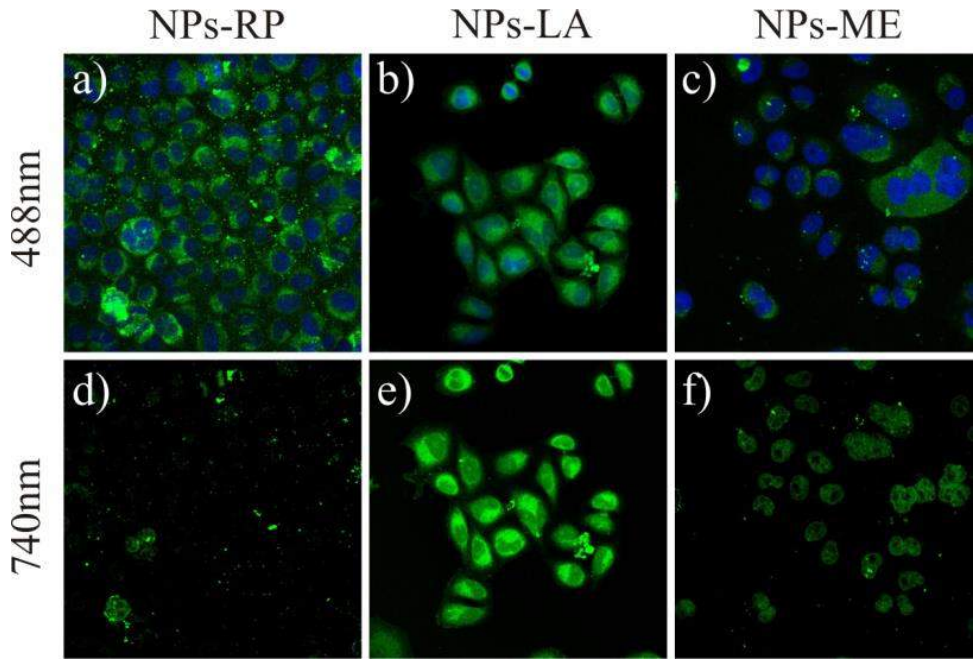

Figure 5.3 One-photon (first row) and two-photon (second row) fluorescence images of HeLa cells treated with a) **NPs-RP,** b) **NPs-LA**, and c) **NPs-ME**. The wavelengths for one- and two-photon excitation are indicated to the left of the columns. The micrographs corresponding to the first row were obtained by setting the confocal microscope with the same parameters of image acquisition. Similar procedure was followed for the two-photon imaging.

Two-photon micrographs were again obtained but now optimizing the laser output level in the utilized microscope for the particular case of each sample, as shown in Figure 5.4. The rest of the parameters for image acquisition were set equal for all samples. In this case, the micrograph of HeLa cells treated with **NPs-LA** were obtained with only 1% of laser excitation output level, while for the cases of **NPs-RP** and **NPs-ME** the levels were 2% and 4%, respectively. Thus, images of comparable quality are obtained with **NPs-LA** and **NPs-RP**, but in the latter case twice of laser excitation is required. In regards to samples treated with **NPs-ME** the imaging of cellular structure resulted rather poor. Presumably, the relatively large size of our **NPs-ME** limited their penetration ability into cells compared with **NPs-RP** and **NPs-LA**. Jin and co-workers studied the effect of size on the penetrating ability of NPs fabricated by ME and they showed that the small NPs (23±3 nm) clearly penetrated the cells much faster than larger NPs (85±5 nm).[88] In addition, the better image quality achieved with **NPs-LA** is assigned to their larger values of σ_{TPA} (see Figure 4.33).

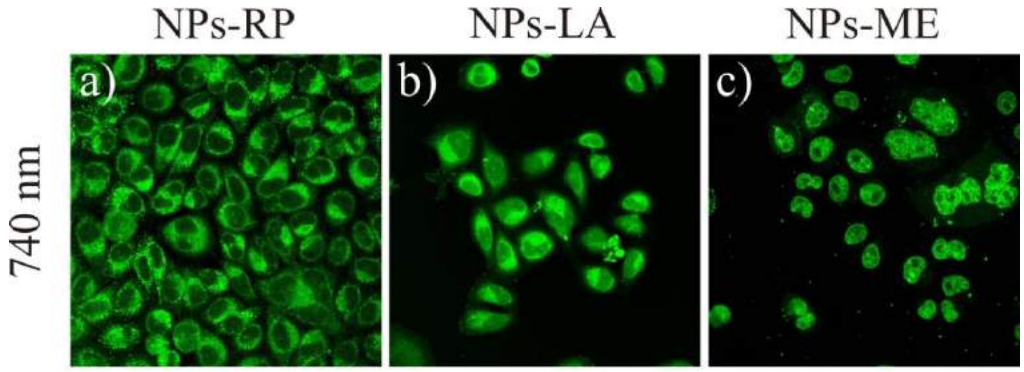

Fig. 5.4 Two-photon images of HeLa cells treated with a) **NPs-RP**, b) **NPs-LA**, and c) **NPs-ME**. In each case, the laser output level for image acquisition was optimized keeping constant the remaining parameters in the microscope.

Conclusions

In conclusion, with this work, a new line of research related to the development of contrast agents and markers for confocal and multiphoton microscopy within the GPOM group was opened and to our knowledge there is not another group in Mexico working on this research line. It is noteworthy that this thesis was multidisciplinary, areas such as chemistry, materials engineering, photonics and life sciences joined together and the result was the design of fluorescent materials, processing of these materials in different nanostructures, physical-chemical characterization and finally their application as contrast agent in confocal and two-photon microscopy.

Linear and nonlinear optical properties of a series of luminescent materials such as borinates, BODIPYs and fluorine derivates were investigated. All borinates exhibit fluorescence induced by absorption of one- or two-photons at the wavelengths about 400 and 800 nm, respectively. The highest two-photon absorption cross-section (σ_{TPA} = 174 GM) of the series of studied compounds corresponds to 5h with a D–π–C=N^+–π–A (D = NEt_2 and A = $COOCH_2CH_3$) architecture.

Three different **BODIPIES** with tetraphenylethene (TPE) units were investigated to gain a deeper insight into the structure–property relationship of these BODIPY luminogens. The accumulation of TPE units can not only ameliorate the fluorescence emission in the aggregate state but also benefit the TPA and TPEF properties of the luminogens. 3TPE-BODIPY shows the best nonlinear optical property, with the highest σ_{TPA} and σ_{TPEF} values of 264 and 116 GM, respectively, when its THF solution is pumped with laser pulses at wavelength of 810 nm.

Moreover, a comparative study of the two-photon action from a fluorene-based monomer and its polymer when they were molecularly dissolved, agglomerated in nanoparticles and encapsulated into silica nanoparticles was realized. In particular, the polymer-doped silica nanoparticles gave high nonlinearities, on the order of 10^3 GM, excellent quantum yields with good photostability. To the best of our knowledge, this is the first time that polymer-doped silica nanoparticles have been fully characterized for their TPA and TPEF properties.

On the other hand, a novel stable fluorene derivative with D-A-D architecture (**BT2**) was studied; the linear and non-linear absorption and the photoluminescence properties were recorded in several solvents. These photophysical properties were strongly affected by the solvents and did not show a monotonic trend with respect to solvent polarity. The maximum two-photon absorption cross-section obtained was σ_{TPA} = 1000 GM at 750 nm and a fluorescence quantum yield of Φ_F ~0.87 in THF. The two-photon activity decreased

slightly (about 1.3 times) in toluene (non-polar solvent) and acetone (polar aprotic solvent), but it was substantially reduced (about 4.2 times) in polar protic solvents such as methanol.

Besides, organic florescent nanoparticles of **BT2** by three different methods (laser ablation, reprecipitation and microemulsion) were successfully prepared. It was found that using any of the three methods the fluorescence quantum yield of nanoparticles is similar (~ 0.8), although the largest TPA cross section was achieved for nanoparticles produced by laser ablation. The photostability of all the **BT2**-based nanoparticles under study was notably better in comparison to molecular solution of **BT2**; the best photostability corresponds to nanoparticle obtained by laser ablation method.

All properties exhibited by aqueous suspensions of nanoparticles of Fluorene-chromophores (polymer **P1** and **BT2**) are attractive for possible applications as fluorescent contrast agents utilized in fluorescence microscopy. Although bodipyies also have acceptable TPA properties, they are not used for cell staining in this thesis.

The brightness exhibited by these nanoparticles is suitable for confocal or two-photon microscopy. **M1** and polymer **P1** were employed as contrast agents for the visualization of HeLa cells using confocal and two-photon microscopy. Using MTT assay the viability was investigated for **M1**and **P1** in NPs and FSNPs, the results provide clear evidence of the importance of encapsulating the TPA materials in order to reduce their cytotoxicity.

Finally, **BT2-NPs** (fabricated by reprecipitation, ablation and microemulsion method) were employed to as exogenous agents for the visualization of HeLa cells using confocal and two-photon microscopy, under similar experimental conditions. Particularly, the results showed that laser ablation could be a worthy and alternative approach for the fabrication of organic nanoparticles useful as exogenous fluorescent agents for in vitro studies using fluorescent microscopy. This is the first time in the literature that the use of organic nanoparticles fabricated by laser ablation for bioimaging applications is reported.

Perspectives

Due to their attractive properties, including small size, high brightness, monodispersity and low photobleaching, organic fluorescent nanoparticles represent a highly attractive platform for bioimaging. Despite their great potential and promising future as novel fluorescent probes in bioimaging, further improvement of O-NPs still faces many challenges. First, progress in the design and development of (1) better fluorophores with high quantum yield and TPA properties, (2) better synthesis routes for different O-NPs with good target specifity are needed; (3) non-toxicity; (4) both the excitation light and fluorescent emission in the spectral range which is favorable for the penetration of light through thick tissues; (5) efficient and stable fluorescence signal.

Second, O-NPs should be simultaneously functionalized with other properties in addition to fluorescence. For example, O-NPs can be used as vehicles for delivery of therapeutic agents, obtaining potential clinical uses of such nanoparticles as tumor imaging and photodynamic therapy of cancer in deep tissues. For this, methods should be devised and optimized to achieve functionalized biocompatible nanoparticles for site-specific imaging and therapeutics. With the development of suitable nanoparticles, we might suggest a novel approach promising and might represent a new direction for treatment of cancer through nanotechnology in the near future.

Third, O-NPs in other fields, such as biological recognition, delivery, chemical sensors and fiber optic modal interferometers (using O-NPs as active shell) also can be explored.

Product research

1. Two-photon excited fluorescence of silica nanoparticles loaded with a fluorene-based monomer and its cross-conjugated polymer: their application to cell imaging. **Laura Aparicio-Ixta**, Gabriel Ramos-Ortiz, Juan L. Pichardo-Molina, José Luis Maldonado, Mario Rodríguez, Víctor M. Tellez-Lopez, Daniel Martinez-Fong, Mikhail G. Zolotukhin, Serguei Fomine, Marco. A. Meneses-Nava and Oracio Barbosa-García. *Nanoscale*, **4**(24), 7751-7759, 2012.

2. Two-photon imaging of a cellular line using organic fluorescent nanoparticles synthesized by laser ablation. **Laura Aparicio-Ixta**, J. E. Alba-Rosales, Gabriel Ramos-Ortiz, Mario Rodríguez, Juan L. Pichardo-Molina, Gerardo Gutierrez-Juarez, Myrna Sabanero-Lopez, Liss Flores Villavicencio, Rosa Santillan, Víctor M. Tellez-Lopez, Daniel Martínez-Fong. Part. Part. Syst. Charact. In press.

3. Chapter 2. Organic Nanomaterials with Two-Photon Absorption Properties for Biomedical Applications. **Laura Aparicio-Ixta**, Mario Rodríguez and Gabriel Ramos-Ortiz. © Springer Science+Business Media Dordrecht 2016. O. Shulika and I. Sukhoivanov (eds.), *Contemporary Optoelectronics, Springer Series in Optical Sciences* 199, DOI 10.1007/978-94-017-7315-7_2.

4. Synthesis, chemical–optical characterization and solvent interaction effect of novel fluorene-chromophores with D–A–D structure. Jesús Rodríguez-Romero, **Laura Aparicio-Ixta,** Mario Rodríguez, Gabriel Ramos-Ortiz, José Luis Maldonado, Arturo Jiménez-Sánchez, Norberto Farfán, Rosa Santillan. *Dyes and Pigments*, **98**(1), 31-41, 2013.

5. Synthesis and chemical-optical characterization of novel two-photon fluorescent borinates derived from Schiff bases. Cristina C. Jiménez, Norberto Farfán, Margarita Romero-Avila, Mario Rodríguez, **Laura Aparicio-Ixta**, Gabriel Ramos-Ortiz, José Luis Maldonado, Rosa Santillan, Nancy E. Magaña-Vergara, Ma. Eugenia Ochoa. *Journal of organometallic chemistry*, **755**, 33-40, 2014.

6. Red Emissive Biocompatible Nanoparticles from Tetraphenylethene-Decorated BODIPY Luminogens for Two-Photon Excited Fluorescence Cellular Imaging and Mouse Brain Blood Vascular Visualization. Zujin Zhao, Bin Chen, Junlong Geng, Zhengfeng Chang, **Laura Aparicio-Ixta**, Han Nie, Chi Ching Goh, Lai Guan Ng, Anjun Qin, Gabriel Ramos-Ortiz, Bin Liu,and Ben Zhong Tang. *Part. Part. Syst. Charact.*, **31**(4), 481-491, 2014.

7. Silole-based Red Fluorescent Organic Dots for Bright Two-Photon Fluorescence in vitro Cell and in vivo Blood Vessel Imaging. Chen B., Feng G., He B., Goh C., Xu S., Ramos-Ortiz G., **Aparicio-Ixta L.**, Zhou J., Ng L., Zhao Z., Liu B. and Tang B. Z.

doi:10.1002/smll.201502822. Article first published online: 23 December 2015. Our contribution in this manuscript was not included in this thesis.

8. Modal interferometer based on redistributed cladding-modes coupling assisted by a single mechanically-induced long-period grating. Karla M. Salas-Alcántara, **Laura Aparicio-Ixta**, Ismael Torres-Gómez, Mario Rodríguez, Gabriel Ramos-Ortiz, Rafael Espinosa-Luna. Manuscript in process and our contribution was not included in this thesis.

References

1. Ohulchanskyy T. Y., Roy I., Yong K. T., Pudavar H. E., *WIREs Nanomed. Nanobiotechnol.*, **2**(2), 162–175 (2010).

2. Denk W., Strickler J. H., Webb W. W., *Science*, **248**(6), 73–76 (1990).

3. So P. T. C., Dong C. Y., Masters B. R., Berland K. M., *Annu. Rev. Biomed. Eng*., **2**, 399–429 (2000).

4. Sharma P., Brown S., Walter G., Santra S., Moudgil B., *Adv. Colloid Interface Sci.*, **123-126**, 471–485 (2006).

5. Hermann J. P., Ducuing J., *Opt. Commun*., **6**(2), 101–105 (1972).

6. Makarov N. S., Drobizhev M., Rebane A., *Opt. Express*, **16**(6), 4029–4047 (2008).

7. http://www.drbio.cornell.edu/cross_sections.html

8. Svoboda K., Yasuda R., *Neuron*, **50**, 823–839 (2006).

9. Albota M., Beljonne D., Bredas J. L., Ehrlich J. E., Fu J. Y., Heikal A. A., Hess S. E., Kogej T., Levin M. D., Marder S. R., McCord-Maughon D., Perry J. W., Röckel H., Rumi M., Subramaniam G., Webb W. W., Wu X. L., Xu C. *Science*, **281**(5383), 1653–1656 (1998).

10. Agasti S. S., Rana S., Park M. H., Kim C. You C. C., Rotello V., *Adv. Drug Delivery Rev.*, **62**(3), 316–328 (2010).

11. Kim H. M., Cho B. R., *Chem. Commun.*, 2, 153–164 (2009).

12. He G. S., Tan L. S., Zheng Q., Prasad P. N., *Chem. Rev.*, **108**(4), 1245–1330 (2008).

13. Chan W. C. W., Nie S. M., *Science*, **281**(5385) 2016–2018 (1998).

14. Goldman E. R., Anderson G. P., Tran P. T., Mattoussi H., Charles P. T., Mauro J. M., *Anal. Chem.*, **74**(4), 841–847, (2002).

15. Dubertret B., Skourides P., Norris D. J., Noireaux V., Brivanlou A. H., Libchaber A., *Science*, **298**(5599), 1759 –1962 (2002).

16. Gerion D., Pinaud F., Williams S. C., Parak W. J., Zanchet D., Weiss S., Alivisatos A. P., *J. Phys. Chem. B*, **105**(37) 8861–8871 (2001).

17. Ruedas-Rama M. J., Walters J. D., Orte A., Hall E. A. H., *Analytica Chimica Acta,* 751, 1–23 (2012).

18. Wang H. F., Huff T. B., Zweifel D. A., He W., Low P. S., Wei A., Cheng J. X. *Proc Nat Acad Sci USA*, **102**(44), 15752–15756 (2005).

19. Park J., Estrada A., Sharp K., Sang K., Schwartz J. A., Smith D. K., Coleman C., Payne J. D., Korgel B. A., Dunn A. K., Tunnell J. W. *Opt. Express*, **16**(3), 1590–1599 (2008).

20. Mengjun Chen, Meizhen Yin, *Prog. Polym. Sci.* **39**(2), 365–395 (2014).

21. Woo H. Y., Korystov D., Mikhailovsky A., Nguyen T.-Q, Bazan G. C., *J. Am. Chem. Soc.*, **127**, 13794–13795 (2005).

22. a) Hong Y., Lam J. W. Y., Tang B. Z., *Chem. Soc. Rev.*, **40**(11), 5361–5388 (2011); b) Zhang X., Zhang X., Tao L., Chi Z., Xu J., Wei Y., *J. Mater. Chem. B*, **2**(28), 4398–4414 (2014); c) Tang F., Wang C., Wang J., Wang X., Li L., *ACS Appl. Mater. Interfaces*, **6**(20), 18337−18343 (2014).

23. Liu J., Lam J. W. Y., Tang B. Z., *J. Inorg. Organomet. Polym.*, **19**(3), 249–285 (2009).

24. Anjun Qin, Jacky W. Y. Lam, Ben Zhong Tang, *Prog. Polym. Sci.* , **37**(1), 182– 209 (2012).

25. Santra S., Zhang P., Wang K., Tapec R., Tan W., *Anal. Chem.* **73**(20), 4988–4993 (2001).

26. Ow H., Larson D. R., Srivastava M., Baird B. A., Webb W. W., Wiesner U., *Nano Lett.* **5**(1) 113–117 (2005).

27. Shi H., He X., Wang K., Yuan Y., Deng K., Chen J., Tan W., *Nanomed. Nanotechnol. Biol. Med.* **3**(4) 266–272 (2007).

28. Kumar R., Roy I., Ohulchanskyy T. Y., Goswami L. N., Bonoiu A. C., Bergey E. J., Tramposch K. M., Maitra A., Prasad P. N., *ACS Nano*, **2**(3) 449–456 (2008).

29. Ehrlich J. E., Wu X. L., Lee I.-Y. S., Hu Z.-Y., Röckel H., Marder S. R. and Perry J. W., *Opt. Lett.*, **22**(24), 1843–1845 (1997).

30. Wei P., Tan O. F., Zhu Y. and Duan G. H., *Appl. Opt.*, **46**(18), 3694–3699 (2007).

31. Makarov N. S., Rebane A., Drobizhev M., Wolleb H. and Spahni H., *J. Opt. Soc. Am. B*, **24**(8), 1874–1885 (2007).

32. a) Gary-Bobo M., Mir Y., Rouxel C., Brevet D., Basile I., Maynadier M., Vaillant O, Mongin O., Blanchard-Desce M., Morère A., Garcia M., Durand J. O., Raehm L., *Angew.*

Chem., **123**(48), 11627–11631 (2011); b) Kim S., Ohulchanskyy T. Y., Pudavar H. E., Pandey R. K., Prasad P. N., *J. Am. Chem. Soc.*,**129**(9), 2669–2675 (2007); c) Khurana M., Collins H. A., Karotki A., Anderson H. L., Cramb D. T., Wilson B. C., *Photochem. Photobiol.*, **83**(6) 1441–1448 (2007).

33. Przhonska O. V., Webster S., Padilha L. A., Hu H., Kachkovski A. D., Hagan D. J., and Van Stryland E. W., *Springer Series on Fluorescence*, **8**, 105–147 (2010).

34. Fundamentals of Light Microscopy and Electronic Imaging, Second Edition. Douglas B. Murphy and Michael W. Davidson. © 2013 Wiley-Blackwell. Published 2013 by John Wiley & Sons, Inc.

35. Rumi M. C., Perry J.W., *Adv. Opt. Photon.*, **2**(4), 451–518 (2010).

36. a) Mello J. C., Wittmann F., Friend R. H., *Adv. Mater.* **9**(3), 230–232 (1997); b) Wu W. C., Chen C. Y., Tian Y. Q. Jang S. H. Hong Y. N. Liu Y. Hu R. R., Tang B. Z., Lee Y. T., Chen C. T., Chen W. C., Jen A. K. Y., *Adv. Funct. Mater.*, **20**(9), 1413–1423 (2010).

37. Yao S., Belfield K. D., *Eur. J. Org. Chem.*, **2012**(17) 3199–3217 (2012).

38. Principles of Fluorescence Spectroscopy Third Edition, Joseph R. Lakowicz University of Maryland School of Medicine, Baltimore, Maryland, USA.

39. Diaspro A., Chirico G., Usai C., Ramoino P., Dobrucki J., Handbook of Biological Confocal Microscopy, Third Edition, edited by James B. Pawley, Springer Science+Business Media, LLC, New York, 2006.

40. a) Sheik-Bahae M., Said A. A., Wei T. H., Hagan D. J. Van Stryland E. W. Sensitive Measurement of Optical Nonlinearities Using a Single Beam, *IEEE LEOS NEWSLETTER*; Special 30th Anniversary Feature, **21**(1), 17–26 (2007); b) Antonov L., Kamada K., Ohta K., *Appl. Spectrosc.*, **56**(11), 1508–1511 (2002); c) Kamada K., Ohta K., Iwase Y., Kondo K., *Chem. Phys. Lett.*, **372**(3-4), 386–393 (2003).

41. Xu C., Webb W. W., *J. Opt. Soc. Am. B.*,**13**(3) 481–491 (1996).

42. a) Taouri A., Derbal H., Nunzi J. M., Mountasser, R., Sylla, M., *J. Optoelectronic Adv. Mater.*, **11**(11), 1696–1703(2009). b) Bindhu C. V., Harilal S. S., Nampoori V. P. N., Vallabhan C. P. G., *PRAMANA-J. Phys.*, **52**(4), 435–442 (1999).

43. Bindhu C. V., Harilal S. S., Issac R. C., Varier G. K., Nampoori V. P. N., Vallabhan C. P. G., *PRAMANA-J. Phys*., **44**(3), 231–235 (1995).

44. Pawlicki M., Collins H. A., Denning R. G., Anderson H. L., *Angew. Chem. Int. Ed*., **48**(18), 3244–3266 (2009).

45. Wang X., Nguyen D. M., Yanez C. O., Rodriguez L., Ahn H. Y., Bondar M. V., Belfield K. D., *J. Am. Chem. Soc.*, **132**(35), 12237–12239 (2010).

46. Rumi M., Ehrlich J. E., Heikal A. A., Perry J. W., Barlow S., Hu Z., McCord-Maughon D., Parker T. C., Röckel H., Thayumanavan S., Marder S. R., Beljonne D., Brédas J. L., *J. Am. Chem. Soc.*,**122**(39), 9500–9510 (2000).

47. Reinhardt B. A., Brott L. L., Clarson S. J., Dillard A. G., Bhatt J. C., Kannan R., Yuan L., He G. S., Prasad P. N., *Chem. Mater.*,**10**(7), 1863–1874 (1998).

48. Kim S., Pudavar H. E., Bonoiu A., Prasad P. N., *Adv. Mater.*, **19**(22), 3791–3795 (2007).

49. Wang X., Yao S., Ahn H.-Y., Zhang Y., Bondar M. V., Torres J. A., Belfield K. D., *Biomed. Opt. Express*, **1(**2), 453–462 (2010).

50. Tan Y., Zhang Q., Yu J., Zhao X., Tian Y., Cui Y., Hao X., Yang Y., Qian G., *Dyes Pigm.*, **97**(1), 58–64 (2013).

51. Huang C., Peng X., Yi D., Qu J., Niu H., *Sens. Actuators B Chem.*, **182**, 521–529 (2013).

52. Morales A. R., Luchita G., Yanez C. O., Bondar M. V., Przhonska O. V., Belfield K. D., *Org. Biomol. Chem.*, **8**(11), 2600–2608 (2010).

53. Ahn T.K., Kim K.S., Kim D.Y., Noh S.B., Aratani N., Ikeda C., Osuka A., Kim D., *J. Am. Chem. Soc.*, **128**(5), 1700–1704 (2006).

54. Raymond J. E., Bhaskar A., Goodson III T., Makiuchi N., Ogawa K., Kobuke Y., *J. Am. Chem. Soc.*, **130**(51), 17212–17213 (2008).

55. Velusamy M., Shen J. Y., Lin J. T., Lin Y. C., Hsieh C. C., Lai C. H., Lai C. W., Ho M. L., Chen Y. C., Chou P. T., Hsia J. K., *Adv. Funct. Mater.*, **19**(15), 2388–2397 (2009).

56. Wu C., Szymanski C., Cain Z., McNeill J., *J. Am. Chem. Soc.*, **129**(43), 12904–12905 (2007).

57. Zheng Q., Xu G., Prasad P. N., *Chem. Eur. J.*, **14**(19), 5812–5819 (2008).

58. Lin T. C., Lee Y. H., Huang B. R., Hu C. L., Li Y. K., *Tetrahedron*, **68**(25)**,** 4935–4949 (2012).

59. Tian Y., Chen C. Y., Cheng Y. J., Young A. C., Tucker N. M., Jen A. K. Y., *Adv. Funct. Mater.*, **17**(10), 1691–1697 (2007).

60. Li K., Jiang Y., Ding D., Zhang X., Liu Y., Hua J., Feng S. S., Liu B., *Chem. Commun.*, **47**(26), 7323–7325 (2011).

61. Castro-Beltran R., Ramos-Ortiz G., Jim C.K.W., Maldonado J. L., Häußler M., Peralta-Dominguez D., Meneses-Nava M.A., Barbosa-Garcia O., Tang B. Z., *Appl. Phys. B*, **97,** 489–496 (2009).

62. Wan Y., Yan L., Zhao Z., Ma X., Guo Q., Jia M., Lu P., Ramos-Ortiz G., Maldonado J. L., Rodríguez M., Xia A., *J. Phys. Chem. B*, **114**, 11737–11745 (2010).

63. Drobizhev M., Karotki A., Rebane A., *Opt. Lett.*, **26**(14), 1081–1083(2001).

64. Abdul N. A., McDaniel W., Bardon K., Srinivasan S., Vickerman V., So P. T. C., Ho J., *Adv. Mater.*, **21**, 3492–3496 (2009).

65. Narayanan A., Varnavski O., Mongin O., Majoral J. P., Blanchard-Desce M.Goodson IIIT, *Nanotechnology*, **19**,115502, 6pp (2008).

66. Nicoud J. F., Bolze F., Sun X. H., Hayek A., Baldeck P., *Inorg. Chem.*, **50**(10), 4272–4278 (2011).

67. a) Kasai H., Nalwa H. S., Oikawa H., Okada S., Matsuda H., Minami N., Kakuta A., Ono K., Mukoh A., Nakanishi H., Jpn. *J. Appl. Phys.* **31,** Part 2 No. 8A, L1132–L1134 (1992); b) Kasai H., Kamatani H., Okada S., Oikawa H., Matsuda H., Nakanishi H., *Jpn. J. Appl. Phys.* 35:L221–L223 (1996); c) Kasai H., Kamatani H., Yoshikawa Y., Okada S., Oikawa H., Watanabe A., Itoh O., Nakanishi H., *Chem. Lett.* **26**(11), 1181–1182 (1997).

68. a) Yao J. H., Mya K. Y., Shen L., He B. P., Li L., Li Z. H., Chen Z. K., Li X. and Loh K. P., *Macromolecules*, **41**(4), 1438–1443 (2008); b) L. Zhu, C. Yang, Jingui Qin, *Chem. Commun.*, **47**, 6303–6305 (2008).

69. Enseki T., Yao H., *Chem. Lett*., **41**(10), 1119–1121 (2012).

70. a) Texter J., *J. Disp. Sci. Technol.*, **22**(6), 499–527 (2001); b) Zhang H., Wang D., Butler R., Campbell N. L., Long J., Tan B., Duncalf D. J., Foster A. J., Hopkinson A., Taylor D., Angus D., Cooper A. I., Rannard S. P., *Nat. Nanotechnol.*, **3**(8), 506–511 (2008).

71. Cao Z. H., Ziener U., *Nanoscale*, **5**(21), 10093–10107 (2013).

72. Asahi T., Sugiyama T., and Masuhara H., *Acc. Chem. Res.*, **41**(12), 1790–1798 (2008).

73. a) Li Y., Liu J., Liu B., Tomczak N., Nanoscale, **4**, 5694–5702 (2012); b) Zhang X., Zhang X., Yang B., Zhang Y., Wei Y., *ACS Appl. Mater. Interfaces*, **6**, 600−3606 (2014).

74. a) Baba K., Kasai H., Nishida K., Nakanishi H., (2010). Organic Nanocrystals for Nanomedicine and Biophotonics, Nanocrystals, Yoshitake Masuda (Ed.), ISBN: 978-953-307-126-8, InTech; b) Baba K., Kasai H., Masuhara A., Oikawa H., and Nakanishi H., *Jpn. J. Appl. Phys.* **48**(11), 117002 (2009).

75. Masuhara H., Bull. *Chem. Soc. Jpn.* **86**(7), 755–783 (2013).

76. Tamaki Y., Asahi T. and Masuhara H., J. Phys. Chem. A, **106**(10), 2135–2139 (2002).

77. Liu P., Cui H., Wang C. X., Yang G. W., *Phys. Chem. Chem. Phys.*, **12**(16), 3942–3952 (2010).

78. Amendola V., Meneghetti M., *Phys. Chem. Chem. Phys.*, **15**(9), 3027–3046 (2013).

79. Chung H. R., Kwon E., Oikawa H., Kasai H. and Nakanishi H., *J. Cryst. Growth*, **294**(2), 459–463 (2006).

80. Nakanishi H., Oikawa H., Reprecipitation Method for Organic Nanocrystals, Single Organic Nanoparticles© Springer-Verlag Berlin Heidelberg 2003, 17–31.

81. Yang S., Lu D., Tian L., He F., Chen G., Shen F., Xu H., Ma Y., Nanoscale, **3**(5) 2261–2267 (2011).

82. Elaboudi I., Lazare S., Belin C., Talaga D. and Labrugère C., *Appl. Phys. A*, **93**(4), 827–831 (2008).

83. Yang G. W., *Prog. Mater Sci.*, **52**(4) 648–698 (2007).

84. Zhao Y. S., Yang W., Yao J., *Phys. Chem. Chem. Phys.*, **8**(28), 3300–3303 (2006).

85. Pecher J., Mecking S., *Chem. Rev.*, **110**(10), 6260–6279 (2010).

86. Xiao D., Lu X., Yang W., Fu H., Shuai Z., Fang Y., Yao J., *J. Am. Chem. Soc*., **125**(22), 6740–6745 (2003).

87. Bagwe R. P., Yang C., Hilliard L. R. and Tan W., *Langmuir*, **20**(19), 8336–8342 (2004).

88. Jin Y., Lohstreter S., Pierce D. T., Parisien J., Wu M., Hall C. and Zhao J. X., *Chem. Mater*., **20**(13), 4411–4419 (2008).

89. Tan D., Ma Z., Xu B., Dai Y., Ma G., He M., Jin Z., Qiu J., *Phys. Chem. Chem. Phys.*, **13**(45), 20255–20261 (2011).

90. Nakamura M., Shono M., Ishimura K., *Anal. Chem.*, **79**(17), 6507–6514 (2007).

91. Miletto I., Gilardino A., Zamburlin P., Dalmazzo S., Lovisolo D., Caputo G., Viscardi G., Martra G., *Dyes Pigm.*, **84**(1), 121–127 (2010).

92. Hobley J., Nakamori T, Kajimoto S., Kasuya M., Hatanaka K., Fukumura H., Nishio S., *J. Photochem. Photobiol., A: Chem.*, **189** (1), 105–113 (2007).

93. Ujiiye-Ishii K., Kwon E., Kasai H., Nakanishi H., Oikawa H., *Cryst. Growth Des.*, **8**(2), 369–371, 2008.

94. Chandran S. P., Hotha S. and Prasad B. L. V., *Curr. Sci.*, **95**(9), 1327–1333 (2008).

95. Bagwe R. P., Hilliard L. R. and Tan W., *Langmuir*, **22**(9), 4357–4362 (2006).

96. Metin C. O., Lake L. W., Miranda C. R., Nguyen Q. P., *J. Nanopart. Res.*, **13**(2), 839–850 (2011).

97. Li B., Kawakami T., Hiramatsu M., *Appl. Surf. Sci.*, **210**(3-4), 171–176 (2003).

98. Zeng H., Du X. W., Singh S. C., Kulinich S. A., Yang S., He J., Cai W., *Adv. Funct. Mater.*, **22**(7), 1333–1353 (2012).

99. Zhang X., Zhang X., Wang S., Liu M., Tao L., Wei Y., *Nanoscale*, **5**(1), 147–150 (2013).

100. Liu D., He X., Wang K., He C., Shi H., Jian L., *Bioconjug. Chem.*, **21**(9), 1673–1684 (2010).

101. F. Chen, M. Chen, C. Yang, J. Liu, N. Luo, G. Yang, D. Chen, L. Li, *Phys. Chem. Chem. Phys.* **2015**, *17*, 1189.

102. Aparicio-Ixta L., Ramos-Ortiz G., Pichardo-Molina J. L., Maldonado J. L., Rodríguez M., Tellez-Lopez V. M., Martinez-Fong D., Zolotukhin M. G., Fomine S., Meneses-Nava M. A. and Barbosa-García O., *Nanoscale*, **4**(24), 7751–7759 (2012).

103. Song X., Li F., Ma J., Jia N., Xu J. and Shen H., *J. Fluoresc.*, **21**(3), 1205–1212 (2011).

104. Jin Y., Kannan S., Wu M. and Zhao J. X., *Chem. Res. Toxicol.*, **20**(8), 1126–1133 (2007).

105. Li K., Liu B., *J. Mater. Chem.*, **22**(4), 1257–1264 (2012).

106. a) Wu W. B., Liu C., Wang M. L., Huang W., Zhou S. R., Jiang W., Sun Y. M., Cui Y. P. and Xu C. X., *J. Solid State Chem.*, **182**(4), 862–868 (2009); b) Ganguli A. K., Ganguly A., Vaidya S., *Chem. Soc. Rev.*, **39**(2), 474–485 (2010).

107. Sugiyma T., Asahi T., Takeuchi H., Masuhara H., *Jpn. J. Appl. Phys.*, **45**(1B), 384–388 (2006).

108. Tamaki Y., Asahi T., Masuhara H. *Appl. Surf. Sci.*, **168**(1-4), 85–89 (2000).

109. Baba K., Kasai H., Nishida K. Nakanishi H. (2011). Functional Organic Nanocrystals, Nanocrystal, Dr. Yoshitake Masuda (Ed.), ISBN: 978-953-307-199-2, InTech, DOI:10.5772/16948.

110. Rodríguez-Romero J., Aparicio-Ixta L., Rodríguez M., Ramos-Ortíz G., Maldonado J. L., Jiménez-Sánchez A., Farfán N., Santillan R., *Dyes Pigm.*, **98**(1), 31–41 (2013).

111. Kim S., Zheng Q., He G. S., Bharali D. J., Pudavar H. E., Baev A., Prasad P. N., *Adv. Funct. Mater*., **16**(18), 2317–2323 (2006).

112. Zheng Q., Ohulchanskyy T. Y., Sahoo Y., Prasad P. N., *J. Phys. Chem. C,* **111**(45), 16846–16851 (2007).

113. Margulis-Goshen K., Magdassi S., *Curr. Opin. Colloid Interface Sci.,* **17**(5), 290–296 (2012).

114. López-Quintela M. A., *Curr. Opin. Colloid Interface Sci.*, **8**(2), 137–144 (2003).

115. Bioconjugate techniques 2nd Edition, Greg T. Hermanson, 2008.

116. a) Zhang Z., Jia J., Lai Y., Ma Y., Weng J., Sun L., *Bioorg. Med. Chem.*, **18**(15), 5528–5534 (2010); b) Ai J., Xu Y., Li D., Liu Z., Wang E., *Talanta*, **101**, 32–37 (2012).

117. Xu L., Pirollo K. F., Chang E. H., *J. Control. Release*, **74**(1-3), 115–128 (2001).

118. Kohler N., Sun C., Wang J., Jhang M., *Langmuir*, **21**(19), 8858–8864 (2005).

119. Huang P., Bao L., Zhang C., Lin J., Luo T., Yang D., He M., Li Z., Gao G., Gao B., Fu S., Cui D., *Biomaterials*, **32**(36), 9796-9809 (2011).

120. Shena Z., Li Y., Kohama K., Oneill B., Bi J., *Pharmacol. Res.*, **63**(1), 51–58 (2011).

121. Lin J. J., Chen J. S., Huang S. J., Ko J. H., Wang Y. M., Chen T. L., Wang L. F., *Biomaterials*, **30**(28) 5114–5124 (2009).

122. Lebret V., Raehm L., Durand J. O., Smaïhi M., Werts M. H. V., Blanchard-Desce M., Méthy-Gonnod D., Dubernet C., *J. Sol-Gel Sci. Technol.*, **48**(1-2), 32–39 (2008).

123. Hayek A., Bolze F., Bourgogne C., Baldeck P. L., Didier P., Arntz Y., Mely Y., Nicoud J. F., *Inorg. Chem.*, **48**(19), 9112–9119 (2009).

124. Jadhav T., Maragani R., Misra R., Sreeramulu V., Narayana Rao D., Mobin S. M., *Dalton Trans.*, **42**(13), 4340–4342 (2013).

125. a) Howes P., Green M., Levitt J., Suhling K., Hughes M., *J. Am. Chem. Soc.*, **132**(11), 3989–3996 (2010).

126. Wu C., Szymanski C., McNeill J., *Langmuir*, **22**(7), 2956–2960 (2006).

127. Frath D., Azizi S., Ulrich G., Retailleau P., Ziessel R., *Org. Lett.*, **13**(13), 3414–3417 (2011).

128. Li D., Zhang H., Wang C., Huang S., Guo J., Wang Y., *J. Mater. Chem.* **22**(10), 4319–4328 (2012).

129. a) Boens N., Leen V., Dehaen W., *Chem. Soc. Rev.*, **41**(24), 1130–1172 (2012); b) Ulrich G., Ziessel R., Harriman A., *Angew. Chem. Int. Ed.*, **47**(7), 1184–1201 (2008); c) Hayashi Y., Obata N., Tamaru M., Yamaguchi S., Matsuo Y., Saeki A., S. Seki, Y. Kureishi, S. Saito, S. Yamaguchi, H. Shinokubo, *Org. Lett.*, **14**(3), 866–869 (2012); d) Bura T., Ziessel R., *Org. Lett.*, 13(12), 3072–3075 (2011); e) Kowada T., Yamaguchi S., Ohe K., *Org. Lett.*, **12**(2), 296–299 (2010); f) Umezawa K., Matsui A., Nakamura Y., Citterio D., Suzuki K., Bright, *Chem. Eur. J.*, **15**(5), 1096–1106 (2009); g) Zhu S., Zhang J., Vegesna G., Luo F. T., Green S. A., Liu H., *Org. Lett.*, **13**(3), 438–441 (2011).

130. a) Zhang Y., Li J., Tang B. Z., Wong K. S., *J. Phys. Chem. C*, **118**, 26981−26986 (2014). b) Hu R., Maldonado J. L., Rodriguez M., Deng C., Jim C. K. W., Lam J. W. Y., Yuen M. M. F, Ramos-Ortiz G., Tang B. Z., *J. Mater. Chem.*, **22**, 232−240 (2012).

131. a) Zhao Z., Lam J. W. Y., Tang B. Z., *J. Mater. Chem.*, **22**, 23726–23740 (2012). b) Shen X. Y., Wang Y. J., Zhao E., Yuan W. Z., Liu Y., Lu P., Qin A., Ma Y., Sun J. Z., Tang B. Z., *J. Phys. Chem. C*, **117**, 7334−7347 (2013).

132. Zhang D., Wang Y., Xiao Y., Qian S., Qian X., *Tetrahedron*, **65**(39), 8099–8103 (2009).

133. a) Hong Y., Lam J. W. Y., Tang B. Z., *Chem. Commun.*, **29**, 4332–4353 (2009); b) Hong Y., Lam J. W. Y., Tang B. Z., *Chem. Soc. Rev.*, **40**(11), 5361–5388 (2011); c) Zhao Z., Lam J. W. Y., Tang B. Z., *Curr. Org. Chem.*, **14**(18), 2109–2132 (2010).

134. a) Zhao Z., Lu P., Lam J. W. Y., Wang Z., Chan C. Y. K., H. H.Y. Sung, I. D. Williams, Y. Ma, B. Z. Tang, *Chem. Sci.*, **2**(4),672–675 (2011); b) Zhao Z., Chan C. Y. K., Chen S., Deng C., Lam J. W. Y., Jim C. K. W., Hong Y., Lu P., Chang Z., Chen X., Lu P., Kwok H. S., Qiu H., Tang B. Z., *J. Mater. Chem.*, **22**(10), 4527–4534 (2012). c) Z. Zhao, S. Chen, C. Deng, J. W. Y. Lam, C. Y. K. Chan, P. Lu, Z. Wang, B. Hu, X. Chen, P. Lu, H. S. Kwok, Y. Ma, H. Qiu, B. Z. Tang, *J. Mater. Chem.*, **21**(29), 10949–10956 (2011).

135. Zhang D., Wang Y., Xiao Y., Qian S., Qian X., *Tetrahedron*, **65**(39), 8099–8103 **(**2009).

136. a) Shirota Y., Kageyama H. Chem. Rev. **107**(4) 953**–**1010 (2007). b) Saragi TPI, Spehr T, Siebert A, Fuhrmann-Lieker T, Salbeck J. *Chem. Rev.*, **107**(4), 1011**–**1065 (2007).

137. Belfield K. D., Morales A. R., Kang B. S., Hales J. M., Hagan D. J., Van Stryland E. W., Chapela V. M., Percino J. *Chem. Mater.* **16**(23), 4634–4641 (2004).

138. Thomas III S. W., Joly G. D., Swager T. M. *Chem. Rev.* **107**(4)1339–1386 (2007).

139. Qian J., Gharibi A., He S., *J. Biomed. Opt.*, **14**(1), 014012–014012–6 (2009).

140. Arriagada F. J., Osseo-Asare K., *J. Colloid Interface Sci.*, **170**(1), 8–17 (1995).

141. V. Lebret, L. Raehm, J.-O. Durand, M. Smaïhi, C. Gérardin, N. Nerambourg, M. H. V. Werts, M. Blanchard-Desce, *Chem. Mater.*, **20**(6), 2174–2183 (2008).

142. Howes P., Green M., Levitt J., Suhling K., Hughes M., *J. Am. Chem. Soc.*, **132**(11), 3989–3996 (2010).

143. Kulkarni A. P., Kong X., Jenekhe S. A., *J. Phys. Chem. B*, 2004, **108**(25), 8689–8701.

144. Andrade C. D., Yanez C. O., Rodriguez L. and Belfield K. D., *J. Org. Chem.*, **75**(12), 3975–3982 (2010).

145. Wu W. C., Chen C. Y., Tian Y., Jang S. H., Hong Y., Liu Y., Hu R., Tang B. Z., Lee Y. T., Chen C. T., Chen W. C., Jen A. K. Y., *Adv. Funct. Mater.*, **20**, 1–11 (2010).

146. Knopp D., Tang D., Niessner R., *Anal. Chim. Acta*, **647**(2), 14–30 (2009).

147. Bae S. W., Tan W., Hong J. I., *Chem. Commun.*, **48**, 2270–2282 (2012).

148. Vivero-Escoto J. L., Huxford-Phillips R. C., Lin W., *Chem Soc. Rev.*, **41**, 2673–2685 (2012).

149. Schulz A., McDonagh C., *So. Matter.*, **8**, 2579–2585, (2012).

150. Chelebaeva E., Raehm L., Durand J.-O., Guari Y., Larionova J., Gu´erin C., Trifonov A., Willinger M., Thangavel K., Lascialfari A., Mongin O., Mir Y. and Blanchard-Desce M., *J. Mater. Chem.*, **20**, 1877–1884 (2010).

151. Tang W., Ke L., Tan L., Lin T., Kietzke T., Chen Z. K., *Macromolecules*, **40**, 6164 – 6171 (2007).

152. T. C. Lin, Y. H. Lee, C. L. Hu, Y. K. Li, Y. J. Huang, *Eur. J. Org. Chem.*, **9**, 1737–1745 (2012).

153. Li X., Zhang X., Li W., Wang Y., Liu T., Zhang B., Yang W., *J. Mater. Chem.*, **21**, 3916–3924 (2011).

154. Cho B. R., Piao M. J., Son K. H., Lee S. H., Yoon S. J., Jeon S. J., Cho M., *Chem. Eur. J.*, **8**(17), 3907–3916 (2002).

155. W. Yao-Chuan, Y. Yong-Li, Z. Hui, H. Nan, F. Miao, Q. Shi-Xiong, C. Yu, *Acta Phys.-Chim. Sin.*, **26**(03), 707–713 (2010).

156. Y. Jiang, Y. Wang, J. Hua, S. Qu, S. Qian, H. Tian, *J. Polym. Sci., Part A: Polym. Chem.*, **47**, 7400–7408 (2009).

157. Varnavski O., Yan X., Mongin O., Blanchard-Desce M., Goodson T., *J. Phys. Chem. C*, **111**(1), 149–162 (2007).

158. Belfield K. D., Yao S., Bondar M. V. *Adv. Polym. Sci.*, **213**, 97–156 (2008).

159. Ma Z., Lu S., Fan Q. L., Qing C. Y., Wang Y. Y., Wang P., Huang, W. *Polymer*, **47**(21), 7382–7390 (2006).

160. Zhou H, Yang L, You W. *Macromolecules*, **45**(2), 607–32 (2012).

161. Kucherak O. A., Didier P., Mély Y., Klymchenko A. S., *J. Phys. Chem. Lett.*, **1**(3) 616–620 (2010).

162. a) Zein S., Delbecq F., Simon D. *Phys. Chem. Chem. Phys.*, **11**(4), 694–702 (2009).
b) Fitilis I., Fakis M., Polyzos I., Giannetas V., Persephonis P., Vellis P., Mikroyannidis, J. *Chem. Phys. Lett*., **447**(4-6), 300–304 (2007).

163. Cheng Y. J., Yang S. H., Hsu C. S. *Chem. Rev.*, **109**(11), 5868–**5**923 (2009).

164. Grimsdale A. C., Chan K. L., Martin R. E., Jokisz P. G., Holmes A. B., *Chem. Rev.*, **109**(3), 897–1091 (2009).

165. Rodrigues P. C., Berlim L. S., Azevedo D., Saavedra N. C., Prasad P. N., Schreiner W. H., Atvars T. D. Z., Akcelrud L., *J. Phys. Chem. A*, **116**(14), 3681−3690 (2012).

166. Lincker F., Heinrich B., Bettignies R., Rannou P., Pécaut J., Grévin B., Pron A., Donnio B., *J. Mater. Chem.*, **21**(14), 5238−5247 (2011).

167. Reichardt C. Solvents and Solvent Effects in Organic Chemistry. 3rd ed. 1 reprint 2004. Wiley–VCH: Weinheim. 2003.

168. Peng Q., Lu Z. Y., Huang Y., Xie M. G., Han S. H., Peng J. B., Cao Y., *Macromolecules*, **37**(2), 260–266 (2004).

169. Luo J., Yang R., Yang W., Cao Y., *Sci. China Chem.*, **53**(3), 576–**5**80 (2010).

170. Park K. K, Tsou L. K., Hamilton A. D., *Synthesis*, **21**, 3617–3620 (2006).

171. Saroja G., Soujanya T., Ramachandram B., Samanta A. *J. Fluoresc.*, **8**(4), 405−410 (1998).

172. Fery–Forgues S., Fayet J. P., Lopez A. *J. Photochem. Photobiol. A: Chem.*, **70**(3), 229−243 (1993).

173. Cheng J. Z., Lin C. C., Chou P. T., Chaskar A., Wong K. T. *Tetrahedron*, **67**(4), 734–739 (2011).

174. Wang Y., Huang J., Zhou H., Ma G., Qian S., Zhu X. H. *Dyes Pigm.*, **92**(1), 573–579 (2011).

175. Kato S. I., Matsumoto T., Shigeiwa M., Gorohmaru H., Maeda S., Ishi-I T., Mataka S. *Chem. Eur. J.*, **12**(8), 2303**–**2317 (2006).

176. Nag A., Goswami D. *J. Photochem. Photobiol. A: Chem.*, **206**(2-3), 188**–**97 (2009).

177. Wang C. K., Zhao K., Su Y., Ren Y., Zhao X., Luo Y., *J. Chem. Phys.*, **119**(2), 1208–1213 (2003).

178. Yan Y., Li B., Liu K., Dong Z., Wang X., Qian S., *J. Phys. Chem. A*, **111**(20), 4188**–**4194 (2007).

179. Alexandre Albanese, Peter S. Tang, Warren C.W. Chan, *Annu. Rev. Biomed. Eng.*, **14**, 1–16 (2012).

180. El-Daly S. A., El-Azim S. A., Elmekawey F. M., Elbaradei B. Y., Shama S. A., Asiri A. M., *Int. J. of Photoenergy*, 458126, p. 10 (2012).

181. Albota M. A., Xu C. and Webb W. W., *Appl. Opt.*, **37**(31), 7352–7356 (1998).

182. S. Nagl, M. Schaeferling, O. S.Wolfbeis, *Microchim. Acta*, **151**, 1 (2005).

183. C. Xu, W. R. Zipfel, *Cold Spring Harb. Protoc.*, **3**, 250 (2015).

Appendix A. Reagents and equipment used to fabrication and characterization of fluorescent materials

All fluorophores (Borinates, BODIPYS, M1, P1 and BT2) used in this dissertation are non commercial and their synthesis were reported elsewhere.[i-iv]

For the fabrication of organic nanoparticles and doped silica nanoparticles the following materials were utilized: deionized water, 1-butanol 99.8%, 1- Sodium bis(2-ethylhexyl)sulfosuccinate (AOT, D201170), N-Methyl-2-pyrrolidinone (NMP, 328634), triethoxyvinylsilane (VTES, 175560), 3-aminopropyltriethoxysilane (APTES, A3648) and 3-(Trihydroxysilyl)propyl methylphosphonate monosodium salt solution (THPMP, 435716), tetrahydrofuran (THF, 401757), hexadecyltrimethyl-ammonium bromide (CTAB) and p-(1,1,3,3-tetramethylbutyl) phenoxypolyoxyethylene glycols (Triton X-100).

For the characterization of BT2 in solution were used Hexane, Toluene, Dioxane, Tetrahydrofuran, Acetone, Acetonitrile and Methanol. All solvents were anhydrous grade and all chemicals for the fabrication of organic nanoparticles also were purchased from Sigma Aldrich. Only 1-butanol was purchased in Karal S.A. de C.V. All chemicals were used without further purification.

For BT2 nanostructures with polyethylene glycol the following PEG's were utilized: **PEG 5000** (O- [2- (3-Mercaptopropionylamino) ethyl] -O'-methylpolyethylene glycol 5000, purchased from Sigma-Aldrich), average molecular weight: 5000 g/mol. **PEG 3400** (PEG Succinimidyl 3400 MW succinimidyl ester, INC NANOCS), average molecular weight: 3400 g/mol. **PEG 2000** (1,2-distearoyl-sn-glycero-3-phosphoethanolamine-N- [methoxy (polyethylene glycol)-2000] (ammonium salt), purchased from Avanti Polar Lipids Inc.), average molecular weight: 2000g/mol.

For the estimation of amino groups on the silica nanoparticles surface were used TNBS, Picrylsulfonic acid solution 5 % (W/V) (P2297, Sigma-Aldrich), HCl and Sodium Dodecyl Sulfate (SDS), BioReagent, suitable for electrophoresis, for molecular biology, ≥98.5% (GC) (L3771, Sigma Aldrich).

For different functionalizations and bioconjugations of fluorescent silica nanoparticles the following materials were used: Succinic anhydride (239690), Sodium acetate, Potassium carbonate, Sodium Phosphate, Acetic Anhydride, ACS Reagent, >=98.0%, *N*-(3-Dimethylaminopropyl)-*N′*-ethylcarbodiimide hydrochloride, (EDC), HEPES Biotechnology Performance Certified, ≥99.5% (titration), cell culture tested (H4034), Glutaraldehyde grade II (G6257), Folic acid ≥97% (F7876), Glycine for electrophoresis, ≥99% (G8898), NHS-PEG-NHS PEG average M_n 3,400 (n ~ 77), NaOH, Transferrin human powder, BioReagent, suitable for cell culture, invitrogen and Biotech CE 100Kd, 16mm. trial kit.

For electrophoresis gel were used Agarose (V3121), Tris Base P/Karal (9131), EDTA, Glacial Acetic Acid, Sodium bicarbonate (5010, Karal).

Cell-culture products and Hoechst 33258 were purchased from GIBCO™ (Invitrogen Corporation, Grand Island, NY). Vecta Shield-DAPI (4',6-diamidino-2-phenylindole), a fluorescent stain that binds strongly to A-T rich regions in DNA was purchased from Vector Laboratories, USA.

The human cervix cancer cell line HeLa ATCC® CCL-2™ and A549 (line derived from lung adenocarcinoma) were used.

UV-visible absorption spectra were obtained with a Perkin Elmer LAMBDA 900, spectrophotometer. The photoluminescence spectra were acquired with an Ocean Optics 4000 spectrometer using a diode laser (375 nm) as an excitation source. Scanning electron microscopy (SEM) was performed in a JEOL JSM-7500F microscope. TPA cross sections of samples were measured through two-photon excited fluorescence (TPEF) technique using a Ti:Sapphire laser (100 fs/pulse, repetition rate of 80 MHz, tunability 740–830 nm). Fluorescence lifetimes were obtained at room temperature by time correlated single photon counting (TCSPC) technique on a Horiba Jobin Yvon TemPro instrument with a nanoLED laser of 455 nm as excitation source.

Finally the cells were imaged through a Leica TCS-SP5 MP two-photon laser scanning microscope (Leica Microsystem, Wetzlar Germany) and Olympus FV1000 microscope.

Appendix B. Synthesis of organic nanoparticles by reprecipitation method

First, 1 mg of organic fluorescent fluorophore was dissolved in 2 mL of THF. Then a small volume of these solutions (typically in the range 0.25–0.8 mL) was injected quickly and under sonication in 8 mL of deionized water or in 8 mL of aqueous solution containing one of the following surfactants: CTAB or Triton X-100. The surfactants were used at the concentrations in the range of 0.08-0.8 mM to achieve high nanoparticles concentration and long stability. THF was then removed by evaporation under vacuum, followed by filtration through membrane filters with 0.2 μm cutoff. The resulting aqueous suspensions of nanoparticle were of high optical quality and without significant light scattering. Figure A1.

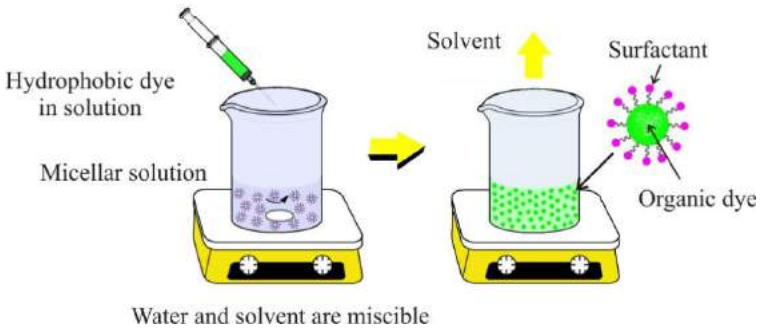

Fig. A1. Reprecipitation method to fabricate organic nanoparticles.

Appendix C. Synthesis of silica nanoparticles doped with organic fluorescent fluorophores

This method was described by X. Wang, J Qian, F. J. Arriagada and coworkers.[49,134,135] The process consists in the preparation of a microemulsion system to synthesize fluorescent silica nanoparticles (FSNPs) in the nonpolar core of Aerosol-OT/1-butanol micelles in water. Micelles were prepared by dissolving either 0.22 g or 0.44g of Aerosol-OT, 300 μL of 1-butanol and 200 μL of NMP in 10 mL of deionized water by magnetic stirring. NMP was used as a hydrophilic solvent for the organic fluorescent fluorophores and exhibits unlimited water miscibility. Then, 200 μL of the fluorophore dissolved in NMP at the concentration of 10 mM and 0.1 mM, respectively, was added to the micellar solution under constant magnetic stirring. Half an hour later, 100 μL of neat VTES was added to the micellar system, and the resulting solution was stirred for about 1 hr. Next, the doped silica nanoparticles were precipitated by adding 20 μL of APTES or THPMP and stirring the

solution for 20 hrs at room temperature. The use of two different precursors such as APTES or THPMP allowed us to modify the surface of FSNPs with amine groups (NH_2) or methyl phosphonate groups ($MePO_2^-$), respectively. To remove surfactants, co-surfactants, non-encapsulated fluorophore and residues of unreacted precursors, the suspension was dialyzed against deionized water in a 8-10 kDa cutoff cellulose membrane Float-A-Lyzer G2 for 72 hrs. Aqueous suspension of FSNPs was obtained at different concentrations and special care was taken to eliminate big particles by filtering the suspensions with a membrane filter with 0.2 μm cutoff. The resultant samples exhibited high colloidal stability.

Appendix D. Fabrication of organic nanoparticles by laser ablation

To fabricate O-NPs through LA method (**NPs-LA**), the first step was to grow single crystals of the BT2 fluorophore. A saturated solution of the compound (in hexane) was covered and kept undisturbed for slow evaporation of the solvent at room temperature. After few days crystals in the form of needles were obtained. These crystals of BT2 were pulverized mechanically to obtain micrometer-sized crystals of which 2 mg were suspended in 5 mL of milli-Q water containing the surfactant cetyltrimethylammonium bromide (CTAB) at the concentration of 0.8 × 10−3 M. Such microcrystals (suspended in the water-CTAB solution using continuous magnetic stirring) were exposed to an intense laser beam of femtosecond pulses (800 nm wavelength, 650 μJ/pulse, 60 fs pulse width, 1 kHz repetition rate) provided by a Ti:Sapphire Regenerative Amplifier from Coherent Inc. Without any beam focusing (beam waist of ≈5 mm), the laser ablated the microcrystals during 60 min and the ejected material was trapped by the water–CTAB solution and stabilized as fluorescent O-NPs. Samples were filtered using membrane filters with 0.2 μm cutoff. Figure A2.

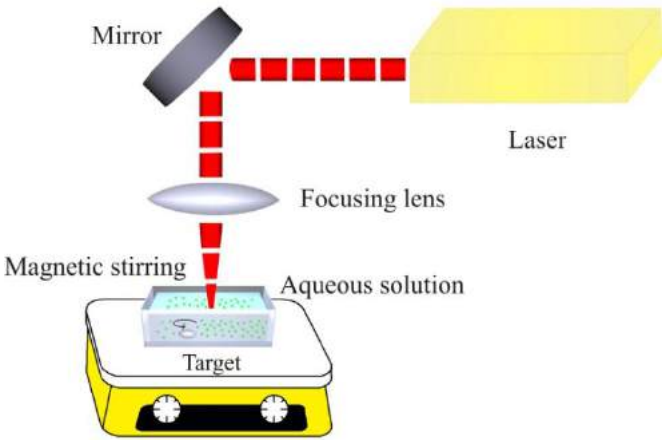

Fig. A2. Laser ablation method to fabricate organic nanoparticles.

Appendix E. Surface modification of amino-functionalized SNPs with folic acid/Transferrin

For an efficient bioconjugation, first it is necessary to obtain a quantitative estimation of amino groups of the FSNPs to use the appropriate amount of crosslinking agent and provide another reactive group at the other end to couple with the biomolecule. 2,4,6-Trinitrobenzene Sulfonic Acid (TNBS) is used for this purpose. It reacts with amine-containing compound and a highly chromogenic product is generated whose absorbance is readily measured at 335nm. For quantitation of amines, the results were compared with a standard curve generated with an amine-containing the compound prepared at various concentrations.

In the first method to conjugate silica nanoparticles with folic acid, which is called S1, the following procedure was used: To 2 mL of suspension of FSNPs with amine groups in the surface dispersed in sodium phosphate (0.1M, pH~7.3), 200 μL of 0.1 M EDC solution was added, and the mixture was stirred at room temperature for 30 min. Then 2.2 mg of folic acid diluted in a sodium phosphate solution was added, and the reaction between folic acid and amino groups was allowed to proceed for 12 h. Finally, the suspension obtained was dialyzed against deionized water for 50 h to remove unreacted molecules.[49]

The next method called S2 carried out is similar for bioconjugation of the BT2-SNPs with folic acid or transferrin. To a 2.5 mL of suspension of BT2-SNPs with amine groups in the surface, was added 2.5 mL of HEPES buffer (pH value ~8.0, 40 mM). Next, 121 μL of GA was added to suspension obtained, and we let the reactions between GA and amino groups last for about 12 hours. The reacted suspension was dialyzed against DI water to eliminate the unreacted excess GA molecules. Then, to the dialyzed suspension was added 5 mL HEPES buffer, and then it was divided by half, to the first part, 20 mg transferrin was added for conjugation and 2 mg of FA for the second part. The reaction was allowed for about 12 hours. Next, 5 mg of glycine were added to the suspension of nanoparticles to block the remaining aldehyde groups on the surface of the nanoparticles. Finally, the suspensions were dialyzed, purified and then stored at 4 °C.[v]

In the third method, called S3, NHS-PEG-NHS was used for conjugation of BT2-SNPs. 14.5 mg (MW: 3,000) was added to 2 mL of the suspension of BT2-SNPs (

M), and NaOH solution was added until the pH value of the solution was around 8. After 12 hours of stirring, the reaction solution was dialyzed against DI water for 24 h to remove the unreacted excess NHS-PEG-NHS molecules. Next, to BT2-SNPs-PEG suspension was added 1.33 mL HEPES buffer. 485 μL of GA was added, and the reaction lasted for about 12 hours. The reaction solution was then dialyzed against DI water to eliminate the unreacted excess GA molecules. 24 hours later 2.66 mL HEPES buffer was added to the dialyzed suspension and 4 mg Tf was added to 1 ml as-diluted suspension for

conjugation. Next, certain 6 mg were added to FSNPs-PEG-Tf to block the remaining aldehyde groups on the surface of nanoparticles. After purification, the suspension was stored at 4°C.[182] Figure A3.

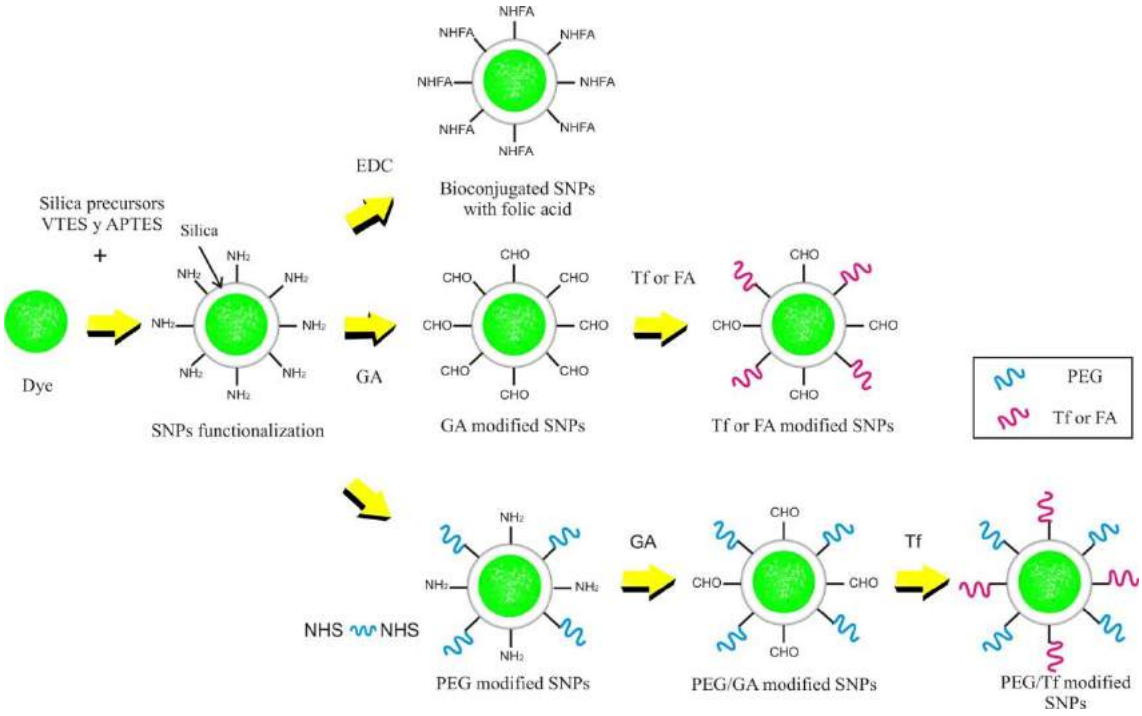

Fig. A3. Schematic illustration of three routes for the bioconjugation of FSNPs.

Appendix F. Agarose gel electrophoresis

The functionalization and bioconjugation was monitored by agarose gel electrophoresis which is a successful technique used to separate nanoparticles according to size and shape, also it is commonly used to separate biomolecules and to sort nanoparticles according to the exact number of attached polymer chains.[vi]

Agarose gels (0.35-0.5%) were prepared with and immersed in sodium bicarbonate solution and 1X TAE buffer (TRIS, Acetic acid, EDTA buffer). The gels are run in a horizontal electrophoresis system fabricated by the student Yenisey Ponce from the Group of Dr. Juan Luis Pichardo. The FSNPs-NH_2 and FSNPs functionalized using different conditions in the synthesis were set and agarose gel is run for 30 min at 90-150 V in 0.5X TAE buffer. Gel images were recorded with a digital camera and processed the images only with small

linear contrast adjustments in order to give a true representation of the visual gel appearance.

Appendix G. Cell cytotoxicity assay

Methylthiazolyldiphenyl-tetrazolium (MTT) assays were performed to assess the cytotoxicity of fluorescent samples into HeLa and A549 cells. These cells were seeded in 96-well plates and incubated at 37 ° C and 5% CO_2 for 24 h to allow adherence in the well. Then dilutions (in the range 1:1-1:32) of the aqueous suspensions of **M1(P1)**-NPs, **M1**(**P1**)-SNPs in DMEM medium were made and the cells were incubated 24 h to allow the suspensions of nanoparticles acting on all cells. After this, the medium was removed and replaced with fresh culture medium. Next, MTT (0.5mg/mL) in 1×PBS solution was added into each well. The MTT medium solution was carefully removed after 4 h of incubation and purple MTT-formazan crystals were formed. Finally, this precipitated was dissolved by adding isopropanol and the absorbance of MTT at 540 nm was measured by ELISA microplate reader (Labsystems Multiskan). The percentage of viability was obtained as follows: % Viability = OD treated cells × 100 / OD control cells.

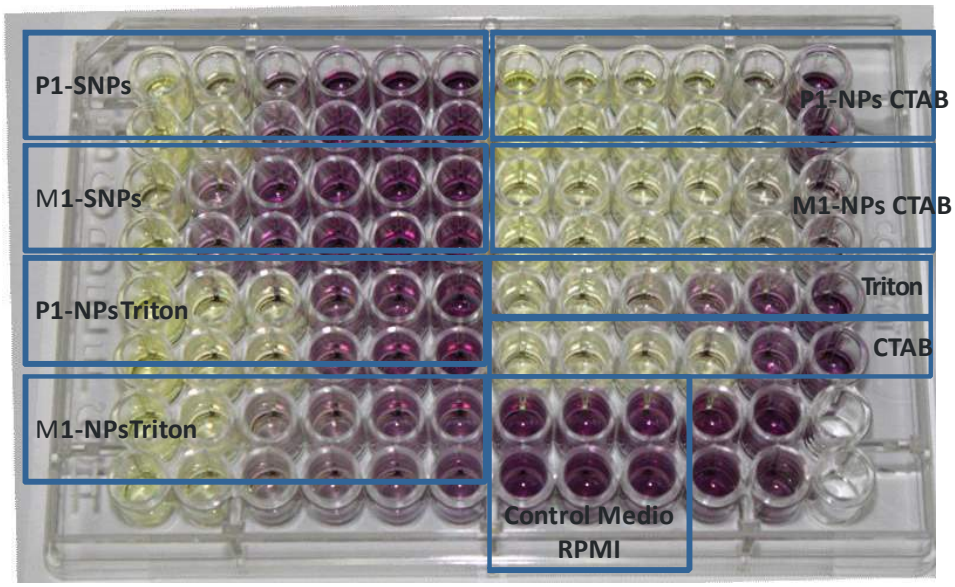

Fig. A4 Cell cytotoxicity assay. Cells were seeded in 96-well plates and exposed with an aqueous suspensions of **M1(P1)**-NPs, **M1**(**P1**)-SNPs. Purple color shows that there are live cells.

i. Jiménez C. C., Farfán N., Romero-Avila M., Rodríguez M., Aparicio-Ixta L., Ramos-Ortiz G., Maldonado J. L., Santillan R., Magaña-Vergara N. E., Ochoa M. E. *J. Organomet. Chem.*, 755, 33–40, (2014).

ii. Zhao Z., Chen B., Geng J., Chang Z., **Aparicio-Ixta L.**, Nie H., Goh C. C., Ng L. G., Qin A., Ramos-Ortiz G., Liu B., Zhong Tang B., *Part. Part. Syst. Charact.*, **31**(4), 481–491 (2014).

iii. Ramos-Ortíz G., Maldonado J.L., Hernández M.C.G., Zolotukhin M.G., Fomine S., Fröhlich N., Scherf U., Galbrecht F., Preis E., Salmon M., Cárdenas J., Chávez M.I., *Polymer* **51**(11), 2351–2359 (2010).

iv. Rodríguez-Romero J., Aparicio-Ixta L., Rodríguez M., Ramos-Ortíz G., Maldonado J. L., Jiménez-Sánchez A., Farfán N., Santillan R., *Dyes Pigm.*, **98**(1), 31–41 (2013).

v. Qian J., Li X., Wei M., Gao X., Xu Z., He S., *Opt. Express*, **16**(24), 19568–19578 (2008).

vi. M. Hanauer, S. Pierrat, I. Zins, A. Lotz, Carsten Sönnichsen, *Nano Lett.*, **7**(9), 2881–2885 (2007).